UNIVERSITY OF STRATHCLYDE

DOCTORAL THESIS

Creation of an All-Optical Bose-Einstein Condensate

Author:
Andrés ULIBARRENA

First supervisor:
Prof. Stefan KUHR
Second supervisor:
Dr. Elmar HALLER

A thesis submitted in fulfillment of the requirements for the degree of Doctor of Philosophy

in the

Experimental Quantum Optics and Photonics group

July 3, 2020

Declaration of Authorship

I, Andrés ULIBARRENA, declare that this thesis titled, Creation of an All-Optical Bose-Einstein Condensateand the work presented in it are my own. I confirm that:
Signed:

_____

Date:

_____

"It happened sometimes in the practice of physics that the student, having wrestled for hours with a recalcitrant equation, would suddenly find a way to wreak some drastic simplification upon it. Of a sudden, two terms, which he had copied out time and again, and which had become as familiar to him as his own signature, would, through some insight, or the providence of some new scrap of information, turn out to be equal to each other, and vanish from the equation altogether, leaving a wholly new mathematical sentence to be pondered. The student's first reaction was exhiliration: pride at his own cleverness, mingled with a sense that at last he was getting somewhere. But soon sobriety took over, as he pondered the remade equation and became aware that he was really just starting on a new problem."

Neal Stephenson, Baroque Cycle vol. 3, The System of the World

UNIVERSITY OF STRATHCLYDE

Abstract

Physics
Experimental Quantum Optics and Photonics group

Doctor of Philosophy

Creation of an All-Optical Bose-Einstein Condensate

by Andrés ULIBARRENA

This thesis reports on the experimental setup of the initial stages of the two-species, ^{87}Rb and ^{85}Rb, bosonic quantum gas microscope. In particular on the initial cooling and trapping of ^{87}Rb atoms, with the creation of a large all-optically cooled Bose-Einstein condensate as a proof of the temperatures and densities achieved. In most cold atoms experiments, the Bose-Einstein condensate is achieved by evaporating the atoms in a magnetic trap. Due to the swallowness of magnetic traps, the evaporation sequence takes longer than in all-optical traps. One of the reasons for using all-optical traps is to have a high repetition rate.

After a historical introduction to the topics of atomic physics, ultracold atoms in optical lattices and quantum simulation, we provide a basic summary on atomic physics and laser cooling. It is followed by a description of the experimental setup. The following chapters detail the cooling and trapping process, culminating in the creation of an all-optical Bose-Einstein condensate. The final chapter offers an overview on the future stages of the two-species bosonic quantum gas microscope.

In this thesis we detail our cooling techniques, such as grey molasses and the evaporative cooling process. We achieve temperatures as low as 4 µK in clouds of 3×10^9 atoms after grey molasses and a BEC of 1.8×10^6 atoms with a total sequence time under 5 s. There is still room for improvement in our BEC creation process and we are confident that higher numbers can be achieved.

Acknowledgements

If back in 2015 when I was finishing my degree someone had told me that in 2020 I would have finished a PhD in quantum simulation and that I would have helped build a quantum gas microscope I would have not beieve it, and then I would have asked what exactly are quantum gas microscopes and quantum simulators. Thankfully, now I know what a quantum simulator and a what a quantum gas microscope are, and a plethora of other interesting concepts.

None of this would have been possible without the continued help, support, patience and trust of my thesis supervisor, Prof. Stefan Kuhr. Even back then, when I did not have the knowledge and my previous experimental experience was a wee project on the field of interferometry, Stefan believed in me and offered me the chance to work in not one but two great experiments. I cannot thank Stefan enough for this opportunity, everything that he taught me and all the help that he provided on these more than four years.

Before I go into more details of the aforementioned experiments and the people that helped me there, I need to mention Dr. Elmar Haller, my second supervisor. When I had problems with an arcane piece of software that needed mending, when I had to prepare for a viva, when I had silly (sometimes not so silly) questions, Elmar was there to help me. Thank you very much for your help, and for dealing with my frequent questions. In the future I hope to be able to answer yours!

The first laboratory I worked in was the fermionic quantum gas microscope, affectionately known as the "potassium lab". My knowledge of atomic physics and quantum optics was nonexistent. Thankfully Dr. Bruno Peaudecerf and Dr. Manuel Andia, the two post docs in charge of the lab, taught me too many things to list here. I only directly worked with them during my first year, but they remained a constant source of advice and friendship over the remainder of their stay at Glasgow. Even though we only coexisted there for a brief time, Dylan Cotta also helped me getting the hang of the lab and other experimental stuff such as soldering and gluing optical elements. I can say that thanks to that I make less of a mess now.

In January 2017, Stefan offered me to start working in a new lab. We were going to build a new quantum gas microscope from scratch. It took me exactly one second to say yes and to ask when could we start working on that. At the beginning it was just the two of us but in April Hector Abel, a summer student, joined us for three months and helped set up some of the equipment. In June Ilian Despard joined us and everything went much more smoothly. Having a second PhD student was not only very fun but also we were able to specialise (and thanks to that I am "the laser guy" nowadays even in my new experiment). And also, thanks to Ilian we went on many adventures with our friends playing DnD, even one memorable Saturday night when we were playing, discovered that the pressure in the lab was spiking and we went there to fix the problems. Here's to many more adventures!

In January 2018, Harikesh Ranganath joined our lab as a "summer student". Even though summer was far away, his warmth and humor were a much welcome addition at the lab. Sadly, he joined the "potassium lab" for the PhD. But that did not hinder him on joining me for bouldering, RPGs, watching movies or whatever we had decided to do. Thank you!

Later that year, Dr. Arthur La Rooij joined us as a post doc in the bosonic quantum gas microscope. As Bruno and Manuel were leaving soon, he too got snatched by the potassium. Nonetheless, he had always time to help me with my questions and problems. Thank you very much Arthur! And from November to May 2019, Maximilian Ammenwerth, a master student, joined us. His dedication, knowledge and enthusiasm were those of a PhD student and I cannot thank him enough for helping me in those hard times when we were always so close of achieving a BEC. Visit us soon, Maximilian!

As soon as Maximilian left, Clemens Ulm, Paul Schroff and Charalampos Nikolatos joined the team as summer students. It was very fun to have you and you helped us bring a lot of projects to fruition. Thanks!

In July of that year, Dr. Andrea Di Carli became our postdoc. Andrea and I used to go have lunch together, exploring the many restaurants of the centre of Glasgow and, before we knew it many others joined us in that great custom. Here's to the many, many lunches that we enjoyed Andrea, and to the many more that we will enjoy!

I would also like to mention other people that helped me along the PhD, such as my office mates Craig Colquhoun and Matthew Johnson. We have had plenty of fun discussing life in general and nerd things in particular! Dr. Paul Griffin and Dr. Jonathan Pritchard were also a huge help on my PhD and always glad to assist even when they were buried under their duties and tasks. Last but not least, I want to thank my friend and flatmate Adrián Costa, whom I snared into a PhD at Strathclyde. Thank you very much for joining me in Scotland and for all the fun times we've had in the flat and outside of it!

I am sure that I am leaving behind a lot of people that, without their help this PhD would not be possible, such as my viva examinors Prof. Gian-Luca Oppo and Dr. Donatella Cassetari. Without their help, this thesis would be far worse. Also, both my supervisors and my team members input and corrections were instrumental to this thesis and I cannot stress enough that fact. Lastly, I would like to thank the Experimental Quantum Optics Group at Strathclyde University and my friends and family at Spain and Galicia.

I acknowledge funding of my PhD stipend though the ERC project "FERMILATT", the Strathclyde SCDT "Quantum Optics and Quantum Technologies" and the Faculty of Science at the University of Strathclyde.

Contents

Dedicado a mis padres, por su continuo apoyo y amor incondicionales.

Chapter 1

Introduction

1.1 A brief history of atomic physics

The atomic theory of matter theorises that matter is comprised by infinitely small, unbreakable[1], building blocks which, in turn are surrounded by a void. The first atomic theory was proposed by members of the Ionian philosophy school in the 5th century BCE. These philophers were Democritus, Leucippus and Epicurus (5th and 4th centuries) [1]. Not only they were some of the first philosophers that moved away from mythological thoughts, they also proposed the first theory that resembled modern atomic theory. They arrived to their definition of atoms by arguing that there had to be a limit when subdividing matter, a final, indivisible fragment. Democritus argued that different atoms had different geometrical shapes and that they interacted as time passed.

As Aristotle and Plato, the most important philosophers of medieval Western culture, rejected the idea of a *mechanical cosmos*, work on atomism was discontinued in the West until the Renaissance. Independent development of atomic theories was continued in the Islamic, Hindu and Buddhist cultures up to the late middle ages, but as the basic concepts did not differ from the ones postulated by the Ionian school, we will not describe them further.

In the 16th century CE, atomic theory gained momentum again by the works of Henry Percy, Francis Bacon, Galileo Galilei and René Descartes, among others [1]. Even though he barely improved on the previously established atomist theories, Henry Percy, the 9th Earl of Northumberland (1564-1632), helped revive the concept of atom. Later, he influenced one of the most prominent philosphers of England at the time, Francis Bacon, towards atomism. The first one to begin to reject the Aristotelian corpus and to move on to a new model was Galileo Galilei (1564-1642), in his work "Discourse on floating bodies"[2]. He partially rejected some of Aristotle's theory, e.g. matter is comprised of corpuscles in motion, but never fully commited to a completely new model that explained some of the flaws of Aristotelian physics.

[1] *Atomon* means unbreakable in Greek.

René Descartes (1596-1650) postulated that matter is comprised of vortices that continously interact with each other and abhorred the notion of a void. He also moved farther away from classical atomism with his theory on the duality of mind and matter.

Europe during the second half of the 17th century and the first quater of the 18th, the Baroque, was a melting pot of scientific activity. Based on the works of Galileo, Descartes, Huygens and others, a plethora of new theories in different fields were developed in a very short time. Sir Isaac Netwon (1642-1726) and Gottfried Wilhem von Leibniz (1646-1716) developed calculus independently. Robert Hooke (1635-1703) studied phenomena and fields as varied as forces, architecture, horology and, in the case of microscopy, was the first one to employ it as a scientific tool. Robert Boyle (1627-1691) worked closely with Sir Isaac Newton in the latter's alchemical works, and is considered the first chemist. Boyle accepted the idea of a mechanical universe from Descartes and combined it with the concept of the atom, thus laying the foundation for modern atomic theory. It is also worth mentioning here Leibniz's theories on monads. He postulated that monads were the fundamental unit of the cosmos and all matter was comprised by them. Leibniz also attributed certain properties to the monads, such as being able to "feel" and interact with each other constantly in complex ways. Leibniz's monads are not so dissimilar on a very fundamental level to modern atoms in quantum theory.

In the early 19th century, John Dalton aggregated the numerous data collected by contemprary scientists to postulate the same elements appeared in many different substances [3]. Each element was composed of a unique kind of atom and so the conglomerates that these atoms create give rise to the different molecules and materials. It was considered the first modern atomic theory and others followed in Dalton's steps. In 1897, J.J. Thompson proposed that atoms were composed of negatively charged electrons and a positively charged uniform sea-like substance and that the electrons were like plums in a pudding [4], hence the name of this model, the "plum pudding model". Ernest Rutherford refuted Thompson's model in 1909. According to the data his colleagues Hans Geiger and Ernest Madsen gathered in their experiment, atoms are comprised of negatively charged electrons orbiting around positively charged nuclei [5], the "planetary model". There were several problems with this model, such as why do not the atoms collapse as the negatively charged electrons are attracted by the positively charged nucleus. A quantised description of the atom was needed to solve those problems. The quantum revolution began in the early 20th century when Max Planck published his seminal paper on black body radiation [6]. In 1923 Niels Bohr proposed a model of the atom where the energy and orbital momentum were quantised and thus the electron orbited around a positively charged nucleus at fixed distances, depending on its energy. The Bohr atomic model is the first truly quantum one and as quantum mechanics was better understood, the

models became ever so refined. Erwin Schrödinger elaborated on Louis de Broglie's hypothesis on the particle-wave duality of matter and went on to work on how to describe the dynamics of an electron in an atom as a wave. His efforts resulted in the famous Schrödinger equation. In its time dependent form it takes the form of:

$$i\hbar\frac{\partial}{\partial t}\Psi(\vec{r},t) = \hat{H}\Psi(\vec{r},t), \tag{1.1}$$

where i is the imaginary unit, $\hbar$ is the reduced Planck constant, Ψ is the electron wavefunction, t is time and $\hat{H}$ is the Hamiltonian. Schrödinger's equation describes systems on a more fundamental level than Newton's laws. It can describe simple models, like the electron on a hydrogen atom and complex models, e.g. ensembles of atoms in periodic potentials. By choosing the proper Hamiltonian of the system and solving Schrödinger's equation, the system is perfectly defined and it is possible to extract all the required information.

Phenomena like high-temperature superconductivity, could be fully described by the Schrödinger equation with the right Hamiltonian, as previously stated. The only downside is that solving the Schrödinger equation in complex systems with current technology ranges from the computationally expensive to impossible in a timescale shorter than an age of the universe. But, there are tools that we can use to simulate the results of solving the Schrödinger equation in complex situations. These tools are the quantum simulators, a subset of quantum computers. Quantum simulators can be built employing a plethora of media, e.g. ultracold neutral atoms in optical lattices, arrays of trapped ions, arrays of cavities, nuclear spins, superconducting qubits, and quantum dots among others. For the remainder of this thesis we will focus on quantum simulation employing neutral atoms in optical lattices. As we will see in the next sections, ultracold atoms, in particular Bose-Einstein condensates, offer unprecedented capabilities as quantum simulators. In our experiment we employ bosonic ^{87}Rb. In future stages of the experiment we will also use ^{85}Rb.

1.2 Ultracold atoms and Bose-Einstein condensation as tools to probe new phenomena

When ensembles of atoms trapped in a potential reach low enough temperatures and high spatial densities, the atoms undergo a transition to a new quantum phase, called Bose-Einstein condensate. In a bosonic system, it is possible for more than one boson to share wavefunction and quantum numbers with others. Once there is a high enough number of indistinguishable bosons in the same space, the bosons condense and form a Bose-Einstein condensate with a single waveform. The wide range of phenomena that we can explore using Bose-Einstein condensates (BECs) constitute its main advantage as a medium for ultracold atoms in optical lattices for

quantum simulation, but ultracold alkali atoms are used in a plethora of experiments such as atomic clocks or interferometry.

There could be no BEC of ^{87}Rb without the technology and the knowledge needed to cool down the atoms to sub-μK temperatures. It took almost 20 years since Theodor W. Hänsch and Arthur L. Schawlow [7] theorised about a novel technique to cool down atoms using radiation pressure in 1975. It was then experimentally achieved by David J. Wineland's group in 1978 with ions [8]. In 1985, the group of Stephen Chu cooled atoms below the Doppler limit [9] employing the optical molasses technique. Later on, in 1989, Jean Dalibard, Claude Cohen-Tannoudji and Alain Aspect created a model that explained why sub-Doppler temperatures can be achieved by molasses cooling [10, 11]. They named their effect Sysiphus cooling after the Greek myth where a man is condemned to roll a rock on the slope of a mountain, only to begin anew the next day. It is also known as polarisation gradient cooling, because the atoms are cooled as they traverse the polarisation potential hills and valleys. Recently, molasses cooling was further improved by creating a coherent two-photon transition scheme with the addition of a phase-coherent repumping beam. By doing so, molasses cooling becomes a two photon cooling scheme. It brings the atoms to a velocity dependent dark state, where they remain cold as they cannot be heated by other photons. As the atoms are neither totally in a dark state nor in a bright state, this technique is known as grey molasses cooling [12, 13].

By adding a magnetic gradient to the optical molasses, in 1987 the team of Stephen Chu were able to not only cool down to less than a mK but also trap 10^7 atoms in a scheme known as magneto optical trapping [14]. In 1986 Stephen Chu and Arthur Ashkin developed a neutral atom trapping technique using the dipole force in a tighly focused laser beam. They named it optical dipole trapping [15]. In 1988, Daniel Kleppner developed a cooling technique known as evaporative cooling for hydrogen atoms in which decreasing the depth of the trap nonadiabatically forces the hotter atoms to exchange heat with the colder ones and escape the trap [16]. This technique was later exploited by Eric Cornell, Carl Wieman and Wolfgang Ketterle in 1995 as they first achieved the creation of a Bose-Einstein condensate [17, 18].

Bose-Einstein condensates in optical lattices are the ideal systems to probe bosonic models that describe bosons in a periodic potential, such as the Bose-Hubbard model (Equation 1.2). The Bose-Einstein condensate is prepared in the optical lattice. Optical lattices in one dimension consist of the standing wave-like interference pattern created by counterpropagating beams. By adding pairs of counterpropagating beams on the axes perpendicular to the initial one the lattice can be extended to three dimensions. Once the bosons condense in a Bose-Einstein condensate, we can observe phenomena such as the superfluid to bosonic Mott insulator transition just by varying the ratio between the tunneling rate and the interaction energy between the bosons [19]. That is achieved by increasing or decreasing the intensity of the laser beams that conform the optical lattice.

Another example would be the transition between a two-dimensional system

and an array of one-dimensional systems. By varying the intensity of one of the the three pairs of beams that create the three-dimensional optical lattice, we create a series of 1D systems, where tunneling is possible in one dimension but not in the others. In this fashion we can split a single two dimensional BEC into an array of one-dimensional BECs. We can also probe spin propagation dynamics by addressing a single atom in a particular lattice site [20].

1.3 Quantum simulation and quantum gas microscopes

Quantum gas microscopes offers a novel way to study single atoms in optical lattices. The realisation of quantum gas microscopes has been possible thanks to the marriage between optical microscopes, whose great magnification allows the study of microscopic objects; and quantum simulators, systems where a quantum Hamiltonian can be prepared in order to simulate its behaviour. Due to the computational cost of simulating quantum mechanics, quantum simulators are the preferred tool in order to simulate complex quantum systems. We will now embark on journey through the histories of microscopy and quantum simulation.

It is in the 17th century when microscopes were first developed. They consist of a system of lenses designed to create an image of the object several times larger than its original size, thus greatly magnifying objects so small that would be otherwise impossible to resolve. Microscope technology improved in the following centuries and, in the 20th century, microscopes were not only tools to observe matter but also able to alter it, e.g. atomic force microscopes enable us to observe and rearrange individual atoms [21].

Even though Robert Hooke did not develop the microscope himself, that was the work of Hans and Zacharias Janssen, a father and son pair of Dutch speclemakers, he was the first to use it in scientific investigations. In Hooke's work "Micrographia" [22] he detailed several animals and physical phenomena. He made several diagrams of tiny animals, such as fleas, and also discovered that the sparks generated after the clash of two metals are actually bubbles of molten metal that cool down as they radiate heat. Another of his observations is the fact that organic tissue is comprised of microscopic reticules, which were later known as cells. Microscopy continued to improve, making it possible to observe systems of increasingly reduced size.

As quantum theory was better understood, Richard Feynman realised that the best tool to simulate quantum mechanical systems were computers that operated with a quantum mechanical ruleset, known as quantum computers. A subset of quantum computers designed to simulate a system are known as quantum simulators. In 2009, several groups developed quantum simulators based on the concept of ultracold atoms in optical lattices imaged by a large aperture microscope [23, 24].

In 1982, Feynman published "Simulating physics with computers". In this paper, he analises several kinds of possible simulations and simulators. He arrives at the conclusion that the best tool to simulate quantum systems, are computers that behave quantum mechanically. His famous quote "I therefore believe that it's true that with a suitable class of quantum machines, you could imitate any quantum system, including the physical world" (sic.) opens the way for quantum systems designed to simulate other quantum systems, i.e. quantum simulators.

The main obstacle of simulating quantum systems in classical computers is the exponential increase of the size of the Hilbert space with the system size, and a full simulation of a quantum system will use up more memory and computational tail than is accessible with the current classical technology.

Quantum gas microscopes are a particular type of quantum simulators, which, in turn are a subset of universal quantum computers. Specifically, a quantum gas microscope is a kind of quantum simulator that employs ultracold atoms in optical lattices and images them with a microscope objective with enough optical resolution to resolve single atoms. By controlling the intensity of the beams of the optical lattice we can fully tune the ratio between the tunneling rates and the interaction strength of the atoms, thus being able to supress tunneling between lattice sites completely. By using spatial light modulators [25, 20, 26] it is possible to address single sites with a high degree of precision, enabling us to study phenomena such as thermalisation and many body localization [27] or quantum walks [28].

Ultracold atoms at sub μK temperatures are the ideal system to simulate models like the Bose (or Fermi)-Hubbard model. The Bose-Hubbard model describes the interactions between the bosons on a periodic potential and their tunneling rates. The Hamiltonian that describes the Bose-Hubbard model is:

$$H = -t \sum_{\langle i,j \rangle} \hat{b}_i^\dagger \hat{b}_j + \frac{U}{2} \sum_i \hat{n}_i(\hat{n}_i - 1) - \mu \sum_i \hat{n}_i, \tag{1.2}$$

where t is the tunneling rate, $\langle i, j \rangle$ denotes neighbouring sites i and j, $\hat{b}_i^\dagger$ and $\hat{b}_i$ are bosonic creation and annihilation operators ($\hat{n}_i = \hat{b}_i^\dagger \hat{b}_i$), U is the on-site interaction potential and μ is the chemical potential. Since the first observation in Immanuel Bloch's group of a quantum phase transition from superfluid to Mott insulator in 2002 [19], many experimental groups have used the Bose-Hubbard model to explore phenomena such as the observation of the Higgs amplitude mode [29, 30, 31, 32], frustrated systems [33, 34] or spin transport phenomena [35, 36, 20]. For the reasons above, ultracold atoms in optical lattices and, in particular, quantum gas microscopes, are extremely versatile tools to understand the behaviour of the Bose-Hubbard model. The first attemp to image single atoms in an optical lattice was pioneered with bosons by the groups of Markus Greiner [23, 37] and Immanuel Bloch and Stefan Kuhr [24] and shortly after other groups built fermionic [38, 39, 40, 41, 42] quantum gas microscopes. Upon completion, our experiment will be a two-species bosonic quantum gas microscope, employing both ^{87}Rb and ^{85}Rb (Chapter 6).

1.4 Thesis structure

The main goal of this thesis is to show the creation of an all-optical Bose-Einstein condensate with our experimental apparatus. We begin the thesis with a historical perspective on atomic physics, ultracold atoms, Bose-Einstein condensation, microscopy, quantum simulation and quantum gas microscopy (Chapter 1). Chapter 2 provides theoretical tools such as laser cooling and trapping required to understand the phenomena described in the remainder of the thesis. The experimental apparatus is described in Chapter 3. In Chapters 4 and 5 we detail the data acquisition process and the experimental sequence required to obtain our all-optical Bose-Einstein condensate. Chapter 6 offers some conclusions on the thesis and points towards the next stages of our experiment. Appendix A contains the trap frequencies measurements during the evaporation process employed for our Bose-Einstein condensate characterisation.

Chapter 2

Basics of atomic physics and laser cooling

In this chapter we will provide the physics background required for laser cooling and trapping of atoms and to achieve Bose-Einstein condensation. We will begin by providing a brief description of the level structure of ^{87}Rb (Section 2.1), followed by laser cooling and trapping (Section 2.2), and we will finish the chapter with a summary on Bose-Einstein condensation (Section 2.3). In Section 2.2 we will focus on molasses cooling on both red (Section 2.2.1) and grey (Section 2.2.2) molasses, discussing their basic principles. We will continue with a discusion on magneto optical traps (MOTs, Section 2.2.3) and dipole trapping (Section 2.2.4). To conclude the section on laser cooling, we will introduce evaporative cooling (Section 2.2.5). As our experiment uses ^{87}Rb atoms, we will discuss Bose-Einstein condensation on a dilute cloud of bosonic atoms (Section 2.3.1).

Most of the derivations and theory for this chapter are based on the following references: Christopher Foot's "Atomic Physics" [43] book, Daniel Steck's "Rb 87 D Line Data" [44], the "Optical dipole traps for neutral atoms" review paper by Rudolf Grimm, Matthias Weidemüller and Yurii Ovchinnikov [45] and "Bose-Einstein condensation in dilute gases" [46] by Christopher J. Pethick and Henrik Smith.

2.1 ^{87}Rb level structure

As an alkali-metal atom, rubidium has a single electron in the outermost shell, thus behaves like a heavy hydrogen atom to a first approximation. The single electron in the outermost shell ensures a simple model to study and makes it easy to laser cool it. In order to determine which cooling schemes can be used with ^{87}Rb and the frequencies required, we need to know its atomic level structure. We are going to focus on the D_2 line, the $5^2S_{1/2} \rightarrow 5^2P_{3/2}$ optical transition, as its frequency is within the range of diode lasers. The $5^2S_{1/2} \rightarrow 5^2P_{3/2}$ transition is part of a fine structure doublet, the other line being $5^2S_{1/2} \rightarrow 5^2P_{1/2}$, the D_1 line. The fine structure is caused by the total electronic angular momentum ($\vec{J}$, Equation 2.1), which results from the coupling between the orbital angular momentum ($\vec{L}$) and the electron spin

($\vec{S}$) :

$$\vec{J} = \vec{L} + \vec{S}. \tag{2.1}$$

The coupling of the total angular momentum ($\vec{J}$) with the nuclear spin ($\vec{I}$) gives rise to the total atomic angular momentum ($\vec{F}$, Equation 2.2) and the hyperfine structure.

$$\vec{F} = \vec{J} + \vec{I}. \tag{2.2}$$

The quantum numbers for the ground state, $5^2S_{1/2}$, are $S = 1/2$ and $L = 0$, so $J = 1/2$. Consequently, for the excited state, $5^2P_{3/2}$, $S = 1/2$ and $L = 1$, so for the D2 line $J = |L + S| = 3/2$. The nuclear spin is the same for both ground and excited state and equal to $I = 3/2$ so the total atomic spin are $F = 2$ and $F = 3$, for the ground and excited state respectively.

2.2 Laser cooling and trapping

In this section we will describe the different methods that we employ to cool and trap our atomic clouds. We will begin by describing molasses cooling (Section 2.2.1), polarisation gradient cooling and grey molasses (Section 2.2.2). We will continue by explaining how magneto-optical traps work (Section 2.2.3). The next subsections show the theory behind optical dipole traps (Section 2.2.4) and evaporative cooling (Section 2.2.5).

2.2.1 Molasses cooling

The basis of molasses cooling is velocity-selective photon absorption enhanced by the Doppler effect. Let us consider two counterpropagating laser beams of equal intensity and a cloud of moving two-level atoms with a transition frequency of ω_0 in their reference frame. Atoms moving with different velocities along the propagation direction of the beams will experience different detunings to the transition frequency ω_0 due to the Doppler effect. We maximise the absorption and reemission of photons propagating in the opposite direction to the atoms by red-detuning our cooling light between two transitions, e.g. between $F = 2 \rightarrow F' = 2$ and $F = 2 \rightarrow F' = 3$. In a general case, any atom absorbing a photon increases its momentum by the photon momentum, but by absorbing a photon moving with opposite momentum, the total momentum of the atom is reduced and the atom cools down. Faster atoms will absorb more photons and thus be slowed more. This technique can be generalised to three dimensions by adding counterpropagating beams on the cooling transition on the other two axes. The velocity dependent force that the atoms feel is of the form:

$$F_{\text{Mol}} = -\alpha v, \tag{2.3}$$

with α being the damping coefficient. The molasses force, F_{Mol}, being velocity dependent, is analogous to a viscous force. It is not dissimilar to the one observed in viscous liquids, like honey or treacle; hence the name "molasses cooling" [43].

When cooling two-level atoms by absorption and reemission of photons, like in optical molasses, there is an equilibrium point between the cooling by the absorption of photons propagating in the direction of the moving atoms and the heating caused by the reemission in random directions. The temperature at the equilibrium is defined as the Doppler temperature:

$$T_D = \frac{\hbar\Gamma}{2k_B} = 146\,\mu\text{K}, \tag{2.4}$$

where $\hbar$ is the reduced Plack constant, Γ the natural linewidth of the transition and k_B the Boltzmann constant. While this is the theoretical limit for ideal two level atoms, molasses cooling cools down the atoms to temperatures below the Doppler temperature. This is because there are no perfect two level atoms and interactions with other hyperfine states need to be considered. This phenomenon was explained in more detail by Claude Cohen-Tannoudji and Jean Dalibard in 1989 [10].

2.2.2 Polarisation gradient cooling and grey molasses

An atom moving along the direction of two counterpropagating beams with orthogonal linear polarisations will feel a change from a σ_+ (σ_-) to σ_- (σ_+) every time it travels a distance of $\lambda/4$, with λ being the wavelength of the beam. The standing-wave nature of the two counterpropagating beams results in a periodic repetition of maxima and minima in the potential landscape, caused by the interference between the two counterpropagating beams. An atom moving from a potential valley towards a peak, will transform its kinetic energy into potential energy. Once the atom has climbed the potential and the polarisation becomes the opposite, it is optically pumped to the valley of the potential and will have to climb the potential again, losing energy in the process. This phenomenon is known as polarisation gradient cooling or Sysiphus cooling.

In order to improve the bright, or red, molasses it is possible to cool the atoms by using blue detuned open transitions from $F \rightarrow F' = F$ or $F \rightarrow F' = F - 1$ (see Figure 2.1 for a detailed scheme on the different beams employed on our grey molasses scheme). These transitions pump the atoms to Zeeman dark states. In those states, the atoms are optically transparent to the light. As the atoms absorb much less extra photons, they do not get heated as much by absorption and reemision of photons. That, and the fact that the atoms transition from bright to dark states as they get cooled is why this technique is known as grey molasses [13].

The Zeeman dark states are linear superpositions of $|F; m_F\rangle$ states [12]. They depend on the local polarisation of the cooling light and, only the atoms that move slowly enough can adjust adiabatically their linear superpositions to the local laser field. The atoms in bright states cooled by a blue detuned transition are slowed more

than those cooled by a red detuned transition and so a blue detuning, of typically 5Γ, is preferred.

If we use a weaker coherent repumper beam in our grey molasses cooling scheme on the $F-1 \rightarrow F'$, the grey molasses cooling becomes a two-photon transition in a Λ-configuration. Scanning the two-photon transition frequency enhances the cooling, as seen in Figure 4.16. As the general population of the atomic cloud gets cooled, the atoms accumulate in this dark state. While in the dark state, they are optically transparent to the cooling and repumper beams and thus they do not get heated by absorption and reemision of photons [12].

2.2.3 Magneto-Optical traps

A magneto-optical trap (MOT) uses the velocity dependent damping force of optical molasses to cool the atoms, with the addition of a position-dependent elastic force which keeps the atoms confined due to a magnetic gradient [14]. In one dimension, cooling is achieved by having opposite circular polarizations for a counterpropagating pair of beams and a pair of magnetic coils generating a magnetic gradient. By repeating the optical beam pair configuration for the other two spatial axes, we can extend the system to three dimensions.

Due to the Doppler effect and the frequency detuning of the light, an atom moving along the positive (negative) direction of z will feel more strongly the σ^- (σ^+) light and will be closer to resonance. The scattering will be greater and the atom will be pushed back to the centre of the trap. The equation of the force produced by the MOT on the atoms can be written in 1D as [14, 43]:

$$F_{\mathrm{MOT}} = -\alpha v - \frac{\alpha\beta}{k} z, \tag{2.5}$$

where α is the damping coefficient of the optical molasses, β is the Zeeman shift coefficient, k is the wavenumber of the radiation and z is the position of the atoms along the axis of motion.

2.2.4 Dipole trapping

The beams used in our experiment have a Gaussian intensity distribution, and we will assume a Gaussian profile for every beam in the rest of the thesis, with:

$$I(r,z) = I_0 \left(\frac{w_0}{w(z)}\right)^2 e^{-2r^2/w(z)^2}, \tag{2.6}$$

where $I(r,z)$ is the intensity of a beam propagating along the z-axis, with radial distance r. I_0 is the intensity at the centre of the beam at, at a minimal waist w_0. The waist at a distance z along the axis from w_0 is $w(z) = w_0\sqrt{1+(z/z_0)}$.

The evolution of the beam waist from the point of minimum waist, or focus, is as follows. The waist will be minimal at the focus and will symmetrically diverge

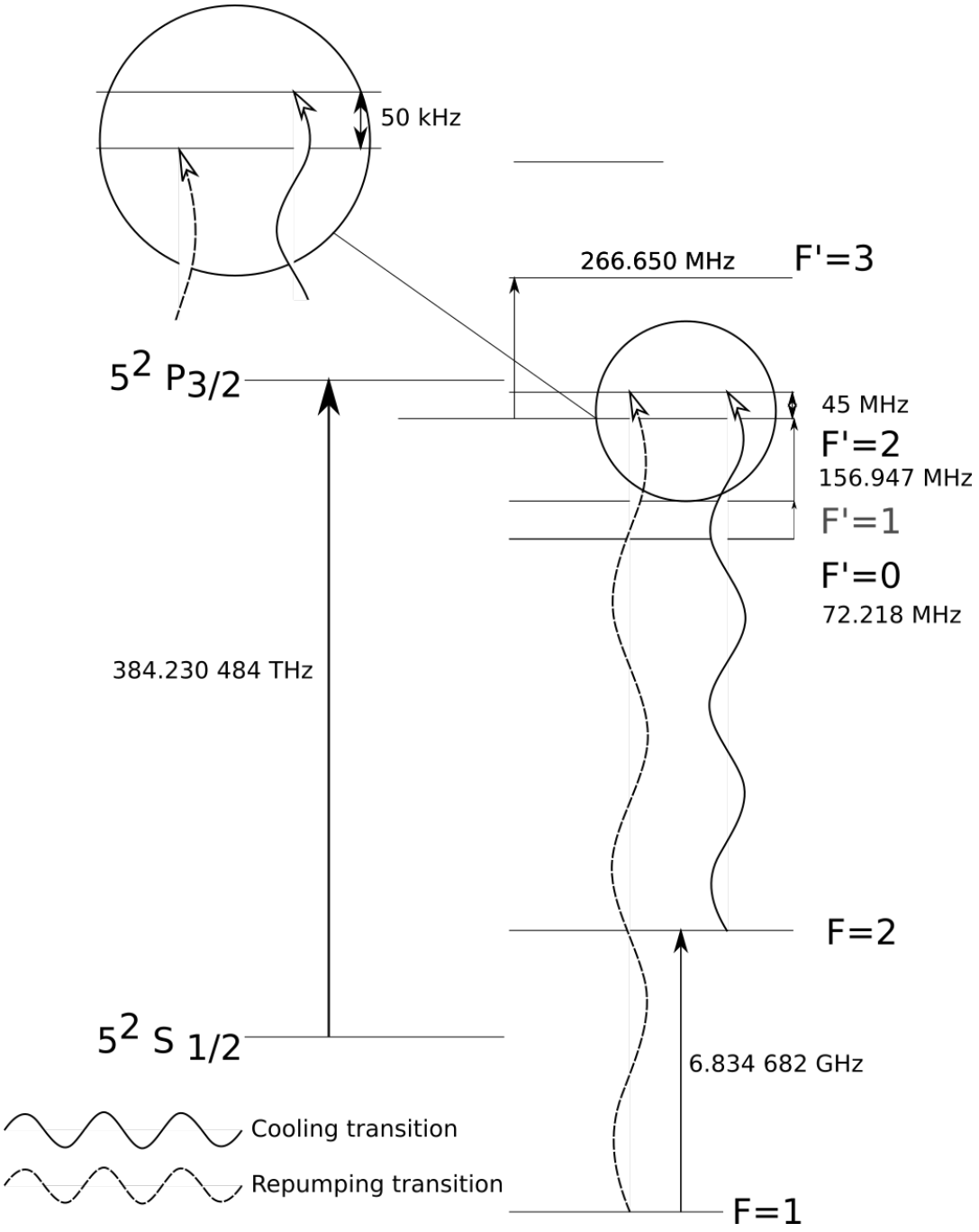

FIGURE 2.1: Scheme detailing the transitions used in our experiment for grey molasses cooling. In this diagram we see in red the repumping transition and in black the cooling transition. The detuning between the two is 50 kHz, as we can see in blue. By scanning the detuning between cooling and repumper beam, we can optimise our grey molasses cooling.

before and after it. The distance at which the waist w_0 increases to $\sqrt{2}w_0$ is defined as the Rayleigh length, z_0:

$$z_0 = \frac{\pi\, w_0^2}{\lambda}, \tag{2.7}$$

where λ is the wavelength of the beam. The inhomogeneity of the intensity and the

diverging waist create an intensity gradient along the radial and propagation axes. This gradient exerts a dipolar force on the atoms along the beam path and the radial direction. For detunings much larger than the natural linewidth of the transition, the force will give rise to a potential of the form [15]:

$$U_{\text{Dipole}} \approx \frac{\hbar\Gamma^2}{8\delta}\frac{I}{I_{\text{sat}}}, \tag{2.8}$$

where δ is the detuning from the transition, I is the intensity of the beam and I_{sat} is the saturation intensity. The potential changes its sign with δ, i.e. if δ is red detuned, the potential will be attractive and if it is blue detuned the potential will be repulsive. This potential will trap the atoms in the focus of the beam and it will offer stronger confinement in the radial direction, while weakly confining on the axial direction. In order to create a trap that offers good confinement in the three spatial axes we use a crossed optical dipole trap (CODT).

For very large ratios of detuning versus natural linewidth, the scattering rate becomes:

$$R_{\text{scattering}} \approx \frac{\Gamma^3}{8\delta^2}\frac{I}{I_{\text{sat}}}. \tag{2.9}$$

The scattering rate scales proportionally to $1/\delta^2$, while the trap depth scales proportionally to $1/|\delta|$. That is the reason why, when setting a dipole trap, a detuning on the order of hundreds of THz is preferred. In this way deeper traps with higher intensities can be created while avoiding heating of the atoms.

2.2.5 Evaporative cooling

In a first approximation, the atoms at the bottom of an optical dipole trap are confined in a harmonic potential. By lowering non-adiabatically the depth of the potential, the hotter atoms escape the trap while the colder atoms remain trapped [47]. If the trap depth is continuosly lowered, thus forcing the hotter atoms away, it is known as forced evaporative cooling.

To understand Bose-Einstein condensation, we need to know the phase-space density (PSD) of our atomic cloud in each of the evaporation stages. The PSD is defined as [46]:

$$PSD = \bar{n}\lambda_{\text{dB}}^3 = \bar{n}\left(\frac{2\pi\hbar^2}{mk_BT}\right)^{3/2}, \tag{2.10}$$

where $\bar{n}$ is the peak density, m is the mass of the individual bosons, λ_{dB} is the de Broglie wavelength, k_B is the Boltzmann constant and T is the temperature of the bosons. In a three-dimensional harmonic potential, $U(r)$, the potential is defined as $U(r) = m/2(\omega_x^2x^2 + \omega_y^2y^2 + \omega_z^2z^2)$. Here, ω_i are the trap frequencies on the different axes.

As the potential is lowered, the trap volume increases and the trap frequencies decrease. By carefully tuning the evaporation process, we can achieve a higher

phase-space density (Equation 2.10) of the atomic cloud, even taking into account the loss of atoms due to the evaporation.

The trap frequencies for a dipole trap in the radial directions, i.e. those perpendicular to the propagation of the beam, and in the axial direction of the propagation of the beam, are different from each other and have the following forms [48]:

$$\omega_{\text{axial}} = \sqrt{\frac{4U_{\text{Dipole}}}{m}}\frac{1}{z_0}, \tag{2.11}$$

for the frequency on the axial direction and

$$\omega_{\text{radial}} = \sqrt{\frac{4U_{\text{Dipole}}}{m}}\frac{\sqrt{2}}{w_0}, \tag{2.12}$$

for the frequency on the radial directions. In our case, $\omega_z = \omega_{\text{axial}}$ and $\omega_x = \omega_y = \omega_{\text{radial}}$.

The peak density is then [47]:

$$\bar{n} = N\bar{\omega}^3\left(\frac{m}{2\pi k_B T}\right)^{3/2}, \tag{2.13}$$

where $\bar{\omega}$ is the geometric mean of the trap frequencies, $\prod_{i=x,y,z}^{3}\sqrt[3]{\omega_i} = \bar{\omega}$. Taking into account the previous considerations, the equation for phase-space density in a harmonic potential becomes:

$$PSD = N\left(\frac{\hbar\bar{\omega}}{k_B T}\right)^3. \tag{2.14}$$

Other important parameters to understand our evaporation process are the collision rate and the evaporation efficiencies. The collision rate for elastic collisions, Γ_c is defined as [49]:

$$\Gamma_c = \bar{n}\sigma\bar{v}_{rel} \tag{2.15}$$

$\bar{n}$ is the peak density, σ is the collision cross section given by:

$$\sigma = \frac{8\pi a^2}{1 + k^2 a^2}, \tag{2.16}$$

$\bar{v_{rel}}$ is the average relative velocity of the atoms in the trap and a is the scattering length and k is the de Broglie wavevector, calculated by:

$$k = \sqrt{\frac{16 k_B T m}{\pi\hbar^2}}. \tag{2.17}$$

The evaporation efficiency, γ, is calculated as:

$$\gamma = \frac{\ln(\text{PSD}_f/\text{PSD}_i)}{\ln(\text{N}_i/\text{N}_f)}, \tag{2.18}$$

with PSD_f and PSD_i the final and initial phase-space densities and N_f and N_i the final and initial atom numbers. The evaporation efficiency represents the fractional improvement of phase space density per atom loss.

2.3 Bose-Einstein condensation

In 1924, Satyendra Bose published the paper "Plancks Gesetz und Lichtquantenhypothese" [50], where he proposed a novel derivation of Planck's Law. In the paper, he also described that the Maxwell-Boltzmann distribution is not valid for all the possible quantum particles. Einstein went on to postulate the existence of a kind of particles, later known as bosons, which would adhere to these new statistics [51, 52]. The distribution is called Bose-Einstein distribution due to their contribution in developing it.

In a thermal gas, its particles occupy a spectrum of energy levels and behave as individual particles. If the atoms are cold enough, they will occupy the lowest energy states. As opposed to bosons, fermions obey the Pauli exclusion principle and so two fermions cannot exist at the same point in phase-space sharing all quantum numbers. Bosons do not have this restriction so, in principle, an infinite number of bosons can share the same space with the same quantum numbers. In other words, if an ensemble of bosons is cooled to the lowest energy state, they will condense and behave as a macroscopic quantum phenomenon and all the condensed bosons will occupy the same space. More precisely, Bose-Einstein condensation happens when the number of bosons contained in a volume equal to the thermal de Broglie wavelength cubed (λ_{dB}) exceeds 2.612, which translates to the atoms being colder than the critical temperature (Equation 2.19) and thus achieving condensation.

Another quantity which charactherises the BEC phase transition is the critical temperature, T_c [53], defined as:

$$T_c = 0.94 \frac{\bar{\omega}}{K_B} N^{1/3}. \tag{2.19}$$

Below the critical temperature, the atoms begin to condense and in the $T = 0$ limit the full cloud is a BEC.

2.3.1 Bose-Einstein condensation on a dilute cloud of atoms

Bose-Einstein condensation has been achieved with some kinds of bosons, like liquid ^4He [54]. For the scope of this thesis, we will focus exclusively on creating a Bose-Einstein condensate from a cloud of cold atoms, in particular ^{87}Rb. Historically, the earliest [17] and most common way of achieving Bose-Einstein condensation with rubidium atoms is to first cool the atoms and then to increase the PSD by evaporating the atoms in a magnetic trap. We cannot employ magnetic traps for two reasons, the first being that in future stages of the experiment we will add ^{85}Rb as a second

species and we will use the high current coils to control the interactions with Feshbach resonances. The second reason is caused by the low trap frequency of magnetic traps, as evaporation is faster in optical dipole traps. Therefore, we will achieve Bose-Einstein condensation by purely optical means.

For that purpose we will use dipole traps for evaporating the atoms, rather than magnetic ones. This creates several challenges over magentic traps, such as the density reduction of the gas when decreasing the trap depth for optical dipole traps. To mantain a high PSD we need to carefully choose our beam waists so that we have a compromise between high trapping frequencies with fast evaporative cooling, and the trap volume for a large atom number.

2.3.2 Gross-Pitaevskii equation

The best way of describing the ground state of a system comprised of an ensemble of identical bosons is by using the Gross-Pitaevskii equation:

$$\mu\psi = \left(-\frac{\hbar^2}{2m}\nabla^2 + V_{\text{ext}}(\vec{r}) + g \mid \psi \mid^2 \right) \psi, \tag{2.20}$$

where ψ is the atomic wavefunction normalised to one, m is the mass of the individual particles, $V_{\text{ext}}(\vec{r})$ is the external potential, g is the coupling constant with $g = (4\pi\hbar^2 Na/m)$, a is the scattering length and μ is the chemical potential.

A BEC confined in a harmonic trapping potential at temperatures sufficiently close to $T = 0\,\text{K}$ and with an atom number large enough can be described under the Thomas-Fermi approximation of the Gross-Pitaevskii equation (Equation 2.20) when the kinetic energy is low enough compared to the interaction energy, $Na/a_{ho} \gg 1$ where a_{ho} is the harmonic oscillator charactheristic length. The expression of the Thomas-Fermi approximation of the GPE is:

$$\psi(r) = \begin{cases} \sqrt{\frac{\mu - V_{\text{ext}}(\vec{r})}{g}}, & \text{if } \mu > V_{\text{ext}}(\vec{r}) \\ 0 & \text{otherwise} \end{cases} \tag{2.21}$$

Using this solution, we can obtain the particle density of a BEC ($n = N|\psi(\vec{r})|^2$, where N is the atom number) confined to the bottom of a harmonic potential as an inverted parabola:

$$n = N\frac{\mu - V_{ext}(\vec{r})}{g} \tag{2.22}$$

The peak of the particle density is:

$$n_{\text{peak}} = N\frac{\mu}{g} \tag{2.23}$$

It is possible to obtain the temperature of the condensate cloud by knowing the condensate fraction, N_0/N, where N_0 is the atom number of the condensate fraction

and the critical temperature, T_c, (Equation 2.19) [46]:

$$T = (1 - \frac{N_0}{N})^{1/3} T_c. \tag{2.24}$$

Chapter 3

Experimental Setup

In this chapter we will describe the main components of our experiment and then we will characterise the principal laser systems. We will explain the purpose and description of the vacuum chamber (Section 3.1), then the microwave (MW) setup (Section 3.2), followed by the magnetic coils (Section 3.3) and continue with the laser system (Section 3.4). We will proceed with a description of the locking system of the cooling lasers (Section 3.5), the characterisation of the aforementioned locking systems (Section 3.6) and the experiment control software (Section 3.7).

Two experimental tables comprise most of our hardware. The so-called Laser Table hosts the cooling setup, which consists of the master (Section 3.4.1), repumping (Section 3.4.2), 2D (Section 3.4.3) and 3D (Section 3.4.4) cooling lasers. On the Experiment Table we have the vacuum chamber (Section 3.1), the trapping lasers (Sections 3.4.5, 3.4.6), the optical lattice lasers, the microscope, the MW setup (Section 3.2) and the magnetic coils (Section 3.3). Besides that, we also have the 2D and 3D MOT (Section 4.3), the imaging (Section 4.2), optical pumping (Section 5.1.2) and molasses (Section 4.4) systems.

3.1 Vacuum Chamber

The cold atoms in our traps might collide with the background gas and exchange heat with it, expelling atoms from the cloud. We avoid this situation by having our atoms in a vacuum chamber at extremely low pressures. Our vacuum chamber is detailed in a diagram in Figure 3.1. It is divided in two sections, the high vacuum and the ultra-high vacuum, linked by a differential pumping tube.

3.1.1 High-vacuum section

The high-vacuum section is used to pre-cool and collect the atoms for an initial trapping in a two-dimensional magneto-optical trap (2D MOT). The high-vacuum section the atoms consists of a rubidium oven, a glass cell, an ion pump and a differential pumping tube that separates the high-vacuum section from the ultra-high vacuum section (Figure 3.2). For normal experiment operations, we keep a pressure of approximately 1×10^{-7}mbar in this section.

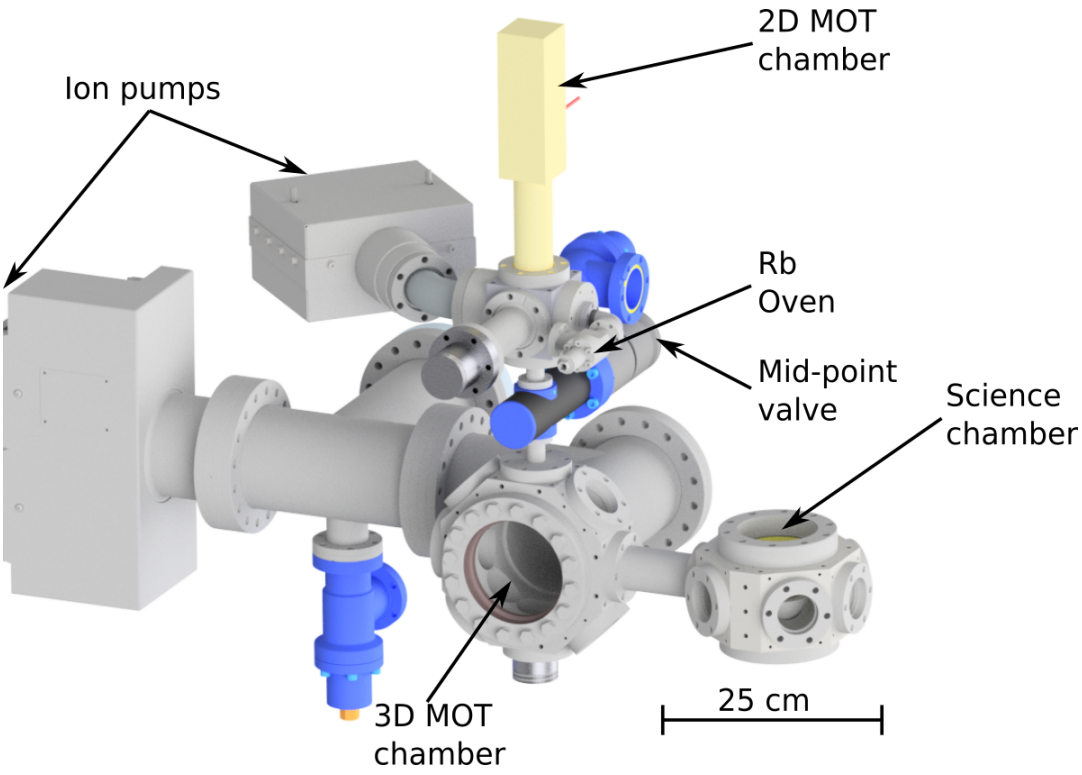

FIGURE 3.1: 3D rendering of the full vacuum chamber. The top section is the high vacuum section, while the bottom is the ultra-high vacuum section. Typically we keep pressures of 1×10^{-7} mbar and 1×10^{-11} mbar in the high and ultra-high vacuum chambers, respectively. The buttefly valve is not displayed in the figure.

The rubidium oven contains a glass ampoule filled with 1 g of rubidium isotopes in the natural proportions, i.e. 72% of ^{85}Rb and 27% of ^{87}Rb. When setting up the vacuum chamber, we broke the ampule and then the rubidium vapour diffused into the chamber. The oven has also a heating tape, which enables us to increase the temperature of the oven to increase its internal pressure and thus increase the flow of rubidium atoms into the high-vacuum section. The rubidium oven and the glass cell are connected by a valve, to regulate the flux of atoms towards the glass cell. One ion pump [1] is set between the glass cell and the differential pumping tube, to pump away the residual background gas from the outgassing of the vacuum components and to avoid saturating the glass cell with rubidium atoms and to minimise the collisions to the trap atoms from background gas. By controlling the opening of the oven valve and the butterfly valve situated before the pumps we can finely tune the amount of rubidium in the 2D MOT glass cell and thus the number of atoms that we load into the 2D MOT.

Our quartz glass cell[2] has dimensions of $50 \times 50 \times 150$ mm, glued with epoxy and with antireflection coating for near infrared light. It is where we initially capture the atoms from room temperature to a few millikelvin in our two-dimensional magneto optical trap (2D MOT, Section 4.3.1).

The differential pumping tube has 4 mm internal diameter and a length of 211.5 mm, and is capable of keeping more than three orders of magnitude of pressure difference between the glass cell of the high vacuum section and the ultra-high vacuum section.

3.1.2 Ultra-high vacuum section

As illustrated in Figure 3.3, the ultra-high vacuum section is divided into two different sections, the 3D MOT and Science chambers. The 3D MOT chamber is the section where the atoms are initially trapped and cooled (Sections 4.3, 4.2,5), before we transport them to the Science Chamber, which hosts the optical lattice system and the microscope (Chapter 6). The windows on the vacuum chamber are coated with antireflective coating for near infrared light and the interior of the bottom window of the Science Chamber is in addition coated to reflect the light from our vertical lattice, at a wavelength of 1064 nm. In normal operation, we keep pressures close to 1×10^{-11} mbar using an ion pump[3] and a titanium sublimation pump[4]. Our 2D MOT glass cell is arranged vertically. The main advantage is efficient use of the experiment table space. In most ultracold atoms experiments [55], the glass chamber of the 2D MOT section used to lay in the same plane as the 3D chamber. Having the 2D MOT section on top the ultra high vacuum chamber grants easy access to optics and enables further modifications and improvements that might be implemented in the future.

[1] 10 l/s VacIon pump.
[2] JPC-4-1717 manufactured by Japancell.
[3] Agilent VacIon 75
[4] Edwards, G360819

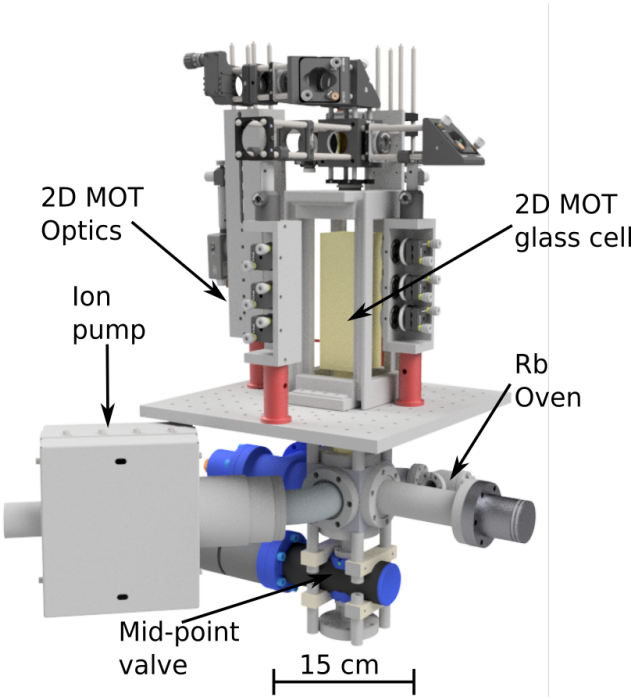

FIGURE 3.2: 3D render of the 2D MOT section of the high-vacuum section of the vacuum chamber and the 2D MOT optics and optomechanics. The buttefly valve is not displayed in the figure.

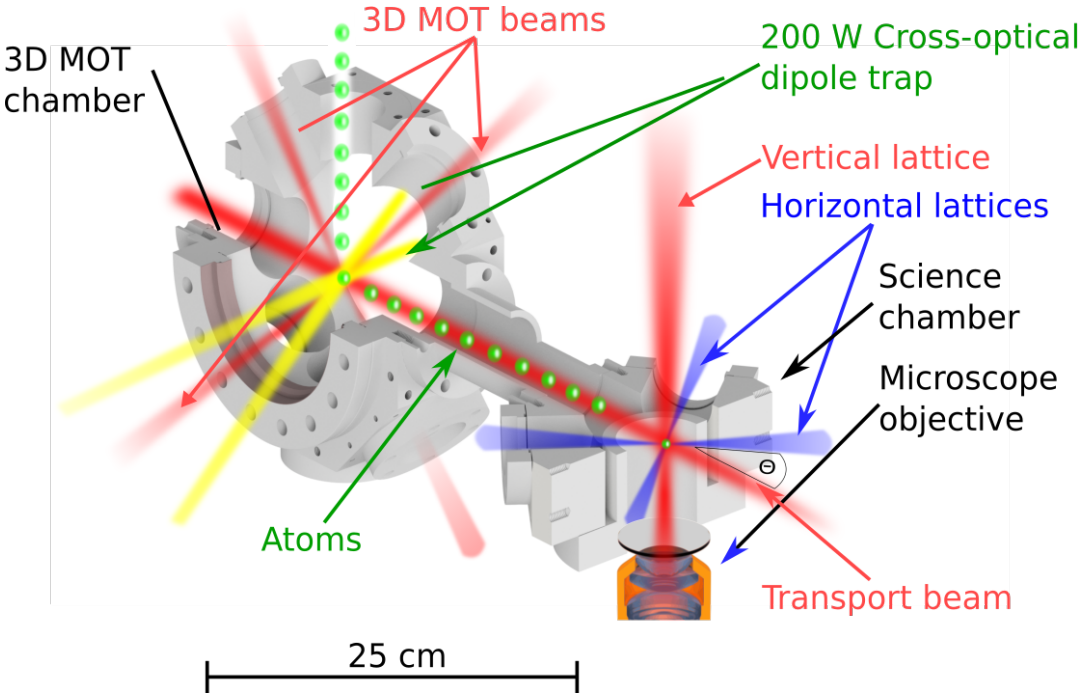

FIGURE 3.3: Cut-out render of the 3D MOT chamber (left) and the Science chamber (right).

3.2 Microwave setup

We use microwave radiation to transfer atoms between different hyperfine states, for example, rapid adiabatic transfer of atoms from $|F = 2; m_F = -2\rangle$ to $|F = 1; m_F = -1\rangle$. For ^{87}Rb the transition frequency is near $\nu_{\text{HFS}} = 6.834\,\text{GHz}$, within the range of operations of MW and radiofrequency devices. In our experiment, we use a combination of a MW antenna and a waveguide[5] to radiate with frequency ν_{HFS} on the atomic cloud.

Above 3 GHz the price of MW synthesizers escalates very steeply. We then generate our MW signal by using a phase-locked dielectric resonator (PLDRO) at 6.2 GHz. It receives a fixed clock signal from our signal generator at 10 MHz and multiplies it to a very precise 6.2 GHz signal. It provides a stable source at the desired frequency range, but we want to be able to fine tune it to at least single kHz precision. By mixing the signal from the PLDRO, acting as the Local Oscillator (LO), with another 500 MHz signal from our signal generator, acting as the Intermediate Frequency (IF), we obtain a Radio Frequency (RF) output signal close to 6.800 GHz.

That signal is filtered and amplified several times before relaying it to two 2-channel switches so we can divert the power either to one of our two MW antennas, one located in the "MOT chamber" and another in the "Science chamber", or to our electro-optical modulator (EOM, Section 3.4.4). See Figure 3.4 for a detailed diagram of the MW generation and amplification system.

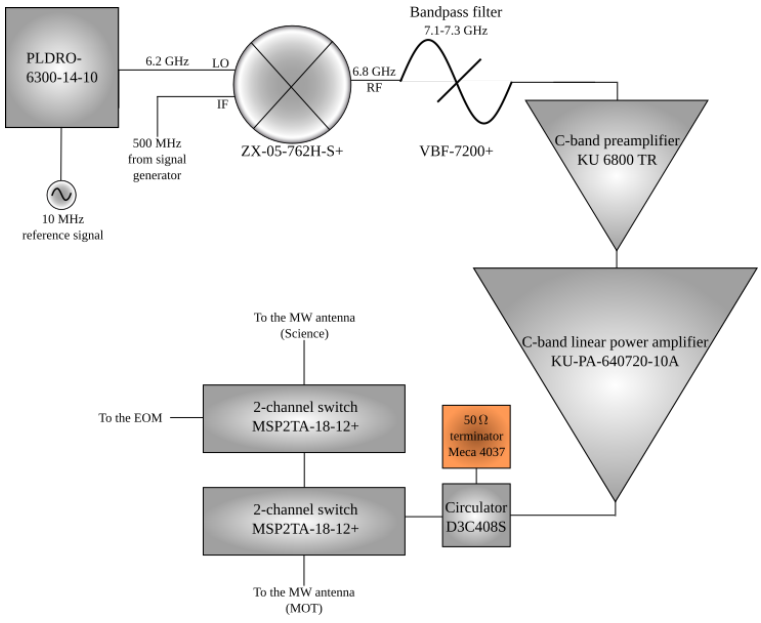

FIGURE 3.4: Diagram of the MW generation and amplification system.

[5] Flann, Model 15094-SF40 UBR84

3.3 Coils

Current carrying copper coils are used in experimental setups to generate magnetic fields, e.g. to create a MOT (Sections 3.3.1, 3.3.2) or to control magnetic fields in the region of the atomic cloud.

Shim coils can compensate any residual field at the position of the atoms by creating an opposite magnetic field. The shim coils have co-propagating currents, which generates a magnetic field at the position of our atoms that increases linearly with the current in the coils. By varying the current in our coils we are able to generate a magnetic field opposite to the residual one and thus counter it.

The gradient coils generate the magnetic gradient which is required in a MOT (Section 2.2.3). The gradient coils are built in an approximately anti-Helmholtz configuration, where each coil is separated by the same distance to the point of interest, i.e. the atomic cloud, and have the same number of layers, windings per layer and radius although the current circulates in opposite directions. The atoms are in the centre between the coils. This configuration generates a quadrupole field with linear gradient [56], as required by the MOT.

3.3.1 2D MOT

For our two-dimensional Magneto Optical Trap (2D MOT) we need three pairs of shim coils and two pairs of gradient, or main, coils. In the case of our 2D MOT shim coils, the coils have a rectangular shape, as it is a better fit for our design of the glass cell and the optics. The dimensions of the 2D MOT shim coils for the horizontal plane axes are 67.4 mm $\times$ 179 mm $\times$ 5.7 mm, while the dimensions of the 2D MOT shim coils on the vertical axis are 102 mm $\times$ 94 mm $\times$ 10.6 mm. The 2D MOT shim coils for the vertical axis have 10 layers and 10 windings per layer, and the 2D MOT shim coils for the horizontal plane have 6 layers and 5 windings per layer. They are made of copper wire, with a thickness of 1 mm, and we employ a current no higher than 2 A to compensate the residual fields with fields up to 1 G.

For our 2D MOT gradient coils we also use copper wire and a rectangular shape. The gradient coils generate a quadrupole in the plane perpendicular to the propagation direction of the atoms. The thickness of the coil is 0.8 mm. The dimensions of the 2D MOT gradient coils are 36.4 mm $\times$ 165.4 mm $\times$ 12.5 mm. The 2D MOT gradient coils have 14 layers and 10 windings per layer. The 2D MOT gradient coils generate a gradient of 15 G/cm for a current of 2 A.

3.3.2 3D MOT Coils

As per our 2D MOT, we also require both shim and gradient coils for the 3D MOT. Due to the design of the 3D MOT chamber, all the coils employed there are circular in order to fit better with the design of the 3D MOT chamber. Copper wire of 0.8 mm diameter is used for the vertical shim coils, while copper wire of 1 mm thickness is

used for the rest of them. The radii of the 3D MOT shim coils differ depending on the axis they compensate, as the vertical shim coils have a radius of 56.5 mm and a height of 8 mm, the dipole axis shim coils have a radius of 70 mm and a height of 17 mm and the transport axis shim coils have a radius 49.5 mm and a height of 8.8 mm. We employ currents below 1 A on the shim coils, that can generate a field up to 1 G, but we ramp up the 3D MOT gradient coils to 6.5 A, generating a gradient of 13 G/cm for 1500 ms during the loading of the 3D MOT and up to 20 A for 18 ms in order to compress the 3D MOT by generating a higher magnetic gradient field of 41 G/cm.

3.4 Laser systems

In our laboratory the lasers can be classified as either "cooling"[6] (Sections 3.4.1, 3.4.3, 3.4.4, 3.4.2) or "trapping" (Sections 3.4.5, 3.4.6)[7]. While the former are mainly used for cooling and imaging purposes with frequencies close to the atomic transitions, the latter are used to create far-detuned Optical Dipole Traps (ODTs) and optical lattices.

Due to their different basic characteristics (functions, wavelength, power), the laser setups where our beams are tailored to the tasks we want to use them for are quite different.

In the case of the cooling lasers, as we want to control our frequencies with a high degree of precision and a narrow linewidth, the frequency of our cooling lasers is stabilised using atomic spectroscopy and an electronic locking scheme. Also, as their light is used in many stages of the experiment in quick succession or even simultaneously, they have several acousto-optical modulators (AOMs) and shutters to be able to have light on the required paths. The light is sent to the main experiment table through optical fibres. As of now, we only have the laser systems in place to cool ^{87}Rb, as we will add the cooling lasers for ^{85}Rb at a later stage (Chapter 6).

The "trapping" setups tend to be simpler and are located on the main experiment table, due to the fact that they output extremely high powers and the beams have to terminate in water-cooled heat dump. In addition, the laser frequencies are very broadband , e.g. IPG model YLR-200-LP-WC-Y14, so there is no need to have a frequency stabilisation system, as the laser light is already far detuned from resonance. Our high power fibre amplifiers are seeded by light with 1 kHz linewidth, and a frequency drift of 1 MHz/min.

3.4.1 Master laser

Our master laser provides a stable frequency with a narrow linewidth so the other lasers can lock onto this reference (Sections 3.5.3 , 3.6.1). It also provides light for the imaging of the atomic clouds (see Section 4.1) and the resonant push beam required to displace the atoms from the 2D MOT to the 3D MOT. As our master laser, we are using a cat-eye external cavity diode laser (ECDL) [8] [57]. The output power of the master laser after the isolator is approximately 60 mW. It is enough to power for the spectroscopy, the push beam setup, the absorption imaging setup and each of the beat signals (Figure 3.5). Our master laser is locked to the $F = 2 \rightarrow F' = 3$ transition of the D2 line of ^{87}Rb, with an additional blue detuning of 220 MHz (Figure 3.6).

We employ a commercial cat-eye ECDL for the following properties: ECDLs emit light with a stable frequency over long periods of time, they posses a narrow linewidth (Section 3.6.1) and they have a good price-performance relationship. The

[6] Up to 2 W in power.
[7] In the case Transport optical dipole trap, 50 W and in the CODT lasers, 200 W.
[8] Moglabs model CEL 002

laser cavity is composed of a laser diode, an étalon, a pair of lenses, two sets of piezoelectric components and the outcoupler. The external cavity extends from the diode to the outcoupler, unlike in the Littrow configuration ECDLs [58], in which together with the diode, the diffraction grating forms the cavity.

The linewidth of a free-running laser diode is typically in the range of a few MHz. That linewidth is too broad for our purposes, as we need to be able to address frequencies below the natural linewidth of the atomic transitions, $\Gamma = 2\pi \times 6.065(9)$ MHz [44]. In order to improve the linewidth of the laser, we create an external cavity, which adds additional constraints to the mode of the diode, allowing the selection by the étalon.

We select the frequency by rotating the étalon, by controlling the length of the cavity with our piezoelectric and by controlling the current and temperature of the diode. Rotating the étalon shifts the filter to higher or lower frequencies, while changing the cavity length displaces the cavity modes. Changing the diode current and temperature moves the diode mode to higher or lower frequencies.

By fine-tuning these parameters, we select a mode with the desired frequency over a large mode-hop free range[9].

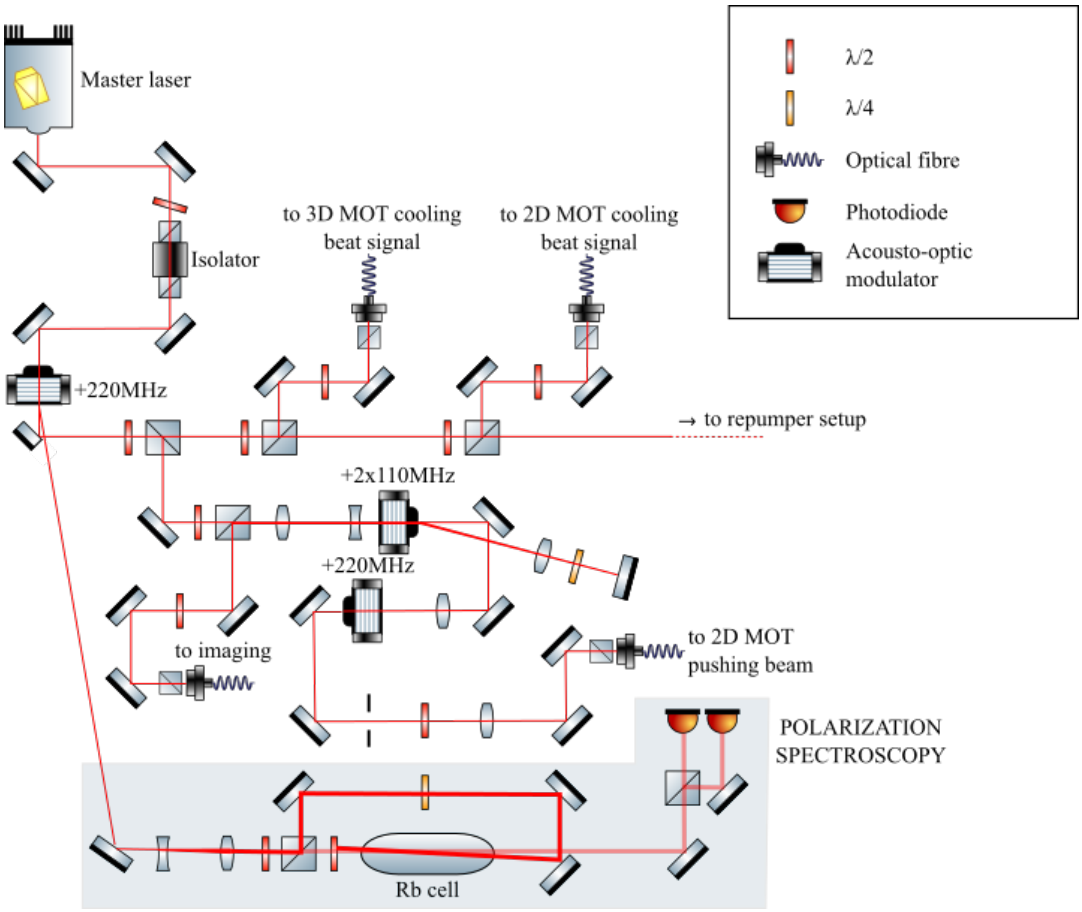

FIGURE 3.5: Scheme of the master laser setup.

[9] Wider than the whole 7 GHz of the Rb D2 line spectrum.

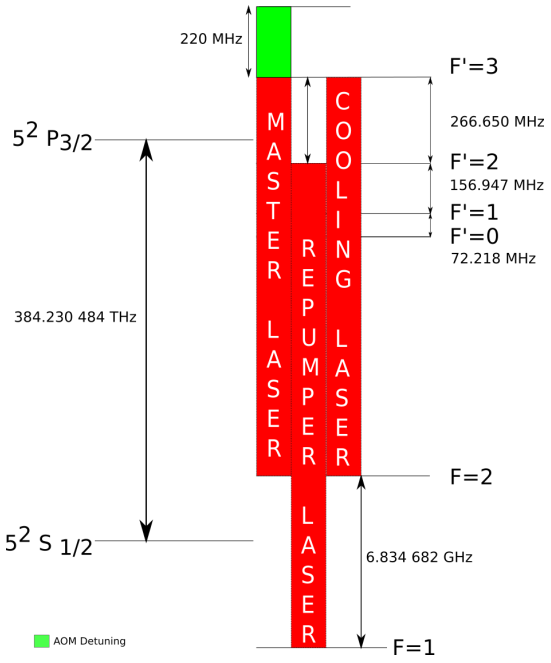

FIGURE 3.6: Transitions used by the current lasers of the experiment, with their respective detunings. Transition frequencies from the figure taken from [44].

3.4.2 Repumping laser

Optical cooling transitions are often not closed. The atoms might decay into unwanted states. For example, magneto-optical traps (MOTs) of ^{87}Rb work on an almost closed transition (Figure 3.6). With just a cooling laser from $F = 2 \rightarrow F' = 3$ on the D2 line of ^{87}Rb there is a chance of the atoms being pumped to the $F' = 2$ state and decaying from $F' = 2 \rightarrow F = 1$. By implementing a laser in the $F = 1 \rightarrow F' = 2$ transition, the $F = 2$ state cannot be depleted and the transition is truly closed.

The repumping is locked to the $F = 1 \rightarrow F' = 2$ transition of the D2 line of ^{87}Rb with an offset lock scheme (Section 3.5.3). For our offset lock we create a beat note of the light of the repumping and master lasers. To cover the frequency difference of 6.348 GHz[10], we employ a signal generator to create a 2.924 GHz signal, doubling it with a frequency doubler and mixing this signal with the beat note from the Master laser so the frequency to voltage converter (FVC) receives a signal in its working range of 100 MHz to 1 GHz (Figure 3.8). More details can be found in Section 3.5.3.

The Repumping laser is also a cat-eye ECDL [11]. A series of $\lambda/2$ waveplates and Polarising Beam Splitters (PBSs) divert the repumping light to the 2D MOT Repumper, 3D MOT Repumper, Optical Pumping and Imaging Repumper paths. We use acousto optical modulators (AOMs) for frequency shifting and fast switching of the light (Figure 3.7).

[10] The hyperfine structure splitting, 6.834 GHz, minus 220 MHz as the master laser is blue detuned from the $F = 2 \rightarrow F' = 3$ transition (Figure 3.6).

[11] Moglabs model CEL 002 [57]

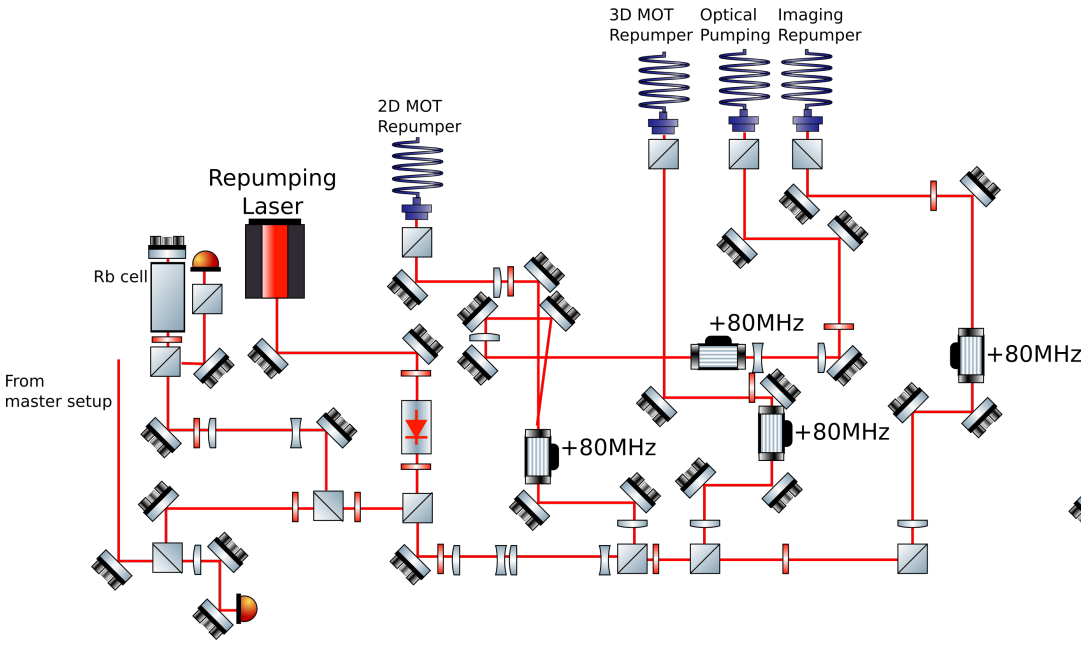

FIGURE 3.7: Scheme of the Repumping laser setup.

3.4.3 2D MOT cooling laser

Having a large flux of atoms from the 2D MOT glass cell towards the 3D MOT chamber is crucial for our experiment. A large 2D MOT trap volume guarantees the high flux of atoms and in order to sustain a large trap volume, the power supplied by a diode laser is not enough. A combination of ECDL and tapered amplifier (TA) for our 2D MOT cooling laser offers the required amount of power, above 1 W. As our

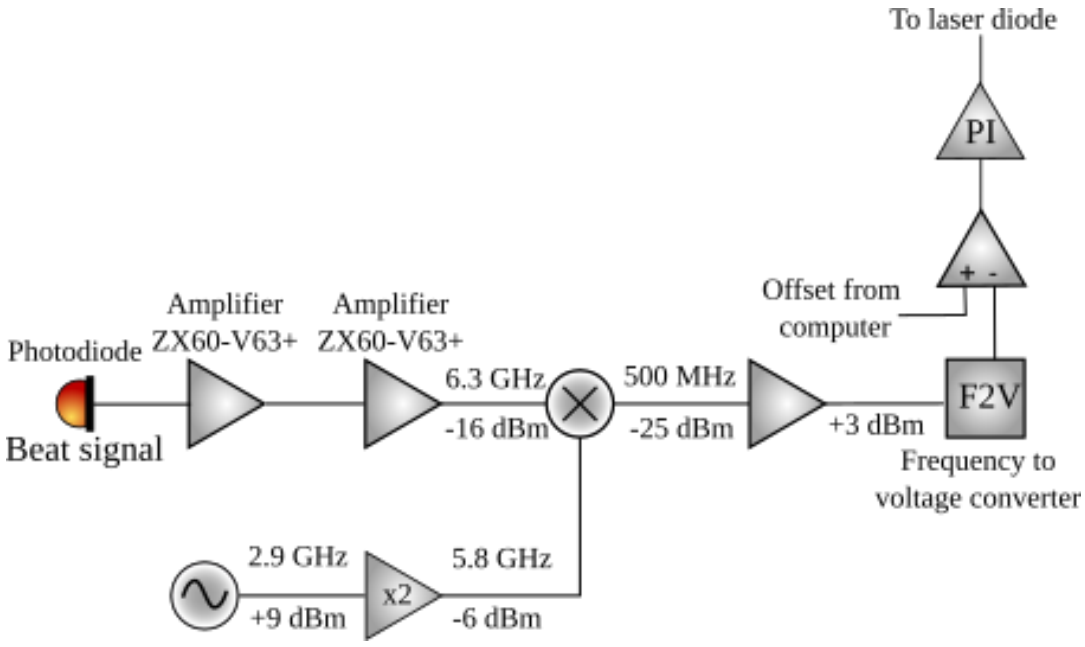

FIGURE 3.8: Signal processing for the offset lock of the repumping laser.

2D MOT cooling laser, we employ a combination of External Cavity Diode Laser [12] and Tapered Amplifier [13]. The ECDL feeds the TA, which amplifies the incoming light up to 1.5 W. The outcoming beam is then overlapped with light from the Repumping laser setup and split between 2D MOT axial Cooling and 2D MOT cooling 1 and 2 (Figure 3.9).

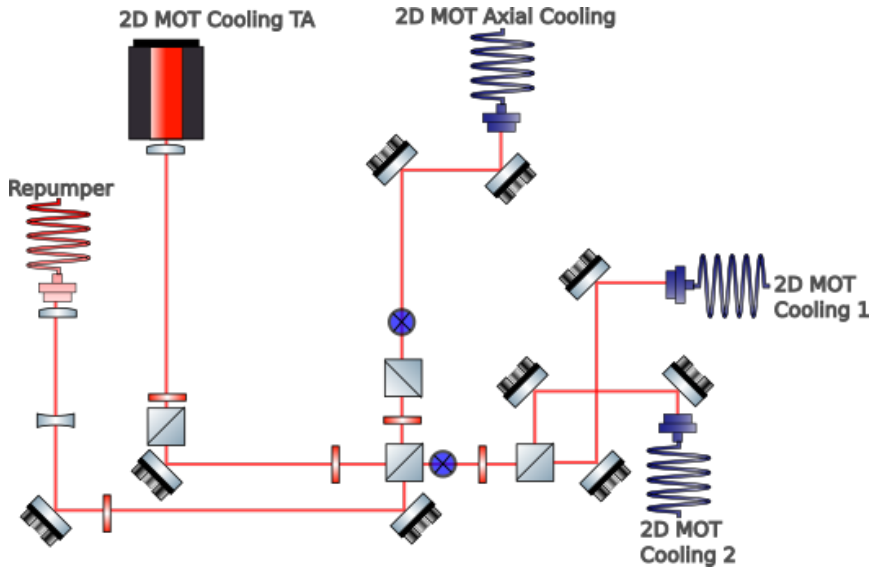

FIGURE 3.9: Scheme of the 2D MOT cooling laser setup.

The frequency of the 2D MOT cooling laser is two natural linewidths (2Γ) red detuned from the $F = 2 \rightarrow F' = 3$ transition of the D2 line of ^{87}Rb. As illustrated in Figure 3.6, the 2D MOT cooling laser is detuned by about 235 MHz from the master laser; which is itself 220 MHz blue detuned from the $F = 2 \rightarrow F' = 3$ transition of the D2 line of ^{87}Rb (Figure 3.6); and well within the 0.1 GHz to 1 GHz range of the FVC. Using an offset locking scheme similar to the one for the repumping laser (Section 3.6.2), we lock the 2D MOT cooling laser to the desired frequency. The beat note from the master laser and the Toptica ECDL is fed into a fast photodiode, which is sent to the FVC. We use a proportional integrator (PI) regulator to regulate the frequency so it is possible to lock the laser to the desired frequency (Section 3.5.3).

[12] ECDL; DL Pro, M-30 Version 06 from Toptica
[13] TA; TA ProM-041 Version 04 from Toptica

3.4.4 3D MOT cooling laser

The higher the atom number we capture in our 3D MOT, the more atoms we will start our evaporation process with (Section 5.1.3). As in our 2D MOT cooling laser (Section 3.4.3), we employ a combination of ECDL and tapered amplifier (TA) in order to relay approximately 300 mW of power for our 3D MOT (Figures 3.10 and 3.11). Other uses of the 3D MOT cooling setup are supplying light for imaging (Section 4.2.2), grey molasses (Section 4.4) and the fluorescence imaging of the atoms in the optical lattice (Chapter 6). Our 3D MOT cooling setup is a combination of an ECDL [14] and a tapered amplifier (TA) [15]. The 3D MOT cooling laser setup is divided in two different sections, the seed (the EDCL mentioned above) laser and tapered amplifier (TA) sections. The seed laser section comprises of the spectroscopy setup, offset lock and fibre coupling into the TA. The 3D MOT cooling ECDL is offset locked (Section 3.5.3) with the master laser similar to the 2D MOT cooling (2Γ red detuned from the $F = 2 \rightarrow F' = 3$ transition of the D2 line of ^{87}Rb, Figure 3.6) and using the same offset locking technique. We overlap light from the master laser with light from the 2D MOT ECDL on a fast photodiode in order to generate a beat note (Figure 3.10).

To amplify several sources of light simultaneously, we overlap them before the TA (Figure 3.10). As of now, we have light for the 3D MOT cooling light of ^{87}Rb , which is fed into a fibre electro optical modulator (EOM) and then into the TA. In the future we will add light for the 3D MOT cooling of ^{85}Rb (Chapter 6). The EOM is used to create sidebands on the $F = 1 \rightarrow F' = 2$ repumping transition during the grey molasses phase, as explained in Section 4.4.

In the tapered amplifier section (Figure 3.11), we fibre couple part of the light to use as the cooling light in our 3D MOT. We also divert part of the light into the Optical Pumping path of the Repumper setup and, generate the molasses cooling light that will be used to take fluorescence pictures of the atoms in the optical lattice with the microscope (see Chapter 6).

[14] Moglabs model CEL 002
[15] Thorlabs TA780P20

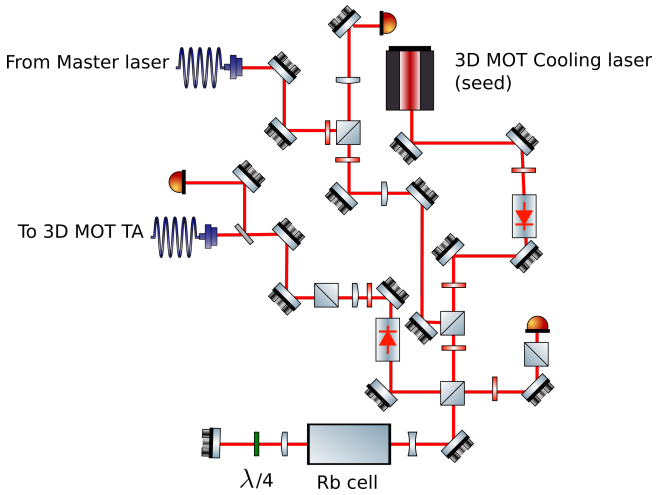

FIGURE 3.10: Diagram of the 3D MOT seed laser section of the 3D MOT cooling setup.

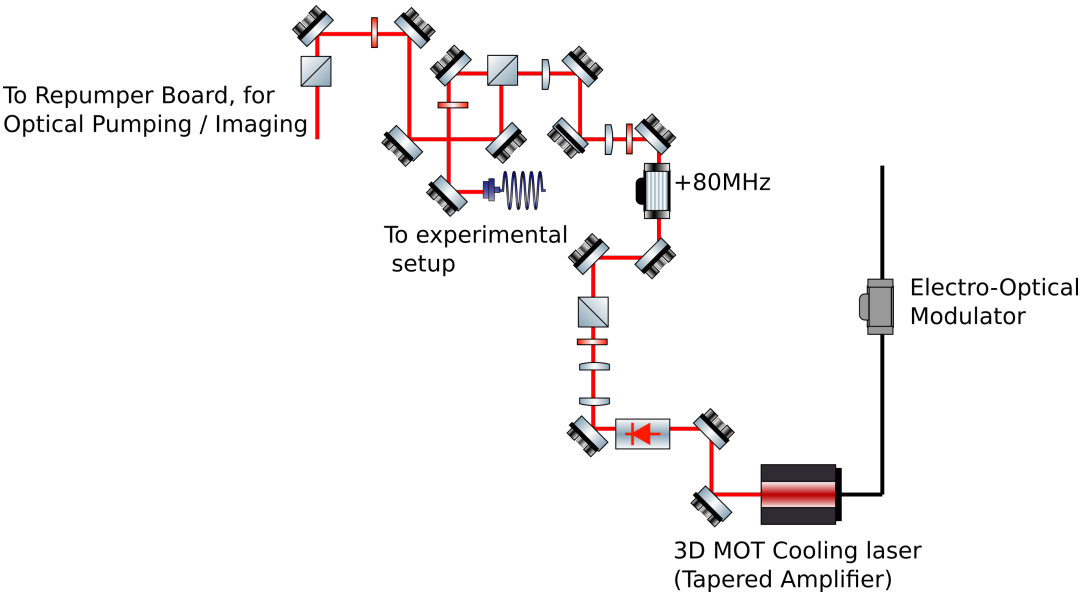

FIGURE 3.11: Diagram of the tapered amplifier section of the 3D MOT cooling setup.

3.4.5 Crossed Optical Dipole Trap lasers

After our grey molasses phase (Section 4.4), we trap a fraction of the atomic cloud in a crossed optical dipole trap (CODT) with a high trapping volume. To avoid heating up the atoms while still having a good trap depth and volume, we decided to use extremely high powers, a waist close to 300 µm and a detuning of approximately 300 nm (Section 2.2.4). For our crossed optical dipole trap (CODT), we use two industrial-grade, 1064 nm lasers with a maximum output of 200 W[16]. For a power of 150 W in each beam and the aforementioned waist, we obtain a trap depth of approximately 350 µK (Equation 2.8). We terminate the CODT beam paths in water cooled beam dumps, as pictured in Figure 3.12. Measurement results of atom numbers and temperatures after loading into the CODT are discussed in more detail in Section 5.1.1.

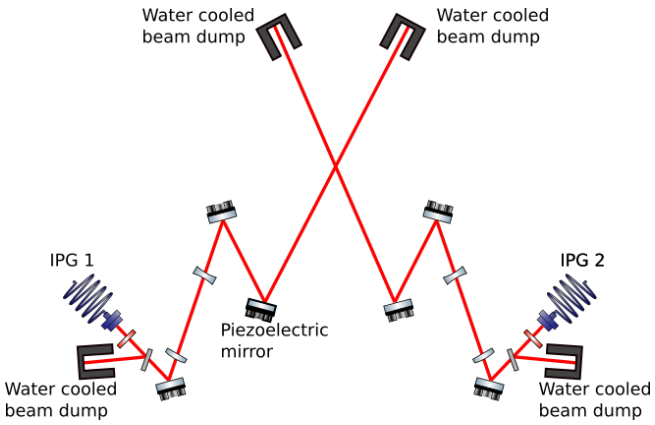

FIGURE 3.12: Schematic of the setup used to create the CODT.

One of our dipole trapping beam paths (IPG 1, Figure 3.12) has a piezoelectric mirror to align the beam onto the centre of the MOT. We control the position of the centre of the MOT cloud by varying the currents on the 3D MOT shim coils and so maximise the number of atoms loaded into the CODT.

3.4.6 Transport optical dipole trap laser

One of the future goals of our experiment is to image single atoms in optical lattices. This will be achieved in the Science chamber, which is approximately 25 cm away from the 3D MOT chamber. To transfer the atoms from the MOT chamber to the Science chamber we trap them in a tightly focused dipole trap and then displace the focus using a mechanical translation stage[17]. As our laser source we use a Nd:YAG fibre amplifier [18], seeded by a narrow-linewidth solid state Nd:YAG[19]. In order to have better control during the loading and transport of the atoms, we regulate the intensity on our so-called "Transport Optical Dipole Trap" (TODT) with a feedback

[16] IPG model YLR-200-LP-WC-Y14.
[17] Thorlabs DDS220/M.
[18] Azur ALS-IR-1064-50-A-SF.
[19] Coherent Mephisto 1000

loop. Our beam is focused to $\approx$ 50 µm and has a power of $\approx$ 20 W. Thus, the expected trap depth is 150 µK (Section 5.1.1).

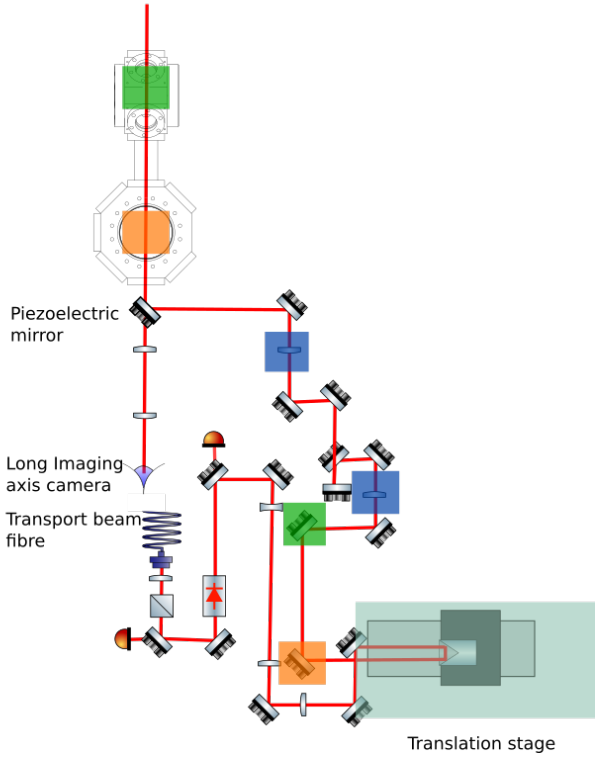

FIGURE 3.13: Schematics of the Transport Optical Dipole Trap (TODT) setup. The difference in beam path between the Translation stage at the "MOT position" and at the "Science Chamber position" is equal to the distance between the mirrors M1 (orange box) and M2 (green box). The distance between the two relay lenses (blue boxes) equals $2f_{Relay}$, as they are a 1:1 telescope.

Aligning the tranport trap is a complex matter. We need to be able to displace the focus of the transport trap from the centre of the 3D MOT chamber to the centre of the Science chamber, which are separated 25 cm apart, with repeatability. In order to do so, we rely on a focusing scheme to relay the focus from the mirrors, M1 and M2, to the chambers and we employ a mechanical translation stage to displace the focus between the chambers. The focusing scheme is known as $4f$, as the total distance is four times the focal distance of the lenses used for relaying the focus from the initial mirror to the chamber. So as to avoid altering the magnetic landscape near the vacuum chamber, the laser amplifier needs to be as far away from the vacuum chamber as possible. That, plus the need to centre the focus of the beam at both the MOT and Science chambers, motivates the implementation of a focus relaying system.

In Figure 3.13 we show in detail the diagram of the TODT. Depending on the position of the retroreflecting cube in our translation stage, the TODT is focused either on M1 (orange box) or in M2 (green box). The distance between the two mirrors is equal to the distance between the centre of the MOT and Science chambers.

In order to translate the focus to the chambers from the mirrors, we use a focus relay system. It consists of two lenses (f_{Relay}) of equal focus, separated by $2f_{Relay}$ and where the distance from the first relay lens to M1 equals the distance from the second relay lens to the Science chamber.

3.5 Locking systems

To stabilise the laser frequencies and avoid frequency drifts over time we need to implement a frequency locking scheme.

In this section, we will describe our two spectroscopy methods, saturation absorption spectroscopy (Section 3.5.1) and polarisation absorption spectroscopy (Section 3.5.2), and the locking of our external cavity diode lasers (ECDL) to the master laser via offset locking (Section 3.5.3).

3.5.1 Saturated absorption spectroscopy

In order to provide visual feedback for our offset locking schemes and due to its simplicity, we implemented a saturated absorption spectroscopy scheme in our 2D (Section 3.4.3) and 3D MOT (Section 3.4.4) cooling lasers, and our repumping laser (Section 3.6.2). By the absorption of light in a rubidium vapour cell, we can observe the optical transitions in a Doppler-free spectrum, in which it is possible to resolve the crossover peaks and the hyperfine levels [43, 59].

For the setup of a typical saturation spectroscopy, the beam path is illustrated in Figure 3.14. It requires two beams of different intensities and orthogonal linear polarisations, which we will denote as pump and probe beams. The pump beam passes through the rubidium vapour glass cell. It is then retroreflected, attenuated by an optical density (OD) filter and has its polarisation rotated by $\lambda/2$. It passes again through the rubidium glass cell and its light is collected in a photodetector.

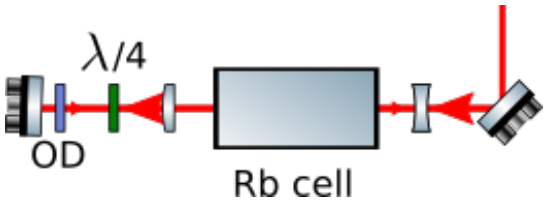

FIGURE 3.14: Diagram of a saturation absorption setup. The intensity of the beams is indicated by the size of the arrows, showing the propagation direction. OD stands for optical density filter.

Thermal atoms in an atomic cloud will have different velocities. The pump (probe) beams will be either blue or red-shifted for different atoms due to the Doppler effect. In our diagram (Figure 3.14), the pump beam comes from the right of the cell and the probe from the left. Atoms moving towards the right (left) part of the cell will feel the pump (probe) beam being blue detuned while the probe (pump) will be red detuned. Thus, depending on their velocities, atoms will be excited by

either of the beams, but never by two of them simultaneously, except for those with velocity equal to zero in the beam propagation axis when the pump and probe beams are resonant to the transition [55].

For a resonant beam (frequency equal to ω_0), those atoms will be excited by both pump and probe. If we measure our probe signal with no pump beam present, after passing through the atomic cloud, we will observe a Doppler broadened dip, as different atoms with different velocities will be excited. When we have both pump and probe present, the pump beam, being closer to the saturation intensity [44] than the probe, will excite most of the resonant atoms, and thus the atomic cloud will be partially transparent to the probe beam. In our photodiode, we will measure the Doppler broadened dip with a central peak, corresponding to the frequency of an atomic transition. The peak is caused by the atoms excited by the pump that are transparent to the probe beam and therefore the light is not absorbed by the atoms. The height of the peak depends to the intensity ratio between pump and probe.

3.5.2 Polarisation spectroscopy locking

To lock the frequency of our master laser (Section 3.4.1) we use polarisation spectroscopy.

It is similar to saturation absorption spectroscopy system, since it relies on a pump-probe scheme (Figure 3.15). The pump beam pumps the atoms to the stretched m_F state[20] through a σ_+ transition. This creates birefringence for the linearly polarised probe, that is, different polarisations will have different indices of refractions. A linearly polarised beam is equivalent to the superposition of two opposite circularly polarised beams and so the left and right handed polarised beams will have different indices of refraction [60, 55]. This results in a retardation of one of the polarisations relative to the other and it will result in a rotation of the linear polarisation of the probe beam and, there will be an imbalance between the light measured in the photodiodes. By substracting one photodiode signal from the other, we obtain the error signal, which has a Fano-like profile. Only when the light is in resonance with the desired transition, the error signal will be equal to zero and can be used as the reference point in our laser control feedback loop (Section 3.4.1). As we can see in Figure 3.15, we measure the probe beam with two photodetectors after the rubidium cell, by using a PBS to split the vertical and horizontal components of the polarised light. We set the polarisation of the probe beam at 45°, so that in the absence of a pump beam each photodetector receives the same amount of light.

3.5.3 Offset locking

In several points in our experimental sequence (Sections 4, 5) we require control over the frequencies of the lasers, with the exception of the master which always remains

[20] In the case of the $F = 2$ ground state of ^{87}Rb, the $m_F = \pm 2$ state.

as a frequency reference for the rest. We are able to control the frequencies of the lasers by offset locking the to the master laser.

A beat note is created by overlapping the beam from the master laser and the beam from the slave laser on a fast photodiode[21]. The beat note is amplified and sent to the frequency to voltage converter (FVC), which is an operational amplifier that outputs voltage proportional to an input frequency. To generate an error signal for the proportional integral (PI) regulator, another operational amplifier adds the output voltage of the FVC to an offset voltage from our experiment control software.

In this way, we can vary the position of the zero crossing of the error signal and thus change the frequency of our laser.

The range of possible input frequencies of the FVC are 100 MHz to 1 GHz, so the master laser and the slaves need a detuning of at least 100 MHz. The cooling laser also serves as an optical pumping laser, on the $F = 2 \rightarrow F' = 2$ transition, and as a grey molasses cooling laser, which needs to be between the $F = 2 \rightarrow F' = 2$ transition and the $F = 2 \rightarrow F' = 3$ transition.

[21] Hamamatsu G4176-03 MSM photodetector

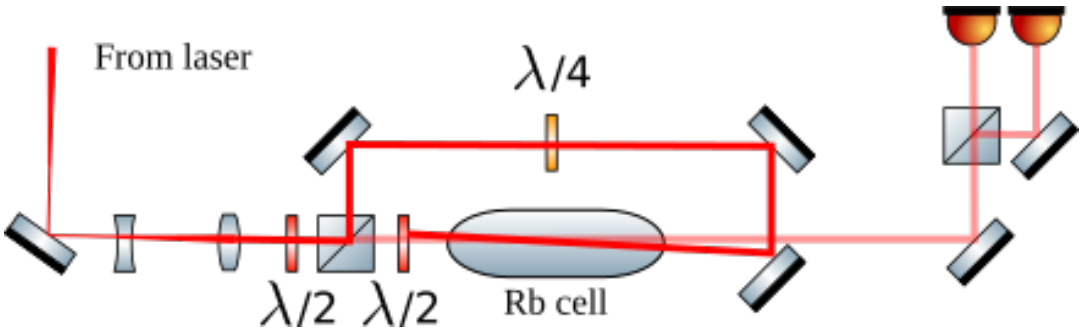

FIGURE 3.15: Polarisation spectroscopy setup.

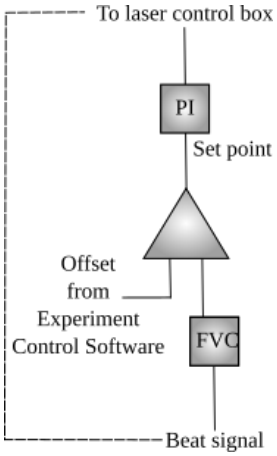

FIGURE 3.16: Scheme of the offset lock setup. The beat signal is the result of the detuning between the master and slave lasers' frequencies. The FVC converts it to a voltage, which is then added to an offset controlled by the Experiment Control Software . The resulting voltage acts as the set point of the proportional integrator (PI) feedback loop that regulates the slave laser's frequency.

To be able to create beat signals that are within the range of the FVC, the master laser is locked 220 MHz blue detuned from the $F = 2 \rightarrow F' = 3$ transition of the D2 line of ^{87}Rb, to a polarisation spectroscopy signal (Figure 3.6). In Sections 3.6.2 and 3.6.3 we offer a characterisation of the bandwidths, i.e. the speed at which we can controllably switch the frequencies of the offset locked lasers.

3.6 Characterisation of the laser systems

In this section we characterise our laser stystems. For our laser systems for MOT and molasses cooling, optical pumping, and imaging, we determine the precision and the speed of frequency changes, i.e. we measure the linewidth (Section 3.6.1) and the bandwidth (Sections 3.6.2, 3.6.3) of our cooling and repumping laser systems.

3.6.1 Linewidth of the Master laser

We take as the linewidth of our master laser the standard deviation of frequency fluctuations whilst the laser is locked. The measurement process consists of three steps, which aim for a quantitative determination of the frequency fluctuations.

In a first step, we calibrate the spectroscopy signal (Figure 3.17) by relating time-difference and frequency-difference in the spectrum. The spectrum shows the hyperfine peaks at the position of the transitions $F = 2 \rightarrow F' = 3$ and $F = 1 \rightarrow F' = 2$. As we know the frequency difference to be 6.5680 GHz, we can convert the data from a time scale to a frequency scale. The difference between the $F = 2 \rightarrow F' = 3$ and $F = 1 \rightarrow F' = 2$ peaks is the hyperfine structure splitting of the ground state of ^{87}Rb minus the difference between the $F' = 2$ and $F' = 3$ hyperfine states [44].

In a second step, we fit a line (Figure 3.18) to the zero crossing of the error signal at the transition $F = 2 \rightarrow F' = 3$.

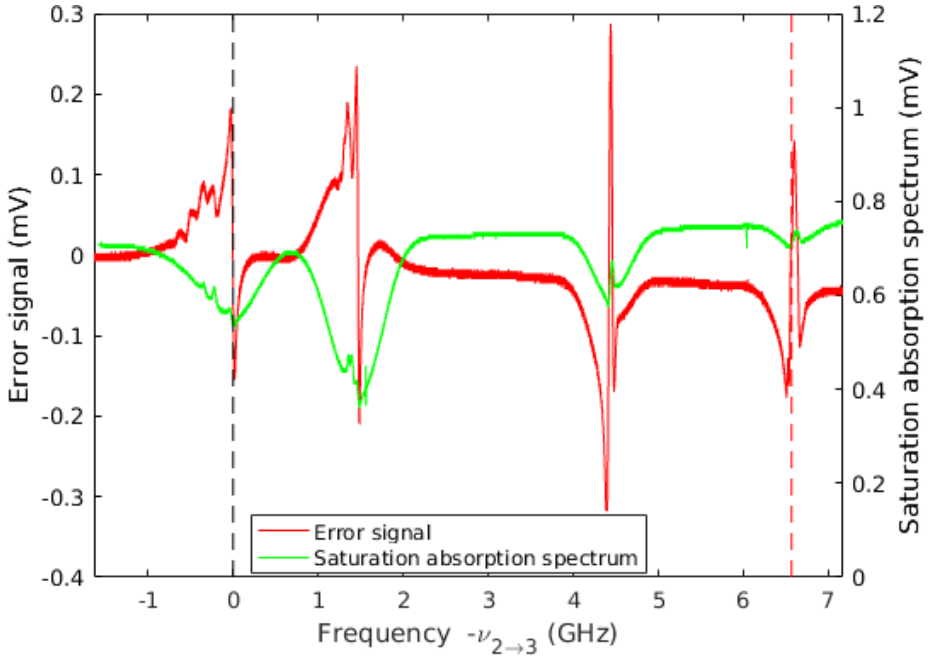

FIGURE 3.17: Saturation absorption spectrum (red) and error signal (green) for ^{87}Rb and ^{85}Rb. The difference between the $F = 2 \rightarrow F' = 3$ (blue dashed line) peak and the $F = 2 \rightarrow F' = 2$ (red dashed line) is the hyperfine splitting structure of ^{87}Rb minus the difference between the $F' = 2$ and $F' = 3$ hyperfine states.

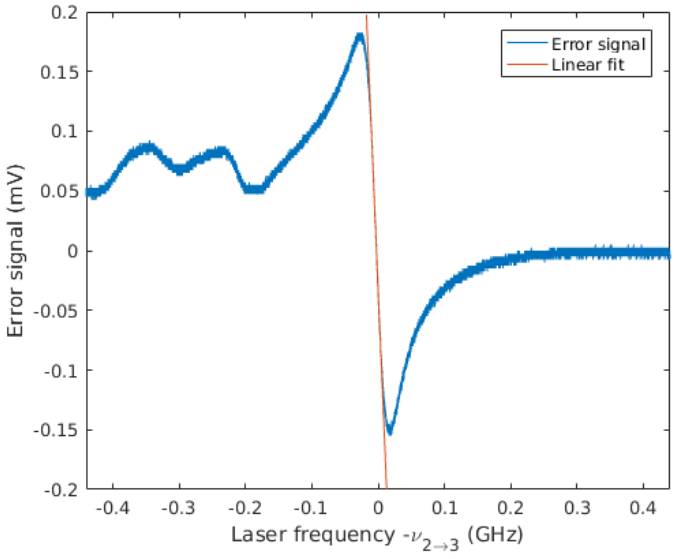

FIGURE 3.18: Calibration of the voltage in frequency units by a linear fit on the zero crossing of the $F = 2 \to F' = 3$ transition of ^{87}Rb.

Finally, using the slope of the linear fit, we convert the voltage of the error signal of our locked laser to frequency. We also measure both the mean value and the standard deviation of the error signal (σ). The linewidth is considered to be 2σ (272.4 kHz) centered on the mean value (see Figure 3.19). For this measurement we employed 2×10^7 datapoints for the calculation of the mean and the standard deviation, but we only plotted approximately 2000 of them in order to show the noise in the data.

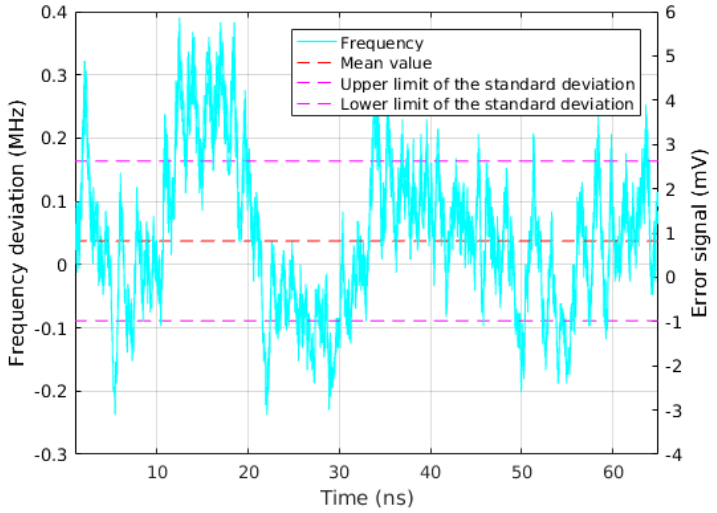

FIGURE 3.19: Frequency deviation of the master laser when locked.

3.6.2 Bandwidth of the Repumping laser offset lock

We require fast changes of the laser frequencies at different stages fo the expeirmental sequence, e.g. to detune the frequency of the MOT light for a compression phase. We need bandwidths on the order of 100 Hz for switching times of 10 ms.

The determining factors for our regulation bandwidth, are the bandwidth of the FVC, and the bandwidth of the feedback loop. The slower of the two will be the limiting factor and will dictate the total bandwidth of the system.

We optimize the gain parameters of FCV and laser regulation box for maximum speed, and they stay below the threshold of ringing. Our measurement results are illustrated in Figure 3.20. It shows the frequency change (red line) and the resulting error signal (blue line). We measure the bandwidth by changing the frequency of the offset lock from 200 MHz to 300 MHz and back to 200 MHz. The error signal stabilises after 3.00 ms, which we define as the switching time. The corresponding bandwidth is 333 Hz.

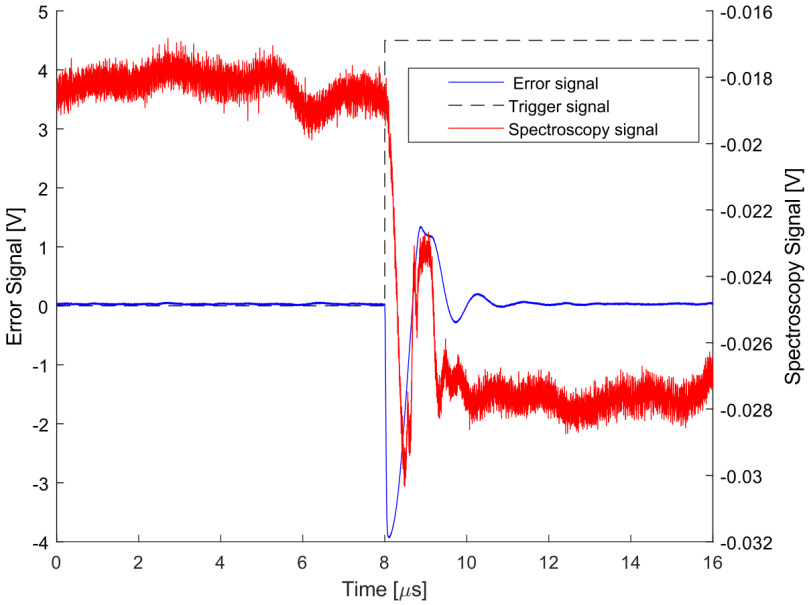

FIGURE 3.20: Bandwidth measurement of the offset lock of the repumping laser. The error signal is the blue line and the spectroscopy signal is the red line, while the dotted red lines denote the trigger used to change the frequency signal. The offset lock bandwidth of the repumper laser is 333 Hz.

Both the spectroscopy (red) and the offset lock (blue) signals are recorded in figure 3.20 to show how small changes in frequency result in a change of the spectroscopy signal. This is analogous to displacing the lock left or right of the spectroscopy peaks in figure 3.17.

3.6.3 Bandwidth of the 2D MOT cooling lasers offset lock

We apply a similar measurement scheme as in Section 3.6.2 for our 2D MOT cooling laser. To measure the bandwidth of the 2D MOT cooling offset lock, we use the same 100 MHz switch between 200 MHz and 300 MHz. Its laser control box (Toptica DL Pro M-30) was adjusted so the ECDL worked just below the ringing threshold. The

measured switching speed was 1.6 µs and the bandwidth was approximately 620 Hz (see Figure 3.21).

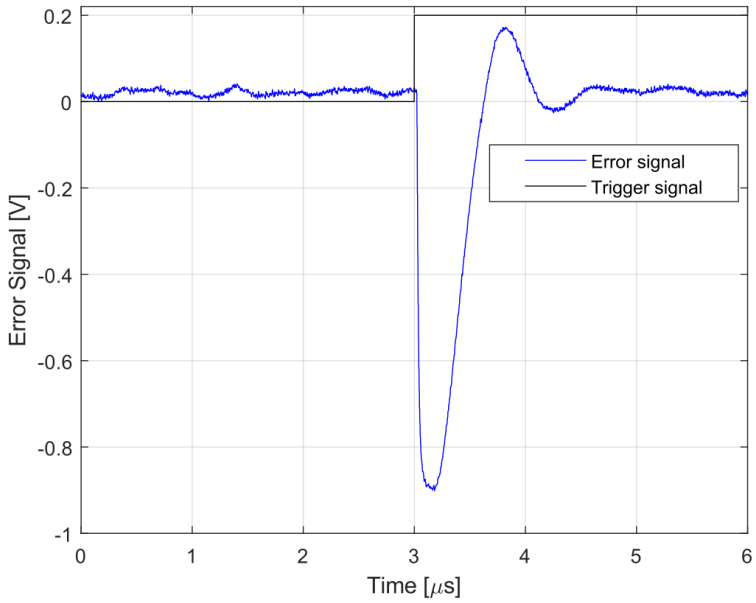

FIGURE 3.21: Bandwidth measurement of the 2D MOT cooling laser. The blue line denotes the error signal and the black line the trigger used to change the frequency. The offset lock bandwidth of the 2D MOT cooling laser is 618 Hz.

The 2D MOT cooling laser and the Repumping laser have a bandwidth of $\sim$ 620 Hz and 333 kHz, respectively. The reasons for the variations in bandwidth lie in the particularities of the electronics of each system. The Repumping laser has additional signal processing electronics (Section 3.6.2) to be able to use the FVC (Section 3.4.2). The 2D MOT cooling laser uses a Toptica controller and, it using a completely different set of electronics, also explains why it is two times as fast as the Repumping one.

3.7 Experiment control

Up to now, we have presented a description of the hardware side of the experiment, e.g. the vacuum chamber, the laser systems, but without a device to program and send precise instructions to our different devices we would not be able to cool and trap our atoms. In this section we will briefly summarise the different elements that conform our software, how they are connected with each other and the means we use to rely the instructions from the experimental sequence.

3.7.1 Software description

The control and analysis process for our experiment setup is divided into several tasks and implemented on several computers. User input is based on a channel/time matrix, where row corresponds to a channel and each column indicates a time interval in the experiment control software. We employ an external system [22] to generate analog ± 10 V and digital (TTL) signals. The system posseses 48 analog and 40 digital channels. It outputs signals with a time resolution of 2 µs. The experiment control software also sends a string with metadata and a trigger to the image acquisition software, which proceeds to take the pictures of the atomic cloud (Section 4.1) and prepares them for analysis. The image analysis software produces the image with the relevant data, e.g. atom number, size of the atom cloud, position of the cloud. The data is relayed into the data analysis software, where we plot it and study it. Figure 3.22 shows the corresponding flowchart of the data capturing process.

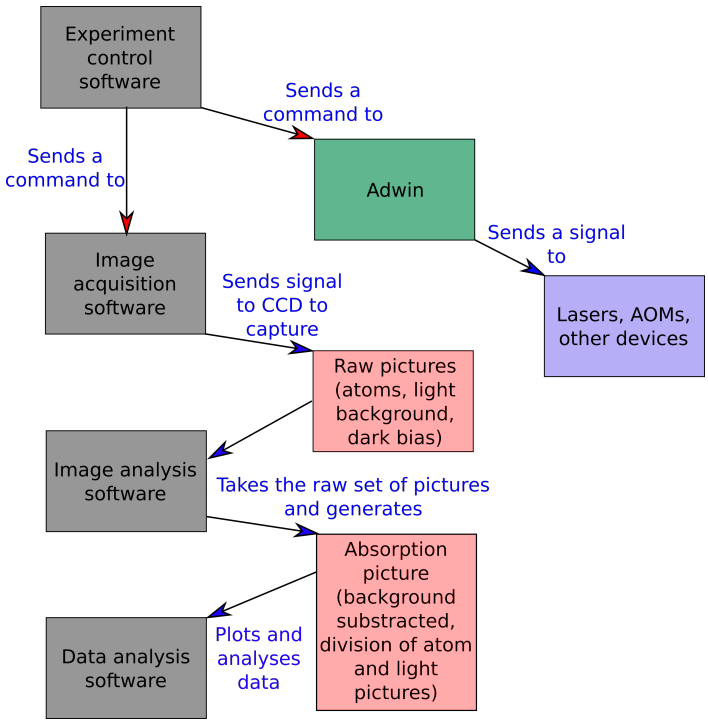

FIGURE 3.22: Flowchart of the data acquisition process.

[22] Adwin Pro II

Chapter 4

Initial trapping stages: Magneto optical traps and molasses cooling

In this chapter we will discuss our imaging systems and will describe the initial cooling and trapping of the atoms before loading the atoms in the crossed optical dipole trap (CODT), where we will continue to cool them down. We will present the atom number and temperature measurements and results relevant for this chapter.

To characterise the atomic cloud through the different stages of our sequence we use time-of-flight absorption imaging (Section 4.1) to ascertain the number of atoms in the cloud (Section 4.1.1) and their temperature (Section 4.1.2). We describe the characteristics and layout of our different imaging setups in the 3D MOT chamber in Section 4.2. Before loading rubidium atoms in the Crossed Optical Dipole Trap (CODT) and evaporating them in order to create a Bose-Einstein condensate (BEC), we cool and trap them in our Magneto Optical Traps (MOT, Section 4.3). The atoms are cooled from room temperature to mK temperatures in the 2D MOT chamber (Section 4.3). We use a resonant beam to push them down through a differential pumping tube and recapture them in the 3D MOT chamber (Section 4.3). After further cooling by a red and grey molasses phase (Section 4.4), we load the atoms in the CODT (Section 5.1.1).

4.1 Time-of-flight absorption imaging

The technique we use in our experiment to evaluate the status of our atomic clouds is time-of-flight absorption imaging [61, 62, 55, 47]. The basic idea behind absorption imaging is that we do not image the atomic cloud directly but rather its shadow when illuminated with resonant light (Figure 4.1). The configuration of lenses that we use is known as a $4f$ configuration, as the lenses are separated by the sum of their focal distances.

The term time-of-flight refers to the fact that we do not image the atoms in situ but rather a few milliseconds after they have been released from their trap into free space. The optical density of an atomic cloud is defined as the capacity to absorb the incoming light and it depends on the integrated density of the atomic cloud. In the case of MOTs and BECs, their optical densities are so high that no light reaches

the Charge-Coupled Device (CCD) sensors and thus we are unable to determine an atom number (Figure 4.3, Section 4.1.1). Thus we image the cloud after a certain time-of-flight. As the cloud expands, its optical and atomic densities decrease and then we can measure accurately the atom number.

Time of flight absorption imaging is also used to determine the temperature of the atomic cloud by measuring the width of the cloud for several expansion times (Section 4.1.2).

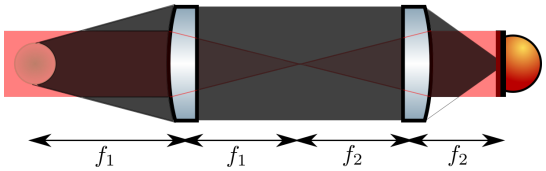

FIGURE 4.1: Diagram of the lens system used for absorption imaging, f_1 and f_2 are the focal distances for the first and second lenses.

4.1.1 Atom number measurements

We take three pictures of an atomic cloud to calculate its atom number. A picture of the imaging beam and the shadow of the atomic cloud ($I_A(x,y)$), a picture with just the imaging beam light ($I_0(x,y)$) and finally a picture with no light whatsoever (I_{bias} or dark picture). We subtract the dark picture from the previous two pictures to remove any bias due to noise in the sensor of the CCD camera. Then, by dividing two intensities, $I_0(x,y)$ and I_A, we are able to measure the column density in a logarithmic scale, and thus obtain the atom number from it (Figure 4.2).

The transmitted intensity of a light beam, $I_A(x,y)$, propagating in the $\hat{\mathbf{z}}$ axis after an atomic cloud is:

$$I_A(x,y) = I_0(x,y)e^{-D(x,y)}, \tag{4.1}$$

with $I_0(x,y)$ the initial intensity of the light beam and $D(x,y)$ the optical density. We take an additional picture with no incident light and thus rewrite the previous equation as:

$$I_A(x,y) - I_{\text{bias}} = (I_0(x,y) - I_{\text{bias}})e^{-D(x,y)}, \tag{4.2}$$

where I_{bias} is the electronic offset (or bias). If we solve the previous equation for $D(x,y)$, the optical density, we obtain:

$$D(x,y) = -\log\left(\frac{I_A - I_{bias}}{I_0 - I_{bias}}\right). \tag{4.3}$$

We can also define the optical density as [63]:

$$D(x,y) = D_0(x,y)\frac{1}{1 + \frac{I}{I_{\text{sat}}} + \frac{4\Delta^2}{\Gamma^2}} \tag{4.4}$$

with I_{sat} the saturation intensity, Γ the natural linewidth and Δ the detuning.

$$D_0(x,y) = 2\sigma_0 \int_z n(x,y,z)dz = 2\sigma_0 \tilde{n}(x,y) \tag{4.5}$$

$D_0(x,y)$ is the optical density in the resonant case and for intensities well below I_{sat}. It is proportional to the column density $\tilde{n}(x,y)$ along the $\hat{\mathbf{z}}$ axis and to the resonant cross section, σ_0.

In the resonant case ($\Delta = 0$) and for intensities below the saturation intensity, we can equate Equations 4.5 and 4.3 in order to obtain the column density, and from it the atom number. The resonant scattering cross-section, σ_0, is:

$$\sigma_0 = \frac{3\lambda^2}{2\pi} \tag{4.6}$$

where λ is the wavelength of the atomic transition. We calculate the atom number from our optical density using the resonant scattering cross-section and the magnification of our imaging system. By measuring the column density ($\tilde{n}$) at every pixel and dividing it by the area of a pixel (A_{px}), we obtain the atom number at each pixel. The magnification of an optical system is defined in Equation 4.11. Knowing the pixel size of the CCD camera and the magnification, we can obtain the area of a pixel measured in the atom chamber as $A_{px} = L_{px_x} L_{px_y}$. The atom number, n, is then:

$$n = -\log\left(\frac{I_A - I_{bias}}{I_0 - I_{bias}}\right)\frac{1}{\sigma_0} A_{px} C \tag{4.7}$$

where C is the Clebsch-Gordan coefficient of the transition.

When imaging with σ_+ (σ_-) light, the atoms are in a stretched state and we can treat the transition as an ideal two-level atom. The system then becomes a closed transition and thus the Clebsch-Gordan coefficient is now 1.

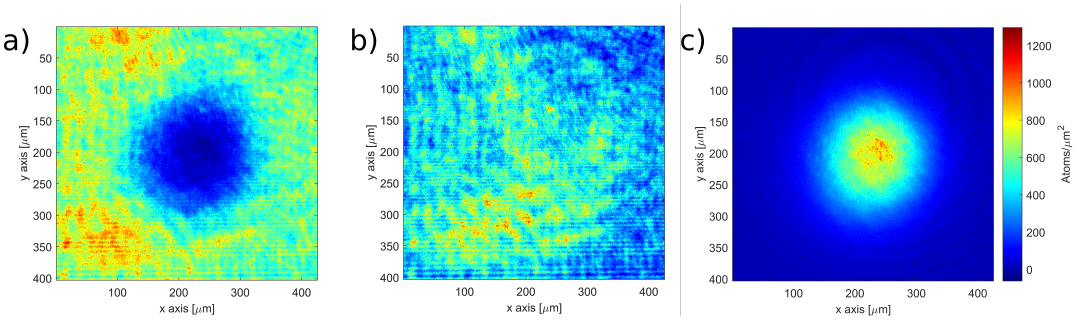

FIGURE 4.2: Raw pictures (a, b) and divided picture (c). Here a) is $I_A(x,y)$ and b) is $I_0(x,y)$. By dividing a) by b), we obtain c). The atom number is calculated there, in a logarithmic scale as per Equation 4.7.

As we have to divide I_A by I_0 (see Equation 4.3), if the atom cloud is too dense we may get no light on the CCD. That will result in a singularity, interpreted by our software as an optical density above 6 and will saturate there. This will lead to an incorrect measurement of the atom number. To avoid it, we image the atoms after a free ballistic expansion of the cloud, achieving a less dense cloud and a more

precise atom number, without any saturation (Figure 4.3). This technique is called time-of-flight (TOF) imaging.

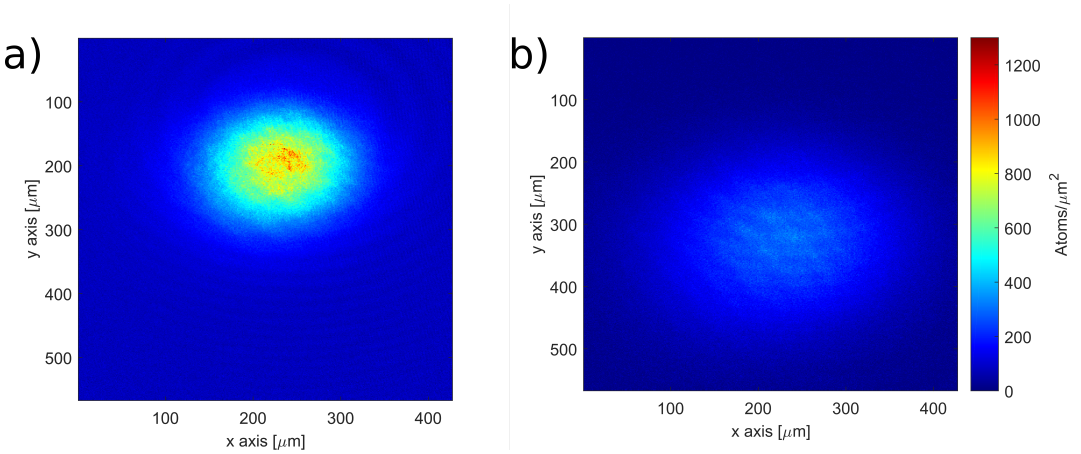

FIGURE 4.3: Atomic cloud after 12 ms of TOF (a) and after 20 ms of TOF (b). The cloud expanded as it fell and by doing so it became less dense. In picture (a), the centre of the atomic cloud is saturated, while in picture (b) it is not. In a saturated region of a picture we cannot determine the number of atoms, as no light reaches the CCD sensor and thus we can only say that there's at least the number of atoms we are currently measuring.

Off-resonant imaging is another technique to determine the atom number for dense clouds. It uses a small detuning ($\sim$ 1.5Γ) of our imaging frequency. Some clouds are too dense to image in our limited range of possible TOF durations. As we cannot extend the duration of the TOF because the atoms escape our field of view, this technique provides a lower value of the optical density, and we need to calibrate the atom number ratio seperately between images with off-resonant and resonant light. For the calibration we use a small cloud of atoms after the MOT, which allows us to measure the optical density with both imaging methods.

Due to the strong scattering of photons and due to the resulting acceleration and heating of the atoms, the imaging process is destructuve.

4.1.2 Measuring temperatures using TOF absorption imaging

For a gas of classical partices, the momentum distribution of the atoms corresponds to a three-dimensional Gaussian distribution (Figure 4.4). The momentum width of the cloud is related to its temperature (T) by the following equation [64]:

$$T = \frac{M}{k_B}\sigma_v^2, \tag{4.8}$$

where M is the atomic mass, k_B the Boltzmann constant and σ_v the velocity distribution, which is the Fourier transform of the spatial distribution of the atomic cloud. As we cannot measure directly σ_v, we obtain it from a fit to r, the Gaussian radius of the cloud after a ballistic expansion.

$$r = \sqrt{r_0^2 + \sigma_v^2 t^2}, \tag{4.9}$$

where r_0 is the Gaussian radius of the thermal cloud at $t = 0$.

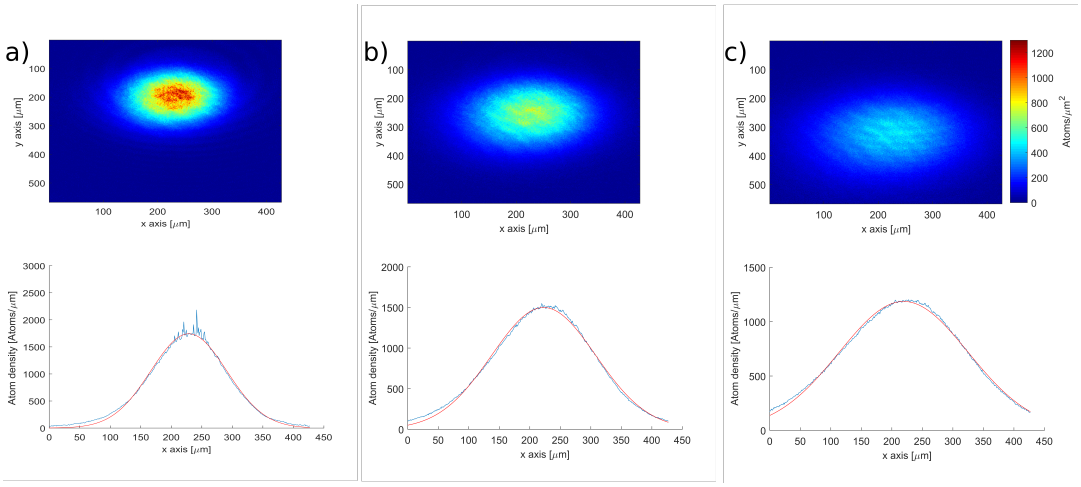

FIGURE 4.4: Time-of-flight thermal expansion of an atomic cloud. We can see how the atomic density profiles expand as the cloud falls from a) to c).

4.2 3D MOT chamber imaging system

In this section we will describe our different imaging systems used in our 3D MOT Chamber. We will also show the differences between the different imaging systems and their characteristics. As our first subsection, we will do an overview of the systems (Section 4.2.1), followed by an analysis of the so-called Long imaging axis and the Dipole imaging axis (Section 4.2.2).

4.2.1 Overview of the imaging setup

The goal of our absorption imaging setups is to obtain the best resolution possible during the imaging of the shadow of the atomic cloud in the vacuum chamber while keeping optical access to the experiment for the rest of our setups. To do so, we use a two-lens imaging system (Figure 4.1) to create a real image of the atomic cloud in the CCD sensor. The resolution is defined as the minimum distance between two distinguishable objects. The resolution of a diffraction limited system is largely defined by the parameters of the first lens [62]:

$$\Delta l \approx 1.22 \frac{f\lambda}{D} \tag{4.10}$$

where Δl is the spatial resolution of the system, f is the focal distance of the first lens, λ is the wavelength of the light and D is the diameter of the lens. As per the Rayleigh criterion (Equation 4.10), two points are distinguishable if the first diffraction minimum of one point and the diffraction maximum of the other coincide. This is defined as the diffraction limited scenario in an imaging system.

The ratio between the first and second lens determines the magnification of the system. As we want the full atomic cloud and the surrounding area to be visible, we demagnify the object [1] to be smaller than the CCD sensor, which has an area of 3.84 mm $\times$ 2.88 mm in our MatrixVision BlueFox3 camera.

The magnification, M, is calculated as follows:

$$M = -\frac{f_2}{f_1}, \tag{4.11}$$

with f_1 the focal distance of the first lens and f_2 the focal distance of the second lens.

4.2.2 Imaging axes

We image along two axes in the horizontal plane of our setup. Both imaging paths use a similar $4f$ configuration of lenses. The Long imaging axis cuts across the full length of the vacuum chamber, entering through the Science Chamber and exiting through the 3D MOT Chamber (Figure 4.5). Our vacuum chamber, as our optical table, is longer in this axis direction, hence naming this axis as "Long".

[1] The imaging beam and part of the chamber. They are approximately 2 cm in size.

The Long axis imaging system consists on two 2-inch lenses to provide a good compromise between a high resolution of the imaging system and a low restriction of the optical access to the chamber. The smallest of all the optical elements in the imaging path determines the aperture of the full system. We also ensure that no vignetting happens on our images, and the aperture of the system is kept constant.

The focal lengths of the two lenses are of 200 mm and 75 mm, respectively (Figure 4.5). As per equations (4.10, 4.11), the angular resolution, Δl is 3.75 µm and the magnification M is -0.375. As our MOT cloud is larger than the size of our sensor, we have to de-magnify our image in order to capture the cloud and so we can observe some time-of-flight expansion. The negative magnification indicates that the image on the CCD sensor is inverted respective to the original object, i.e. the atomic cloud. Our software takes corrects the orientation by rotating the images.

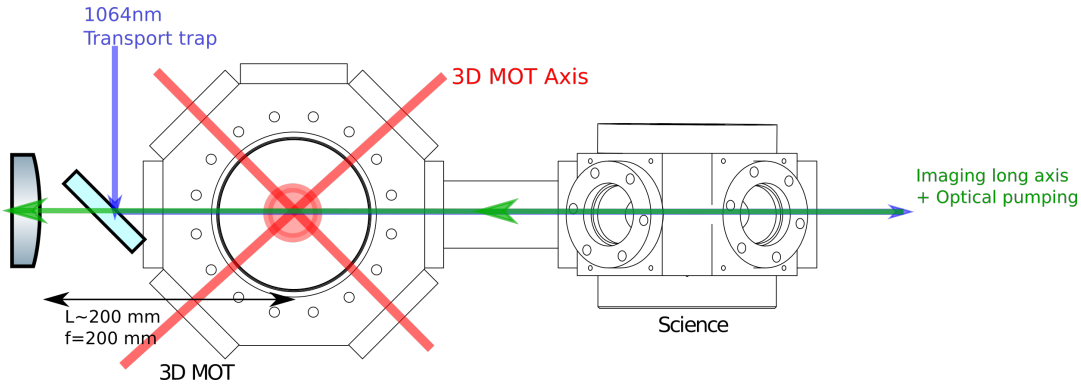

FIGURE 4.5: Diagram of the Long imaging axis. The Optical Dipole Trap (ODT) beam of the "transport trap" shares part of the path with the imaging axis.

Our second imaging paths shares the direction of propagation with our crossed optical dipole trap (Dipole axis, Figure 4.6). Due to the overlap with the 3D MOT cooling beams (Figure 4.6), the focal length ($f_1 = 300$ mm) of the initial imaging lens on the Dipole axis is larger than on the long axis. We use a polarising beam splitter (PBS) to separate the imaging beam from the MOT beam. The PBS limits the aperture of our imaging system to 1 inch diameter. Similar to the Long axis imaging system, the first lens has a diameter of 2 inches. However, as the resolution of the system is already limited by the PBS, the second lens has a diameter of 1 inch. The focal length of the second lens is $f_2 = 200$ mm, resulting in a total resolution of $\Delta l \sim 5.6$ µm and a magnification of -0.67 for the Dipole imaging axis.

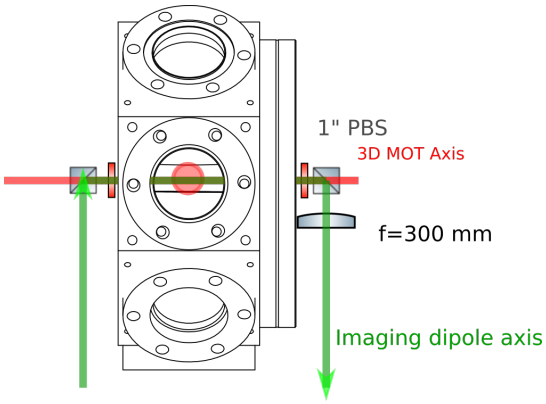

FIGURE 4.6: Top view diagram of the imaging along the Dipole axis of the 3D MOT chamber.

4.3 Magneto optical traps

In this section, we provide an overview of our magneto optical traps, which capture and precool the atoms from room temperature down to a few μK. We start with a 2D MOT in the high-vacuum section of the experiment and continue the discussion with the 3D MOT section (Section 4.3.1), a compression phase (Section 4.3.2), and a measurement of the temperatures (Section 4.3.3).

4.3.1 Cooling in the 2D MOT and 3D MOT

The goal of a 2D-MOT section is to provide a high flux of transversally cooled atoms (Section 3.1.1). The rubidium atoms diffuse from the oven section at approximately 40 °C to the high-vacuum section with the 2D MOT, where the pressure is a compromise between having a high enough flux of atoms and flooding the glass cell with rubidium atoms. We found best loading rates for a pressure of 1.5×10^{-7} mbar.

To generate a large flux with the 2D-MOT setup, we use large laser beam diameters with a large trap volume and a high laser power of 500 mW, distributed over the four different beams of the 2D MOT. We enlarge the 2D MOT cooling beams from the optical fibres by using a caged telescope system based on the original design by Di Carli [65]. Once the beams have a 25.4 mm beam waist, we divert a fraction of their power into the glass cell by changing the polarisation plane of the beams with a $\lambda/2$ waveplate and a polarising beam splitter (PBS), while the rest of the power continues through. The configuration is repeated two more times, resulting in three parallel beams with retro-reflection. In order to compensate for the gravitational effect, the power is highest in the lowest of the three beams. The combination of our beam configuration and the magnetic fields generated by our shim and gradient coils (Section 3.3.1) produces an ellipsoid shaped trap. To enhance density and the subsequent flow of atoms towards the ultra high vacuum section we add an extra cooling beam on the vertical axis, which generates an optical molasses on that axis (2D MOT + [66]).

As discussed in Section 3.4, the 3D MOT and 2D MOT both use cooling and repumping transitions. The $|F = 2\rangle$ to $|F' = 3\rangle$ is the transition used to cool the atoms and, in order to keep a closed cycle, we also have a repumping laser on the $|F = 1\rangle$ to $|F' = 2\rangle$ transition to pump back up to $|F = 2\rangle$ any atoms that decay to $|F = 1\rangle$ (Figure 3.6).

The 2D MOT traps and cools a fraction of the rubidium vapour that fills the glass cell (2D MOT, Section 2.2.3) in a few miliseconds from above room temperature to mK.

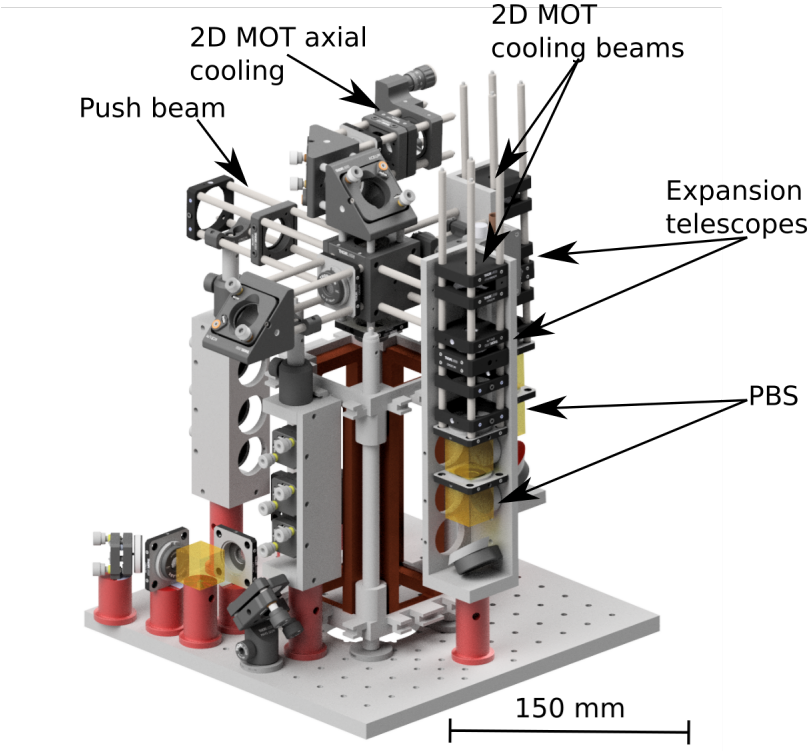

FIGURE 4.7: Three-dimensional computer assisted design (CAD) drawing of the optics and opto-mechanics of our 2D MOT setup. On the top we overlap the resonant push beam with the 2D MOT axial cooling. On the sides we expand the two 2D MOT cooling beams with expansion telescopes and divert their power into the glass cell sequentially, by controlling the polarisation of the beams with the $\lambda/2$ waveplates situated before the polarising beam splitters (PBS).

Transversally cooled atoms are continously pushed down through the differential pumping tube that connects the high vacuum and the ultra high vacuum section by a resonant laser beam. The push due to a resonant absorption and reemission of photons assists the acceleration due to gravity, resulting in a downwards flow of the atoms through the differential pumping tube.

After being pushed down from the high vacuum section into the ultra high vacuum section, the atoms are then recaptured in our three-dimensional magneto optical trap (3D MOT). We keep the 2D MOT and the push beam on while we load the 3D MOT for a typical duration of 1500 ms.

We optimized our 3D MOT parameters to achieve a maximum atom number after loading for 1.5 s. We have found the optimal values for a detuning close to 1 Γ on our 2D and 3D cooling frequencies and currents of 2 A and 5.5 A in our 2D and 3D gradient coils. The current on the 3D MOT gradient coils correspond to a gradient field of 13 G/cm. The shim coil values are set to compensate the Earth's magnetic field and the residual field from the rest of the nearby magnetic equipment, such as optical isolators. In order to cool the atoms by grey molasses (Section 4.4.3) we require magnetic fields as close to the null values as possible. The shim coils are also used to displace the centre of the MOT in the chamber to maximise the number of atoms loaded into the crossed optical dipole trap (CODT). We load 3×10^9 atoms in 1.5 s.

4.3.2 Compressed MOT

We have shown already that we can trap a large number of atoms in our 3D MOT, but as our goal is to trap as many atoms as possible in the crossed optical dipole trap (CODT) in order to have a large reservoir of atoms to evaporate into a Bose-Einstein condensate (Section 5.1), we require a high spatial density of atoms. By compressing the 3D MOT to a fraction of its original volume and applying an off-resonant cooling process we increase its spatial density greatly (Figure 4.8).

To increase the phase-space density (PSD) of the atomic cloud, we increase the 3D MOT gradient coils current and detune the cooling laser in order to create a compressed MOT (CMOT) configuration [67]. During the compressed MOT phase we increase the current in the 3D MOT gradient coils from 5.5 A to 20 A, thus increasing the gradient field from 13 G/cm to 41 G/cm. While we ramp up the current, we also detune the 3D MOT cooling laser to 140 MHz ($\sim 23\Gamma$) red detuned from the $|F = 2\rangle$ to $|F' = 3\rangle$ transition. This frequency is close to being halfway between the $|F = 2\rangle$ to $|F' = 3\rangle$ and the $|F = 2\rangle$ to $|F' = 2\rangle$ transitions. The large detuning from the $|F = 2\rangle$ to $|F' = 3\rangle$ transition enables us to cool the atoms to lower temperatures when applied to a denser cloud, like the one after compression [67].

Figure 4.8 shows absorption images of the 3D MOT with and without compression. Due to the large flux of our 2D MOT, we had to strongly reduce the MOT loading time to avoid a complete absorption of the imaging beam (Section 4.1.1). The pressure in the 2D MOT chamber was 2×10^{-7} mbar while the 3D MOT loading time was 50 ms. The number of atoms is the same in both pictures, it being 6×10^7 atoms.

Our CODT has a small volume, compared to the MOT. Increasing the density of the MOT allows us to trap more atoms in the same CODT trap volume.

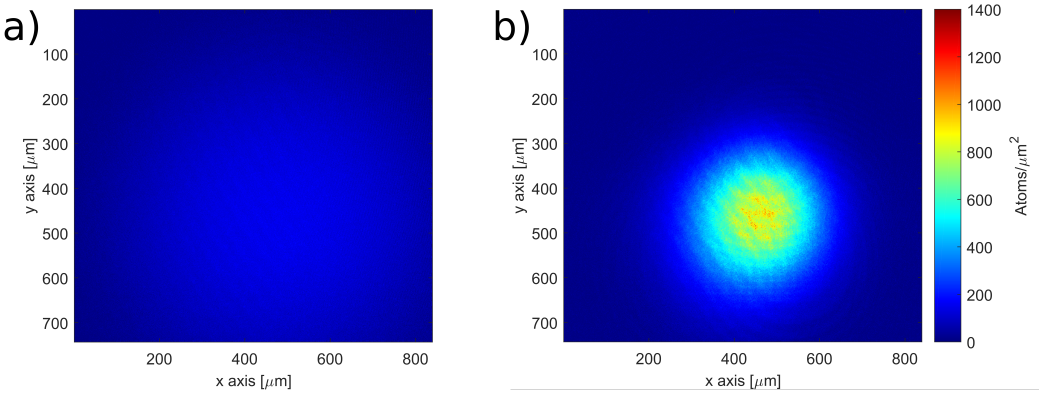

FIGURE 4.8: Uncompressed (a) versus compressed (b) MOT. The compressed MOT is running for 18 ms, and the current in the gradient coils went from 5 A to 20 A, generating a gradient field that went from 13 G/cm to 40 G/cm. The density is much higher in (b), as the same number of atoms fills a lesser volume. The increased density enhances the loading into the CODT.

4.3.3 Measurement of MOT temperatures

For the measurement of the temperature in our MOT, we use time-of-flight (TOF) expansion and absorption imaging as discussed in Section 4.1.2. Figure 4.9 shows the Gaussian width of the atomic cloud over a TOF expansion period of 12 ms to 20 ms. The period is chosen to avoid saturation for short TOF and expansion beyond the imaging region for long TOF. We use Equation 4.8 to extract the temperature from the expansion velocity by fitting Equation 4.8 to the Gaussian width expansion and extracting σ_v.

We determine typical temperatures of 500 µK for the 3D MOT and 40 µK with compression for a cloud of atoms of 3×10^9 atoms.

As discussed in Section 4.3.2 the low temperature of the compression phase is caused by detuning the cooling beam between the $|F = 2\rangle$ to $|F' = 3\rangle$ and the $|F = 2\rangle$ to $|F' = 2\rangle$ transitions. Cooling at that frequency results in less heating by reabsorption and reemission of photons.

To recapitulate, in just a few milliseconds, a MOT can cool down atoms from room temperature to sub-Doppler cooling temperatures. In the case of our 3D MOT, we typically we cool a cloud of 1×10^9 atoms to 500 µK (Figure 4.9).

During the compressed MOT phase, we detune our cooling laser to achieve a molasses-like effect (Section 2.2.1), the temperature in our CMOT is much lower than in the 3D MOT. The temperature of our atoms after the compressed MOT is usually close to 40 µK for 1×10^9 atoms.

Atomic density is a factor that becomes important when cooling down the atoms in a magneto optical trap, especially when the atom numbers and densities involved are large. In the case of molasses cooling, due to the large detuning from either transition involved and the low repumper powers used, density barely affects the quality of the cooling as there is less heating by reabsorption and reemision of photons.

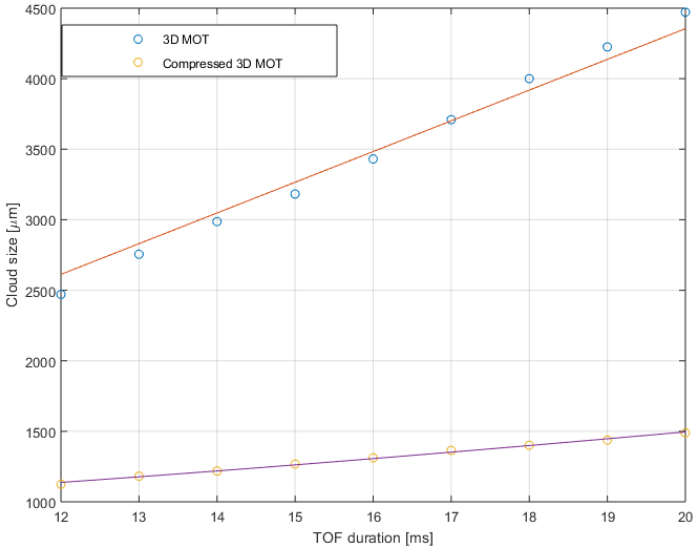

FIGURE 4.9: Time-of-flight measurement to compare cloud sizes of the uncompressed and compressed 3D MOT. The larger detuning on the compressed MOT improves the cooling of the atoms, achieving smaller cloud size and thus lower temperatures than in the regular MOT. The temperature of the uncompressed 3D MOT is 495(9) µK, while the temperature of the compressed 3D MOT is 38(1) µK.

4.4 Achieving lower temperatures with molasses cooling

If we try to load the atoms in the Crossed Optical Dipole Trap (CODT) without cooling them below the CMOT temperatures of 40 µK we only load 5×10^5 atoms. By applying red molasses and then grey molasses we lower the temperature of the cloud to approximately 4 µK and we achieve a loading in the CODT of 8×10^7 atoms.

In this section we will begin with a description on how we achieve molasses cooling, first by achieving a null magnetic field (Section 4.4.1), moving on to red molasses (Section 4.4.2) and then grey molasses (Section 4.4.3).

After describing our grey molasses process, we will show the different cooling regimes that we observe if we skip the red molasses stage and just cool using grey molasses (Section 4.4.4). It will be followed by a description of the 2-photon process nature of the Λ-enhanced grey molasses (Section 4.4.5). After that, we will explain how applying grey molasses after red molasses yields a colder sample (Section 4.4.6). We will conclude with the effect of grey molasses on the loading of the atoms in the CODT (Section 4.4.7).

4.4.1 Working on a compensated magnetic field

To maximise the efficiency of both red and grey molasses cooling processes, we require our atomic cloud to be in a zero magnetic field. There are two mechanisms that allow us to achieve this state. One is the vanishing of eddy currents in the coils, specially the gradient coils. The gradient coils are the ones where we employ much

higher currents than the currents used in the shim coils[2]. The second being the compensation of the residual magnetic fields at the position of the atoms by using the shim coils.

The 3D MOT gradient coils require 30 ms for the residual field produced by the eddy currents to decay (Figure 4.10).

In the presence of a magnetic field, the m_F states split from each other, making them non-degenerate states. This phenomenon is called Zeeman splitting [68]. We can then probe the atoms with a microwave (MW) transition, on the $|F = 2\rangle$ to $|F = 1\rangle$ transition and directly image them employing Repumper light on the $|F = 1\rangle$ to $|F' = 2\rangle$ transition. As the Zeeman splitting for the m_F states of the $|F = 2\rangle$ hyperfine state of ^{87}Rb roughly corresponds to 0.7 kHz/mG, by scanning the MW frequency to probe the position of one the peaks for different waiting times after the compressed MOT stage, we are able to determine the residual magnetic field when the peak stops moving (Figure 4.10) and how long it takes for the eddy currents to vanish.

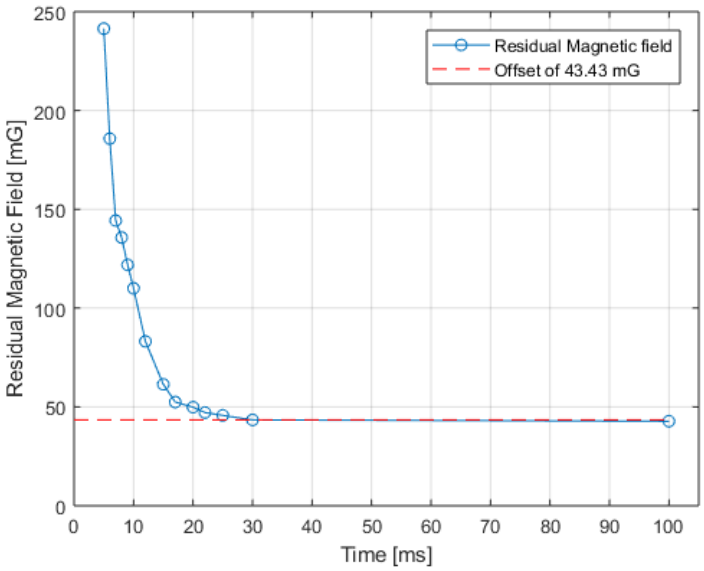

FIGURE 4.10: Measurement of the decay time of the eddy currents after the compressed MOT. Each data point corresponds to the displacement of the $|F = 2; mF = -2\rangle \rightarrow |F = 1; mF = -1\rangle$ peak on a MW spectrum after different waiting times for the eddy currents.

To compensate the residual magnetic field at the position of the atoms, we scan the positions of the MW peaks on the $|F = 2; m_F = -1\rangle$ to $|F = 1; m_F = 0\rangle$ and $|F = 2; m_F = 0\rangle$ to $|F = 1; m_F = -1\rangle$ transitions while varying a shim coils current in one of the three axes, the Transport, Dipole and Vertical axes. We then plot the positions of the peaks versus the current in each of the axes and fit a parabola to them, to obtain the value where the magnetic field is compensated (Figures 4.11, 4.12). We fit a parabola due to the quadratic nature of the Zeeman shift. When all the three

[2]In the gradient coils we use currents of 5 A for more than a second and 20 A for 18 ms, as opposed to the less than 1 A currents of the shim coils.

axis are compensated, the peaks overlap. In this situation we reduce the step and the power of the MW scan, to avoid power broadening [69] and refine our scan. In the end, we are limited by our inability to resolve the peaks, as they overlap into a single one. Its width is in the order of 10 kHz and so our residual field is close to 7 mG.

Another way of achieving better compensation values is to use an offset in one of the axes, thus avoiding the overlap of the peaks in a single one. This process is repeated for the remaining two axes, so as to compensate the three axes.

The aforementioned magnetic field compensation process works best when the size of the atomic cloud is as small as possible. The measurements above are from atoms loaded in the CODT from a 3D MOT loaded for 25 ms. The smaller our cloud, the more sensitive it will be to an imbalance of the magnetic fields.

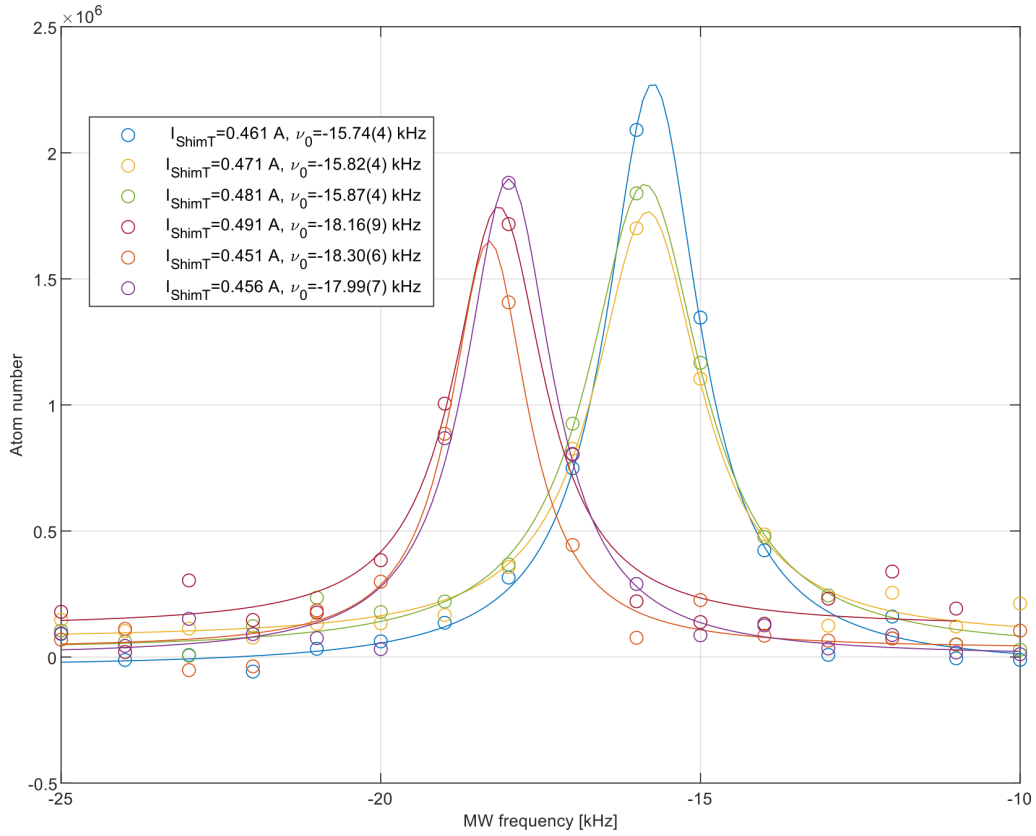

FIGURE 4.11: Displacement of the MW peak of the $|F = 2; m_F = -1\rangle$ to $|F = 1; m_F = 0\rangle$ and $|F = 2; m_F = 0\rangle$ to $|F = 1; m_F = -1\rangle$ transition for different values of the transport shim coil current.

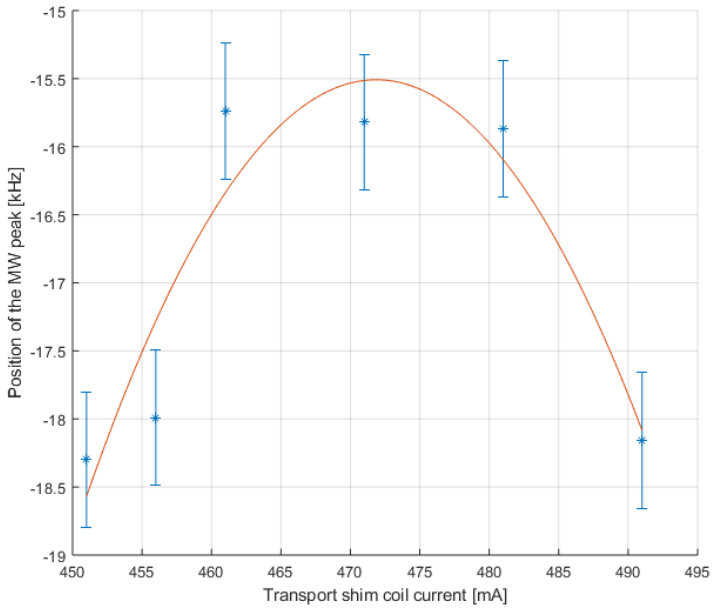

FIGURE 4.12: Finding the null field current value of −470 mA by fitting a parabola to the different MW peak positions of the different Transport shim coil currents.

4.4.2 Initial red molasses cooling

In order to achieve red molasses cooling (Section 2.2.1) after our compressed MOT stage, we turn our cooling and repumping lasers acousto-optical modulators (AOM) off in 0.1 ms and lower their powers. We also bring the shim coils to the null values.

During the next 5 ms, while we keep the AOMs off, we detune the Cooling Laser to close to 40 MHz blue detuned from the $|F = 2\rangle$ to $|F' = 2\rangle$ transition. This is done to avoid heating the atoms while detuning the lasers, even at the cost of having the atoms in free space for 5 ms. After the detuning of the lasers, we turn the lasers back on and cool the atoms by red molasses for 18 ms.

After the red molasses our atoms are usually cooled down to close to 9 µK (Figure 4.14). While this is a much lower temperature than the one for a MOT[3] or a compressed MOT[4], we can cool the atoms further down by adding an extra grey molasses stage after the red molasses.

4.4.3 Further cooling using grey molasses

After the red molasses, in the next 2 ms of our experimental sequence, we proceed by changing the detuning of the 3D MOT Cooling beam slightly from our red molasses stage, from 40 MHz to 35 MHz blue detuned on the $|F = 2\rangle$ to $|F' = 2\rangle$ transition

[3] Usually in the order of 500 µK.
[4] Approximately 40 µK.

and by shutting off the repumping laser as it will not be required in this stage. During the subsequent 5 ms we use the cooling 3D MOT beam and its EOM generated sidebands to cool down our atoms by grey molasses.

Our grey molasses rely on the fact that both cooling and repumping beams are coherent [13] to preserve the linear superposition of the $|F = 2\rangle$ and $|F = 1\rangle$ sublevels. The superposition of these levels will act as the dark states in our cooling scheme (Section 2.2.2).

To ensure the coherence of cooling and repumper beams, we use an Electro Optical Modulator (EOM) to generate sidebands on our cooling beam before amplifying it in the 3D MOT tapered amplifier (Section 3.4.4). We feed a 6.834 GHz signal to the EOM and use the $|F = 2\rangle$ to $|F' = 2\rangle$ transition beam as the carrier so as to generate the sidebands with a detuning equal to the hyperfine splitting between the $|F = 2\rangle$ and $|F = 1\rangle$ sublevels.

By controlling the power of the 6.834 GHz signal, we can vary the ratio between carrier and sidebands and that is equivalent to varying the ratio between cooling and repumping beams. By optimising the ratio between cooling and repumping beams we achieve temperatures as low as 3.3 µK.

As we can observe in Figure 4.13, the PSD of the atomic cloud after grey molasses is noticeably higher than after the compressed MOT. The typical temperatures of a fully loaded 3D MOT after grey molasses are in the order of 4 µK (Figure 4.14).

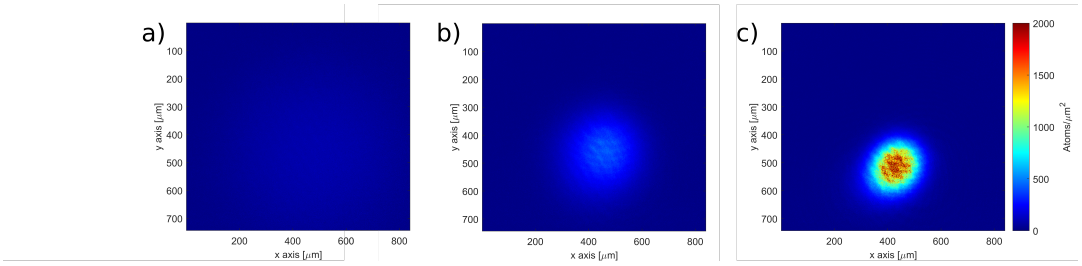

FIGURE 4.13: Uncompressed (a) vs compressed MOT (b) vs grey molasses (c). The three pictures were taken in the same conditions and, so as to avoid saturation on the grey molasses, the 3D MOT was only loaded for 25 ms. The atom number in the three pictures is 2.81×10^7 atoms. The density of the cloud after grey molasses is even higher than after the compressed MOT.

4.4.4 Grey molasses cooling regimes

The effectiveness of our grey molasses is improved by having a previous red, or bright, molasses phase. The red molasses phase cools the atoms to temperatures low enough so the grey molasses becomes most effective by relying on the dark states achieved by the slow-moving atoms (Section 2.2.2) [13].

If we do not achieve these lower temperatures beforehand and instead we apply the grey molasses to cool the atomic cloud after the compressed MOT at a temperature around 40 µK, we observe the following by scanning the duration of our grey molasses stage (Figure 4.15).

During the initial 5 ms there is a sharp decrease on the cloud size, followed by a stabilisation. The whole process lasts about 5 ms. After that stage, we observe cooling similar to the grey molasses cooling after an initial red molasses stage. This cooling stage lasts from 5 ms to approximately 20 ms where the cloud reaches the typical cloud size after grey molasses and remains at a constant cloud size (Figure 4.15).

The temperature after the initial stage corresponds roughly to the temperature after red molasses, while the second stage brings us to the temperatures slightly higher than the ones achieved after red and grey molasses (Sections 4.4.3,4.4.6,Figure 4.14). The dark states of the grey molasses are only achievable by slow moving atoms. Unless we precool the atoms using red molasses, our atoms are going to be too hot to reach the dark states and thus will not benefit from the grey molasses.

4.4.5 Λ-enhanced grey molasses as a two-photon process

The grey molasses cooling scheme relies on a Λ 2-photon Raman scheme to create coherent, velocity selective dark states. We scan the relative detuning between the repumper and the cooling beams. To do so, we finely scan the transition frequency. As it is a frequency in the MW regime, we use a MW frequency (Section 3.2) that we feed into the electro-optical modulator (EOM, Section 3.4.4) to generate sidebands on the cooling frequency. The sidebands and the carrier are detuned by the same frequency as the $F = 2$ to $F = 1$ transition. By shining the carrier and the sidebands to the atomic cloud, we excite the atoms in a two-photon transition. When scanning the relative detuning between carrier and sideband we measure a Fano-like [70] resonance profile (Figure 4.16).

We have decided to use a relative detuning of 50 kHz to minimise cloud size and thus cloud temperature.

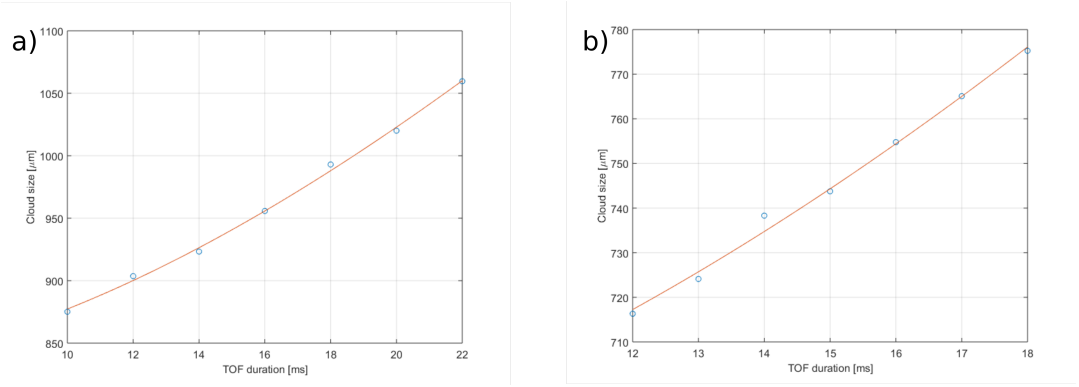

FIGURE 4.14: Temperature measurement after red molasses (a). The temperature is 9.6 µK, about four times lower than the compressed MOT temperature (38 µK, Figure 4.9). Temperature of the atomic cloud after red and grey molasses (b), $T_{\mathrm{GMol}} = 3.3(4)$ µK. The full cloud consisted of more than 1×10^9 atoms. The duration of the red and grey molasses were 18 ms and 5 ms, respectively.

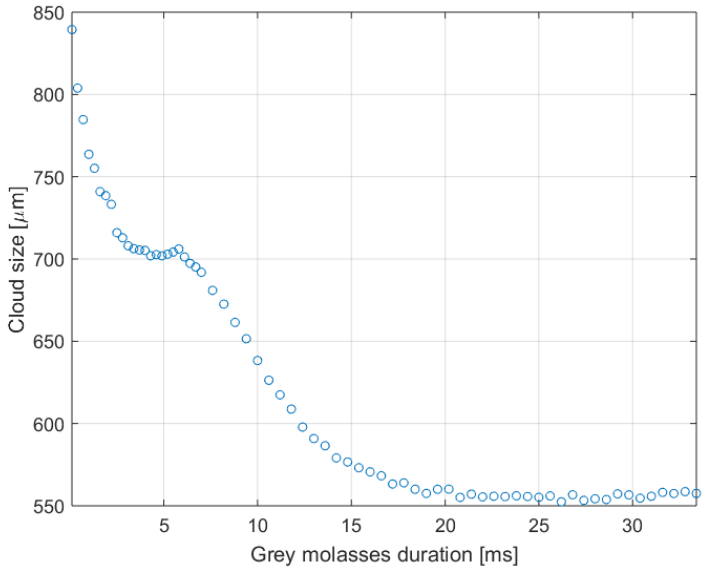

FIGURE 4.15: Scan of the duration of the grey molasses cooling phase, with no prior red molasses. As we increase the duration of the grey molasses, we can observe different cooling regimes. Up to 5 ms the atoms are cooled by standard bright (red) molasses. From 5 ms up to 20 ms the atoms are cooled further down by the Λ-enhanced grey molasses process. In all of these pictures we employed a TOF of 20 ms.

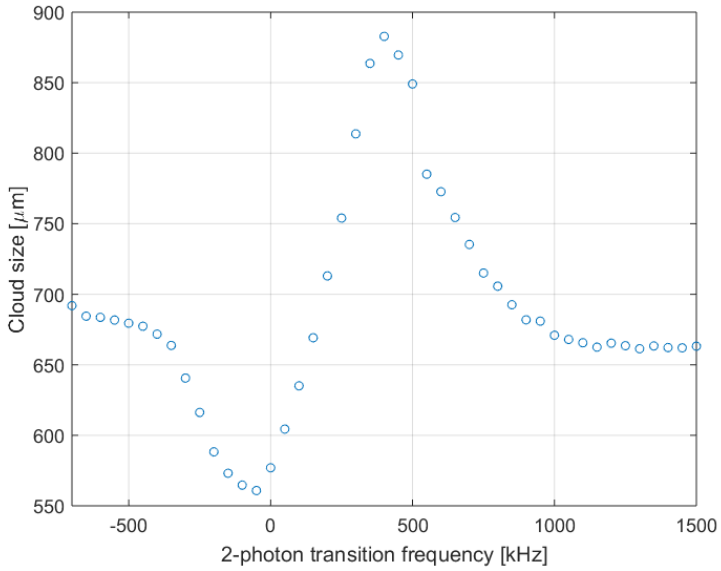

FIGURE 4.16: Scan of the 2-photon transition frequency during grey molasses cooling. As we scan through the frequency of the repumping beam produced by the EOM, we observe the characteristic Fano-like profile of the 2-photon transition.

4.4.6 Improvement on the grey molasses cooling after red molasses

In a previous section (Section 4.4.4) we have confirmed that the grey molasses becomes more effective after a red molasses regime by showing that the initial cooling of the atoms brought us to similar temperatures as the red molasses and only then we could access lower temperatures.

Nevertheless, by adding a grey molasses stage after the initial red molasses we achieve even lower cloud sizes (temperatures). To summarise, in a normal experimental run, after compressing the MOT, we apply red molasses cooling and then grey molasses cooling to the atomic cloud.

4.4.7 Grey molasses effect on the loading of the Crossed Optical Dipole Trap

The cooling of the MOT cloud by the grey molasses plays a big role on the amount of atoms we are able to load into the crossed optical dipole trap (CODT).

The depth of a dipole trap can be expressed in temperature units (Section 2.2.4) and so with our current CODT parameters[5] we find that $U_{CODT} = 85\,\mu K$. Due to the velocity distribution of our atoms, only atoms with a temperature below 10% of the trap depth will remain trapped. The colder our atomic cloud, the larger a fraction of the atoms we will be able to trap.

In Figure 4.17 we observe how the atoms remain trapped in the CODT if we cool them down with the grey molasses, while if we just load the CODT after compressing the 3D MOT the trapped fraction decreases quite rapidly.

4.5 Conclusions

In this chapter we have demonstrated how we image our atoms (Section 4.1) and how we can measure both the atom number (Section 4.1.1) and the temperature (Section 4.1.2) of the clouds.

We have also showed how we can trap (Section 4.3.1), compress (Section 4.3.2) and cool (Section 4.4) the atomic cloud before loading it into the crossed optical dipole trap (CODT). Our 3D MOT can load above 3×10^9 atoms in less than 1500 ms. After compression (Section 4.3.2), we cool and trap the same amount of atoms in a much tighter volume, achieving higher phase-space density (PSD). After a 18 ms compression phase we achieve temperatures close to 40 µK, approximately an order of magnitude lower than the MOT temperatures (Section 4.3.3).

By adding a red molasses phase (Section 4.4.2) before a Λ-enhanced grey molasses we are able to cool our extremely dense cloud to 3.3 µK, slightly lower temperatures than [13] for an additional order of magnitude of atoms cooled.

[5] Intensity of the laser beams equal to $I_{CODT} = 2 \times 100\,W$ and waist equal to $w_0 = 300\,\mu m$

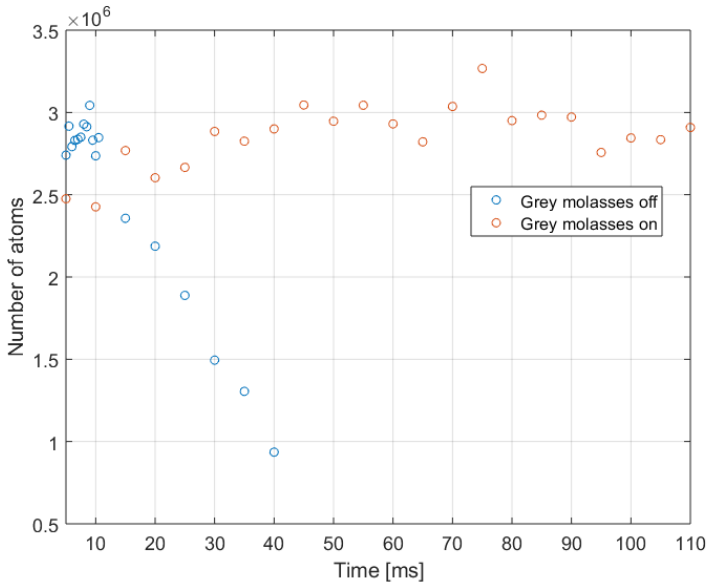

FIGURE 4.17: Atoms trapped in the CODT, with and without having been cooled by the grey molasses. Without grey molasses the atoms are too hot to be kept in the trap and they escape from it. The low atom numbers displayed in this figure are due a short MOT loading time of 25 ms.

Achieving these densities and temperatures enables us to load about 8×10^7 atoms in our CODT, which is a nice starting point for our evaporation sequences in order to achieve a larger than 2×10^6 atoms all-optical Bose-Einstein condensate.

Chapter 5

Creation of an all-optical ^{87}Rb BEC

In this chapter, we will describe our route to the creation of an all-optical BEC of ^{87}Rb atoms. We load into the crossed optical dipole trap (CODT) and evaporate an atomic cloud of 8×10^8 atoms at a temperature of 3 µK to an approximately 2×10^6 atoms Bose-Einstein condensate (BEC).
We will begin by explaining step by step our experimental sequence (Section 5.1): Loading the atoms in the crossed optical dipole trap (CODT, Section 5.1.1), optically pumping the atoms to the desired $|F = 1; m_F = -1\rangle$ state (Section 5.1.2) and evaporating the atoms from the combined Transport trap and CODT (Section 5.1.3). By doing an all-optical evaporative cooling we are able to achieve condensation faster than with the common technique of evaporative cooling in magnetic traps.
We will continue the chapter by characterising the final BEC (Section 5.2). We will discuss how the different characteristics of the ultracold cloud evolve in each of the evaporation stages and possible ways of how to improve the current BEC. We will start by analising the atom number (Section 5.2.1), then the temperature (Section 5.2.2), followed by the trap frequencies (Section A.0.1), the phase-space density (PSD, Section 5.2.3) and conclude by analising the timescale and duration of the evaporation ramps .
At the end of the chapter, we will extract some conclusions and offer some remarks (Section 5.3). There is room for improvement on the evaporation sequence, as once we achieved a large BEC we decided to build the next stages of the experiment.

5.1 Experimental sequence

In this section, we will detail the experimental sequence used to create a BEC. As the initial cooling of the atoms was already covered in Chapter 4, we will begin with the step immeadiately after the grey molasses cooling (Section 4.4), i.e. with the loading of the atoms into the crossed optical dipole trap (CODT).

To create a Bose-Einstein condensate, we need to cool down the atoms below the Doppler temperature, T_{Doppler} (Section 2.2.1). To do so, we load the atoms from the grey molasses cooled cloud into the CODT (Section 5.1.1). Once we have trapped the atoms in the CODT, we bring them to the $|F = 1; m_F = -1\rangle$ state, using optical

pumping (OP) and rapid adiabatic transfer using a microwave (MW) transition (Section 5.1.2). The next step is increasing the phase-space density (PSD) of the atoms, by cooling them with evaporative cooling (Section 5.1.3).

5.1.1 Loading into the Crossed Optical Dipole Trap

Once the atoms have been compressed to a very tight volume and typically cooled down to temperatures close to 4 µK, using the Λ-enhanced grey molasses, we load them into our CODT (Figure 5.1) by ramping up the lasers up to 60% of their maximum output power (Figure 5.2), (120 W per beam). The typical atom number that we trap is close to 8×10^8 atoms. The temperature of the atoms increases during the loading process because of an insufficient matching of the density profiles before and after loading into the CODT. After a short waiting time of 200 ms, the atoms have re-thermalised to a $1/10^{\text{th}}$ of the trap depth, with a temperature of 16 µK.

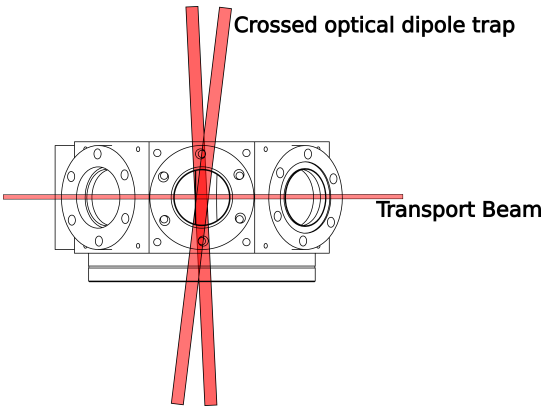

FIGURE 5.1: Diagram of the beam configuration of the crossed optical dipole trap plus the transport beam, acting as a dimple, in the MOT chamber.

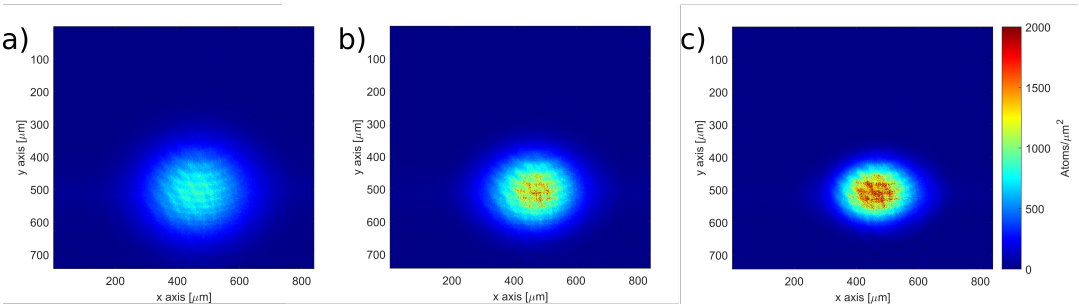

FIGURE 5.2: Atoms loaded into the CODT, depending on the trap depth of the CODT. In a) we use 100% of the avalaible power, in b) we use 70% and in c) 50%. As all the pictures are taken with the same TOF of 20 ms, we observe that atoms in c) expand less and are therefore colder. This may be due to having a shallower or wider trap, or most likely both.

5.1.2 Optical pumping in the CODT and state preparation

To avoid loss we pump the atoms to a particlar energy state. In the case of ^{87}Rb, it is beneficial for us to use the $|F = 1; m_F = -1\rangle$ energy state [44]. To avoid hyperfine-state changing collisions and heating, we use only the $F = 1$ hyperfine state. In addition, to avoid losses between atoms in different Zeeman states, we polarise the atoms to a stretched state, such as the $|F = 1; m_F = -1\rangle$. As we employ optical beams to pump the atoms to the target state, this process is called optical pumping (OP) [71].

In our sequence we use a 15 ms optical pumping pulse on the $F = 2 \rightarrow F' = 3$ transition and a repumping pulse in the $F = 1 \rightarrow F' = 2$ transition, which continues for 3 ms after the optical pumping pulse is shuttered off, in order to bring the atoms to the $|F = 2; m_F = -2\rangle$ state. That state is a dark state for the transitions we use and by using it we minimise the number of absorbed photons in order to pump the atoms. Once the atoms are in the $|F = 2; m_F = -2\rangle$ state, we employ a microwave (MW) transition to transfer the atoms to the $|F = 1; m_F = -1\rangle$ state by rapid adiabatic transfer [72] (Figure 5.4). Rapid adiabatic transfer consists in a near perfect population transfer to the target m_F state by chirping the frequency of the MW pulse. Our rapid adiabatic transfer pulse is a tanh pulse in the frequency spectrum and a square pulse in amplitude. The tanh function maximises the atom transfer [72].

To achieve a $\sigma_\pm$ polarisation, we require that the magnetic field direction is collinear with the optical pumping axis. In our experiment we define the Long axis as the quantisation axis and we null the field in the Dipole and Vertical axis. In a similar manner as with molasses cooling (Section 4.4), we need to wait until the eddy currents have totally subsided to proceed with the optical pumping. After 200 ms, the eddy currents have completely vanished, and we begin the optical pumping procedure.

Our optical pumping laser is tuned to the $F = 2 \rightarrow F' = 3$ transition and sent along the quantisation axis (Figure 4.5) to pump our atoms to the $|F = 2; m_F = -2\rangle$ state. As the atoms absorb σ_- polarised photons, they get excited towards the stretched $|F' = 2; m_F = -2\rangle$ state and decay back to $F = 2$ but to a lower m_F state. If they decay to $F = 1$, a weak repumper on a σ_- pumps them back to $F = 2$. After a few cycles, they reach the stretched state, $|F = 2; m_F = -2\rangle$, as we can see in Figure 5.3. After this, we apply a microwave (MW) pulse to transfer the atoms to the $|F = 1; m_F = -1\rangle$ state, using the rapid adiabatic transfer technique. The frequency of the microwave is $\nu_{MW} = 6.834\,682$ GHz. In Figure 5.4 we show that above 90% of our atoms are in the $|F = 1; m_F = -1\rangle$ state. It is in the $|F = 1; m_F = -1\rangle$ state where we will prepare our BEC. The remaining atoms in $|F = 2; m_F = -2\rangle$ are removed by a resonant pulse on the $F = 2 \rightarrow F' = 3$ transition. For imaging we require a brief repumper pulse in order to bring the atoms to the $|F = 2; m_F = -2\rangle$ from the $|F = 1; m_F = -1\rangle$ state.

The total transfer efficiency for the optcal pumping process and the rapid adiabatic transfer is above 90% and the temperature of the atoms rises to 35 µK due to

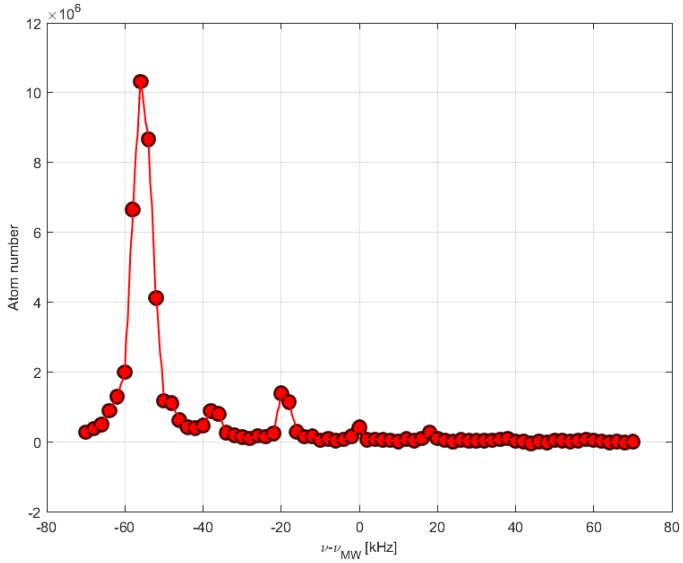

FIGURE 5.3: MW peaks after the optical pumping pulse. We use the σ_+ $F = 2$ to $F = 1$ transition ($\nu_{MW} = 6.834\,\text{GHz}$). For this measurement we employed a magnetic field offset of $B_{off} = 14\,\text{mG}$. The only peaks that we observe are primarily the $|F = 2; m_F = -2\rangle$ to $|F = 1; m_F = -1\rangle$ transition and, with much less intensity the $|F = 2; m_F = -1\rangle$ to $|F = 1; m_F = 0\rangle$ transition peak.

the heating by absorption and reemission of photons and atoms rethermalising at the bottom of the trap.

5.1.3 Increasing phase-space density: Evaporative cooling in a dipole trap

In this stage, all the remaining atoms are in the $|F = 1; m_F = -1\rangle$ state, where we will reduce the depth of the dipole traps to cool the atoms by forced evaporation (Section 2.2.5). We ramp up the Transport trap[1], a much narrower dipole trap that will act as a dimple when we reach shallower traps (Figure 5.5) before any evaporation. In dipole traps, the trap volume increases as we decrease the trap depth. To increase the confinement and enhance the collision rate, we add a dimple potential to our trap in the final stages of the evaporation. We will refer to the combination of these dipole traps as dimple trap. Our evaporation sequence consists of four parts (Table 5.1):

- Ramping up of the Transport trap to 10 W power and keeping the CODT at 120 W per beam.
- "Pre-evaporation", where we keep the Transport trap 10 W but we lower the power of the CODT to 60 W per beam.

[1]Once the quantum gas microscope is complete, we will use this transport trap to displace the atoms to the Science chamber, where they will be trapped in the optical lattices, hence the name "Transport trap" (Section 3.4.6).

	Loading into the TODT	Pre-Evap	Main phase 1	Main Phase 2
Atom Number	$7.8(1) \times 10^7$	$2.5(2) \times 10^7$	$1.1(2) \times 10^7$	$1.8(2) \times 10^6$
Temperature (μK)	35.2(1)	19.5(5)	4.71(5)	0.18(3)
$\omega_{\text{Long}}/2\pi$ (Hz)	85(1)	52(1)	28(1)	30(1)
$\omega_{\text{Dipole}}/2\pi$ (Hz)	52(2)	34(1)	48(1)	107(1)
$\omega_{\text{Vertical}}/2\pi$ (Hz)	52(2)	34(1)	48(1)	107(1)
PSD	$4.6(2) \times 10^{-4}$	$2.2(2) \times 10^{-5}$	$7.6(4) \times 10^{-4}$	12.0(1)
Evaporation Efficiency	-	-0.64	4.45	5.25
Collision rate $s^{-}1$	121	18	36	811

TABLE 5.1: Table detailing the data of the evaporation process.

- Main evaporation, phase 1. Where we ramp down the Transport trap to 4.1 W and the CODT to 36.6 W per beam, their minimum value .
- Main evaporation, phase 2. Where we ramp down the Transport trap to 1.3 W and keep the CODT at 36.6 W per beam.

At the end of this sequence, we typically obtain a BEC of approximately $1.8(2) \times 10^6$ atoms. All the evaporation ramps are decaying exponentials of the form $e^{-t/\tau}$, with τ being the timescale of the ramp. In the following subsections we will show an overview of the several evaporation phases. In Section 5.2 we will discuss each characteristic of the BEC in more detail. The data used in this section is

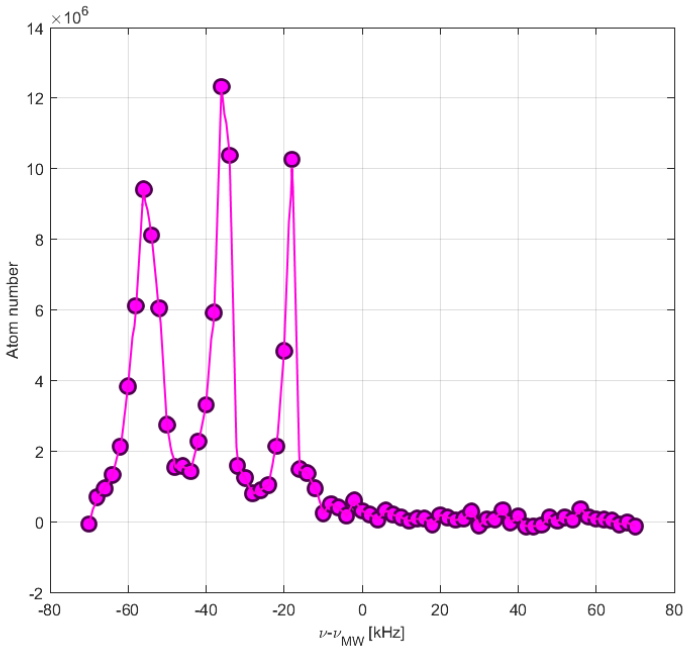

FIGURE 5.4: MW frequency scan after rapid adiabatic transfer. As in Figure 5.3, using the σ_+ $F = 2$ to $F = 1$ transition we probe in which m_F states are the atoms. The peaks correspond to the $|F = 1; m_F = -1\rangle \rightarrow |F = 2; m_F = -2\rangle$, the $|F = 1; m_F = -1\rangle \rightarrow |F = 2; m_F = -1\rangle$ and the $|F = 1; m_F = -1\rangle \rightarrow |F = 2; m_F = 0\rangle$ transitions. This proves that after the rapid adiabatic transfer the atoms are in the $|F = 1; m_F = -1\rangle$ state, as intended.

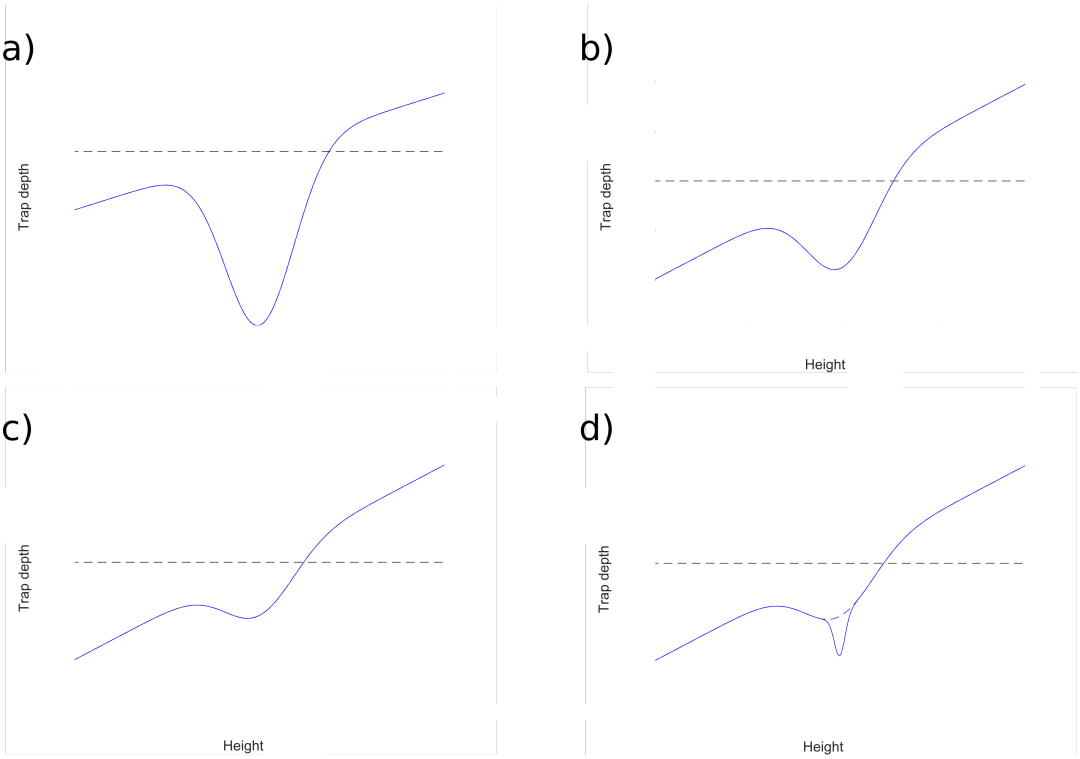

FIGURE 5.5: Calculations of the trap depth in the Vertical axis along the different phases of our evaporation sequence for the combination of CODT and Transport trap. a) is the loading of the atoms in the combination of CODT and Transport trap, b) is the pre-evaporation phase, the dashed line represents the potential without the dimple beam. c) is the first main evaporation phase and d) is the second main evaporation phase.

not the best we can produce but, after proving that we can produce quickly a large all-optical BEC, we decided to continue building the next stages of the two-species bosonic quantum gas microscope. The next subsections will only summarise the state of the cloud at each phase. See Table 5.1 and Figures 5.7 and 5.8 for the a breakdown of the values during the evaporation process.

Loading the atoms in the TODT

After loading the atoms in the crossed optical dipole trap (CODT), and after the optical pumping (OP) procedures, we ramp up the Transport trap to 10 W in order to create a combined potential with the CODT, the TODT (Figure 5.6) [2]. The focus of the Transport trap is then displaced from the centre of the CODT by 6 mm to create a larger trap volume (Figure 5.5). At this stage, the combined potential has a trap depth of approximately 350 µK and measured trap frequencies of $\omega_L = 2\pi \times 85(1)$ Hz, $\omega_D = 2\pi \times 52(2)$ Hz and $\omega_V = 2\pi \times 52(2)$ Hz on the Long, Dipole and Vertical axes. The temperature of the atoms is 35.2(1) µK and the atom number is

[2] Note that during the experimental sequence we displace the focus of the transport trap and so this figure just illustrates how the combined potential of the TODT and the CODT behaves when the focii of both traps overlap.

$7.8(1) \times 10^7$ atoms. Following that, we can calculate a phase-space density (PSD) [53, 46, 73] as per Equation 2.10 of $4.6(2) \times 10^{-4}$.

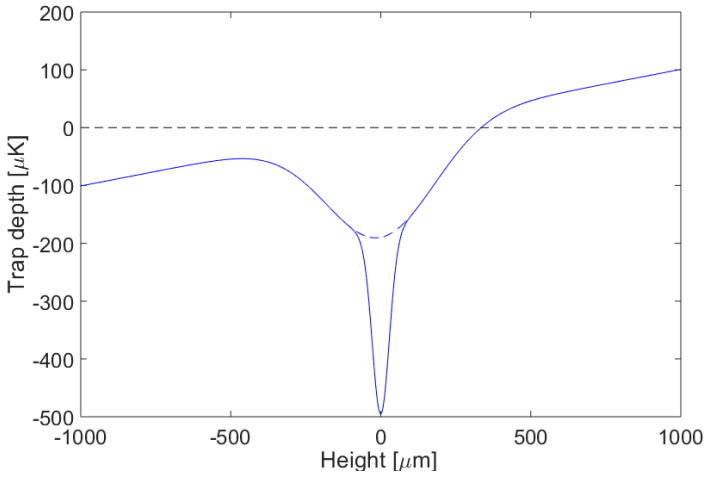

FIGURE 5.6: Calculation of the trap depth in the Vertical axis during the loading of the atoms in the combination of CODT and Transport trap. In this case we are showing the potential with no displacement of the focus of the transport trap, creating a Dimple trap configuration. As we are showing the Vertical axis, gravity is included in the simulation and that is the reason why the potential is tilted.

Pre-evaporation

Keeping the power of the Transport beam constant, we lower the intensity of the CODT beams to 60 W per beam, over 700 ms (Figure 5.5). The total trap depth is now 190 µK and the trap frequencies ($\omega_i/2\pi$) are 52(1) Hz, 34(1) Hz and 34(1) Hz for the Long, Dipole and Vertical axes, respectively. The atoms are now cooled to 19.5(5) µK, while the number of atoms decreases to $2.5(2) \times 10^7$ atoms. The PSD at this stage is $2.2(2) \times 10^{-5}$. The timescale of the ramp was 700 ms and the duration was 700 ms.

Main evaporation (phase 1)

During the first phase of the Main evaporation, the Transport trap power is decreased to 4.1 W and the CODT power to 36.6 W per beam, the minimum output of the CODT lasers. If not for the Transport beam acting as a Dimple trap over the larger volume of the CODT, the atoms would be lost to gravity as the CODT at that depth is not enough to hold the atoms against gravity (Figure 5.5). With the additional confinement of the Transport trap, the trap depth becomes approximately 50 µK. The trap frequencies are now 28(1) Hz, 48(1) Hz and 48(1) Hz for the Long, Dipole and Vertical axes. The temperature of the atoms at this phase is 4.71(5) µK and the atom number is $1.1(2) \times 10^7$. The PSD is now $7.6(4) \times 10^{-4}$. The timescale of the ramp is 900 ms and the duration is 900 ms.

Main evaporation (phase 2)

In the second phase of the Main evaporation, the CODT lasers are kept at their minimum power of 36.6 W while the power of the Transport trap is ramped down from 4.1 W to 1.3 W. The focus of the Transport trap is now displaced back to the centre of CODT. Focusing the Transport trap beam into the centre of the CODT enables us to reduce the volume of the trap and thus increasing the density of the atomic cloud and achieve higher trap frequencies (Figure 5.5). The trap depth is now approximately 1.8 µK and the trap frequencies for the Long, Dipole and Vertical axes are 30(1) Hz, 107(1) Hz and 107(1) Hz. The atom number at the end of the evaporation is $1.8(2) \times 10^6$ for an above 90% pure condensed cloud. As our thermal fraction is on the level of the noise, we cannot measure temperatures directly and thus we calculated the temperature of the cloud and the PSD by using Equation 2.24. The temperature after evaporation is then 0.18(3) µK. The PSD is 12.0(1). The duration of the final ramp is 1150 ms and the timescale is 1100 ms.

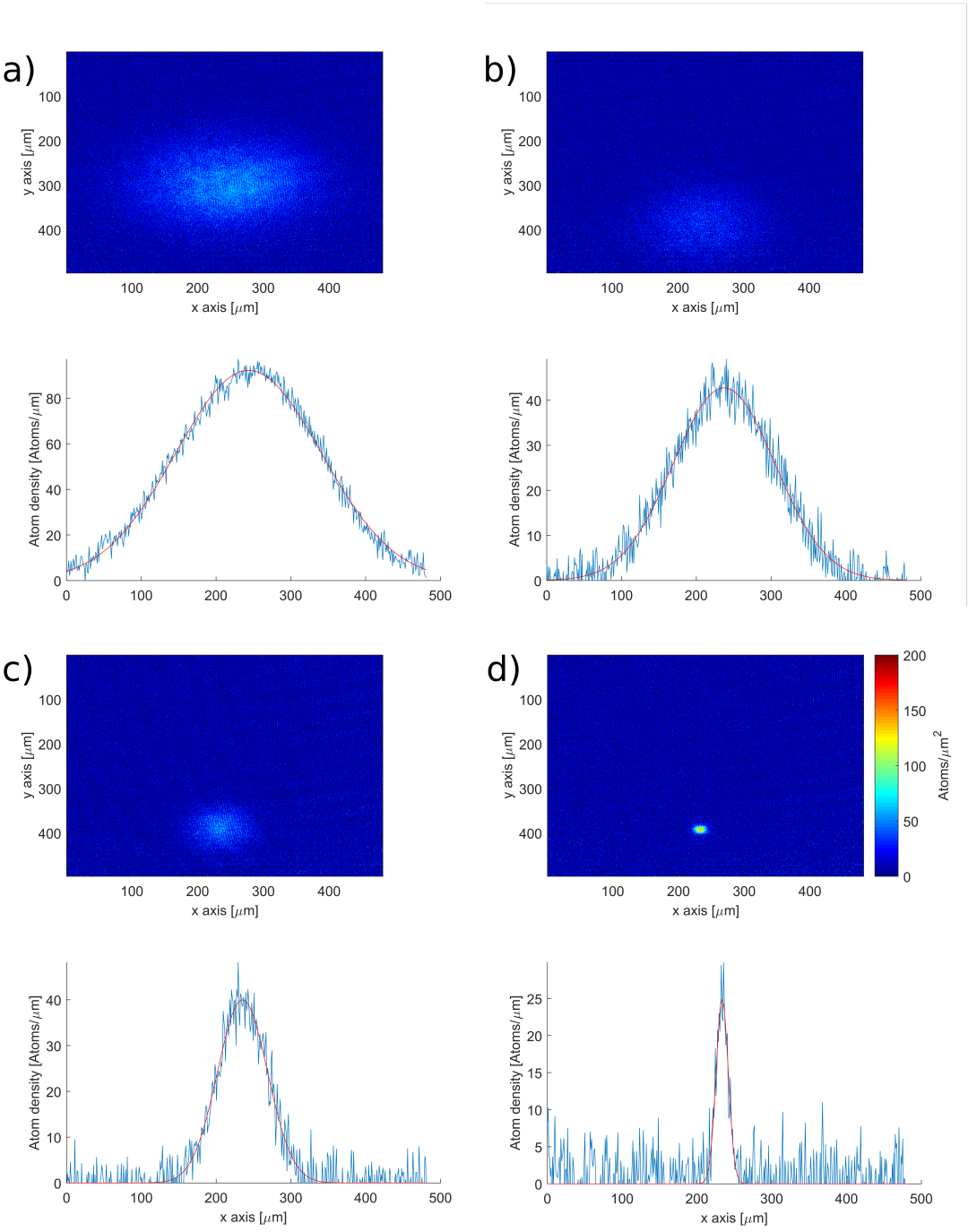

FIGURE 5.7: Atoms at the end of each of the evaporation phases (Section 5.1.3). a) is the loading of the CODT, b) the pre-evaporation, c) the first phase of the main evaporation and d) the second phase of the main evaporation. We only achieve Bose-Einstein condensation after the end of the second phase of the main evaporation. The density of atoms per µm increases as we proceed with the evaporation. All the pictures have the same TOF duration of 20 ms.

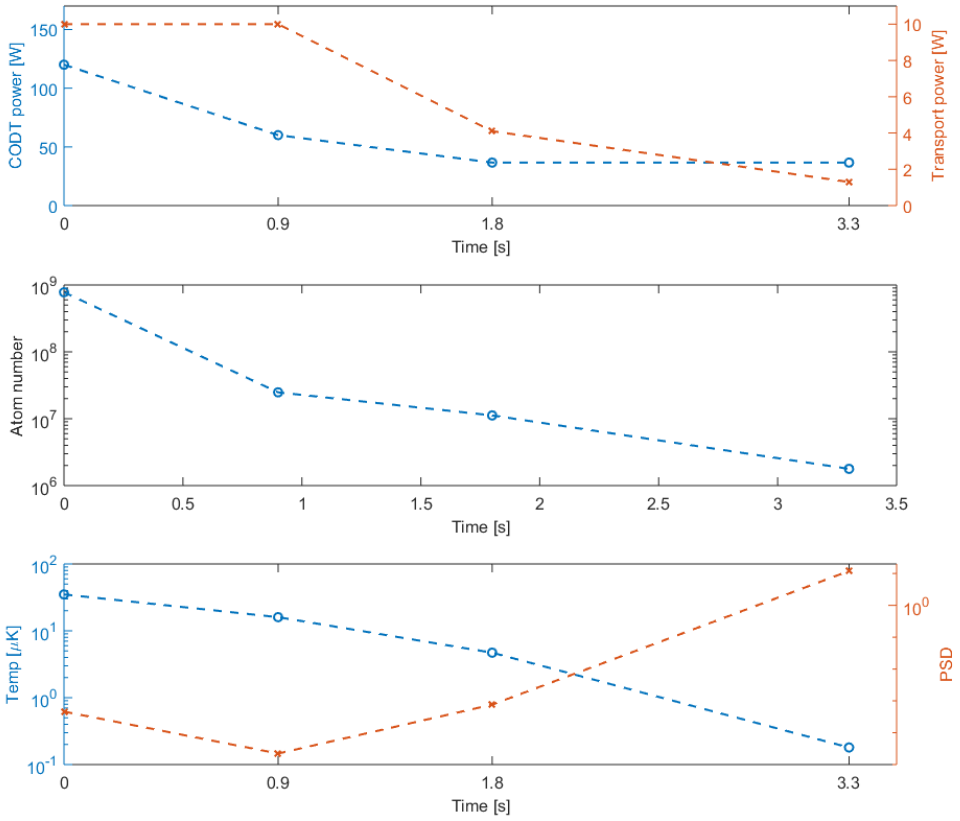

FIGURE 5.8: Summary of the evolution of the atomic cloud through the different evaporation phases.

5.2 Characterisation of the BEC

In order to optimise the creation of the Bose-Einstein condensate, we need to understand its characteristics. We start by focusing on the number of atoms that our final BEC possesses (Section 5.2.1) and which fraction of the final atomic cloud is a condensate and which fraction is thermal. After that, we will evaluate the phase-space density of the cloud at the different stages of the evaporation.

5.2.1 Atom number of the BEC fraction

When creating a BEC with a non-zero temperature, the cloud is a combination of thermal and condensed atoms. In order to distinguish the thermal fraction from the condensed fraction, we let the cloud fall for a certain time of flight (Section 4.1) so the thermal fraction expands and its profile can be fitted to a Gaussian distribution. The condensed fraction will expand more slowly than the thermal fraction, due to the mean field interaction [53]. We can only image our atomic clouds for a limited TOF duration before they fall out of view. We always want to image the full atomic cloud, so the smaller the cloud, the longer time-of-flight durations that we can employ. In the case of our smallest BECs, it is close to 30 ms. That TOF duration is not enough to measure an expansion of the BEC cloud.

We measure the atom number belonging to the BEC and to the thermal cloud by fitting both a Gaussian and Thomas-Fermi fit to the atomic cloud. By knowing the fraction of atoms that are thermal, i.e. fall under the approximately Gaussian distribution and how many are condensed , i.e. they are under the parabola of the Thomas-Fermi approximation (Section 2.3.2, Equation 2.21), we can extract the atom number of our BEC. Often, the condensed cloud is too dense to be imaged directly, so in order to image it we first need to make it less dense. That can easily be accomplished by repumping a fraction of the atoms to the imaging state. We detune the repumper frequency in a non saturated condensed cloud, in a similar manner to the off-resonant imaging shown in Section 4.1.1. For that purpose we load a fraction of the atoms in the 3D MOT and thus we achieve a BEC with a low enough number of atoms, approximately 5×10^5 atoms, that we can image in a non-saturated picture. By repumping a known fraction of atoms from $|F = 1; m_F = -1\rangle$ to $|F = 2; m_F = -2\rangle$ with different repumper detunings, we know how many atoms are actually in our atomic cloud. Once we know the total number, we fit the Thomas-Fermi parabola to the condensed cloud and the Gaussian fit to the thermal cloud (Figure 5.9). In the top row of Figure 5.9 we plot the x- and y-axes profiles of the atom density versus position. In blue we plot the actual data, in black the Gaussian fit of the thermal component and in red the parabolic fit of the condensed fraction. In the second row we have the raw data (left) and the reconstructed data from the fits of the first row (right). By substracting the fit from the data we obtain the final graph in this figure, the differential. In this particular instance, for both x- and y-axes profiles the condensed fraction is 0.14% of the total cloud.

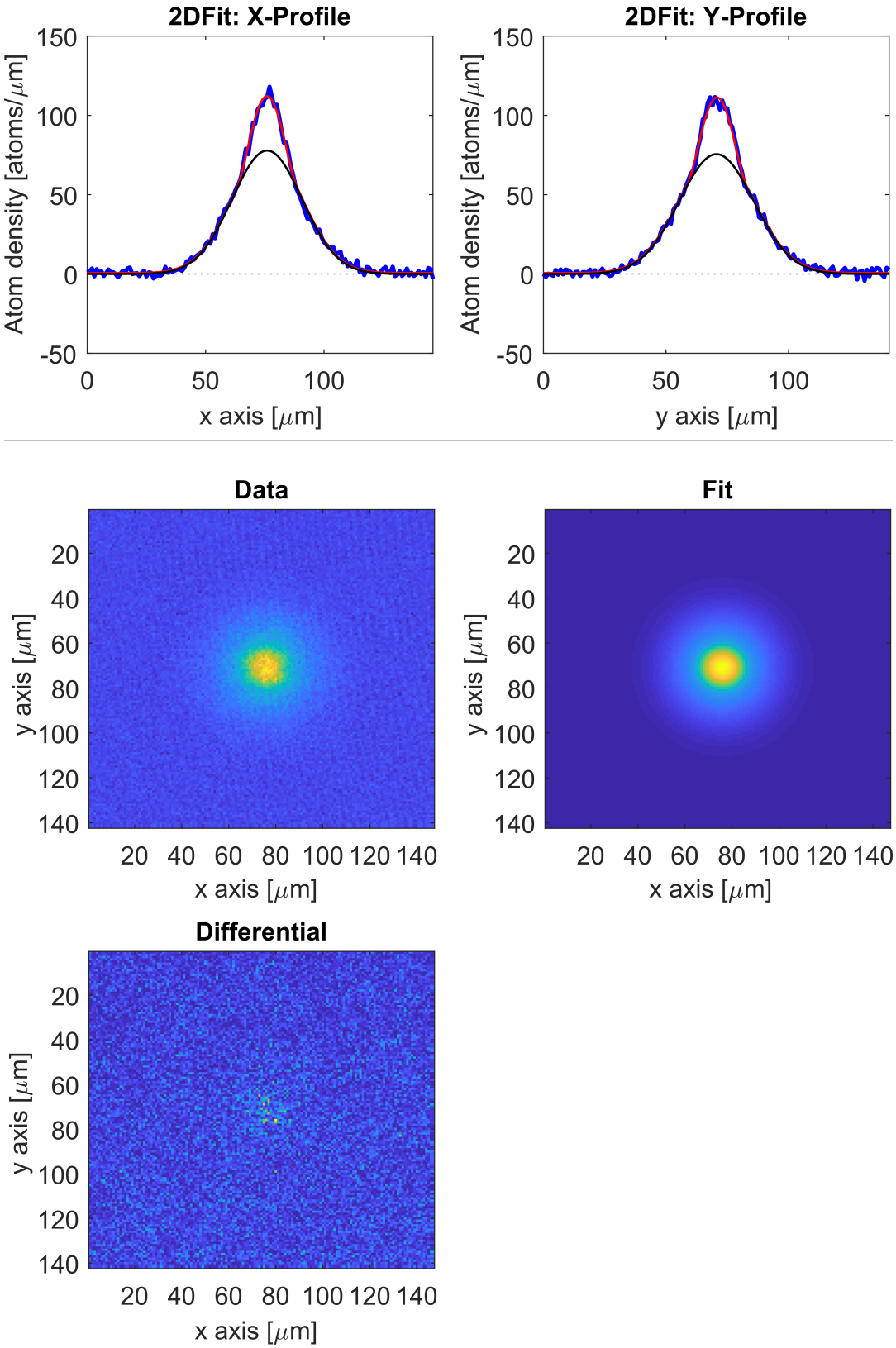

FIGURE 5.9: Obtaining the condensed fraction from a bimodal fit, Gaussian for the thermal fraction and a parabola for the condensed fraction, on the whole atomic cloud (Equation 2.21).

The only disadvantage is that by repumping a fraction of the condensed atoms, we also repump a fraction of the thermal atoms and thus sometimes we cannot achieve enough thermal atoms to properly calculate the thermal and condensed fractions.

We need to define an initial set of parameters for the bimodal fitting (Equations 2.21, 2.22), and so we consider that the atoms above 50% of the maximum signal will be part of the condensed fraction, while the atoms below will be part of the thermal cloud. We integrate the number of atoms in the fitted region and calculate the thermal and condensate fraction. In Figure 5.9 we present the data and the fits and the difference between the two of them.

When evaporating down to a BEC, it is very important to understand at which power to end the evaporation. The lower the trap depth, the colder our atoms, but the more atoms we will lose during the evaporation. If we do not reach temperatures below the critical temperature (Equation 2.19), the atoms will not condense. By plotting the atom number versus the evaporation endpoint and the condensed fraction versus the evaporation endpoint (Figure 5.10) we can understand how many atoms we keep in the trap and what fraction of those are condensed into a BEC. For example, if we could tune our evaporation parameters to obtain a very pure BEC but with a lower atom number or, by using a different set of parameters, we could just obtain a larger BEC with a larger thermal fraction (see Figure 5.11, showing the results of different evaporation endpoints). We could choose, for example, an endpoint of 0.95 V (approximately 1.4 W) for our transport trap laser. With that value, we obtain a condensed fraction of 0.65 and an atom number of 2.9×10^6 atoms. This results in a condensed atom number of 1.9×10^6 atoms.

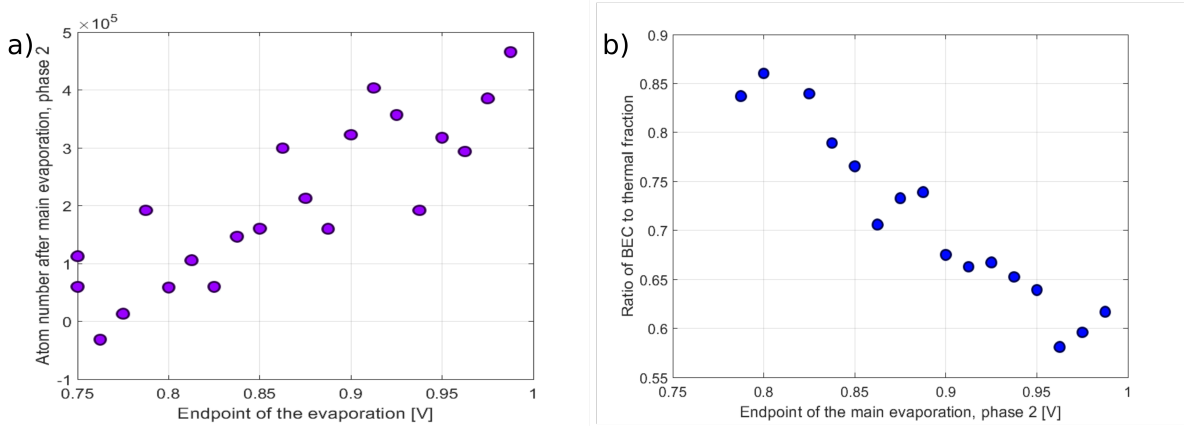

FIGURE 5.10: a) Atom number versus endpoint power of the evaporation, b) condensed fraction versus the endpoint of the evaporation. To achieve the largest number of atoms for a high BEC fraction, we need to choose cleverly the endpoint of our evaporation. The power plotted is in V as we use an AOM to regulate the power of the transport trap. The repumper laser is detuned to 2Γ and so the actual number of atoms is 9.53 times the one plotted.

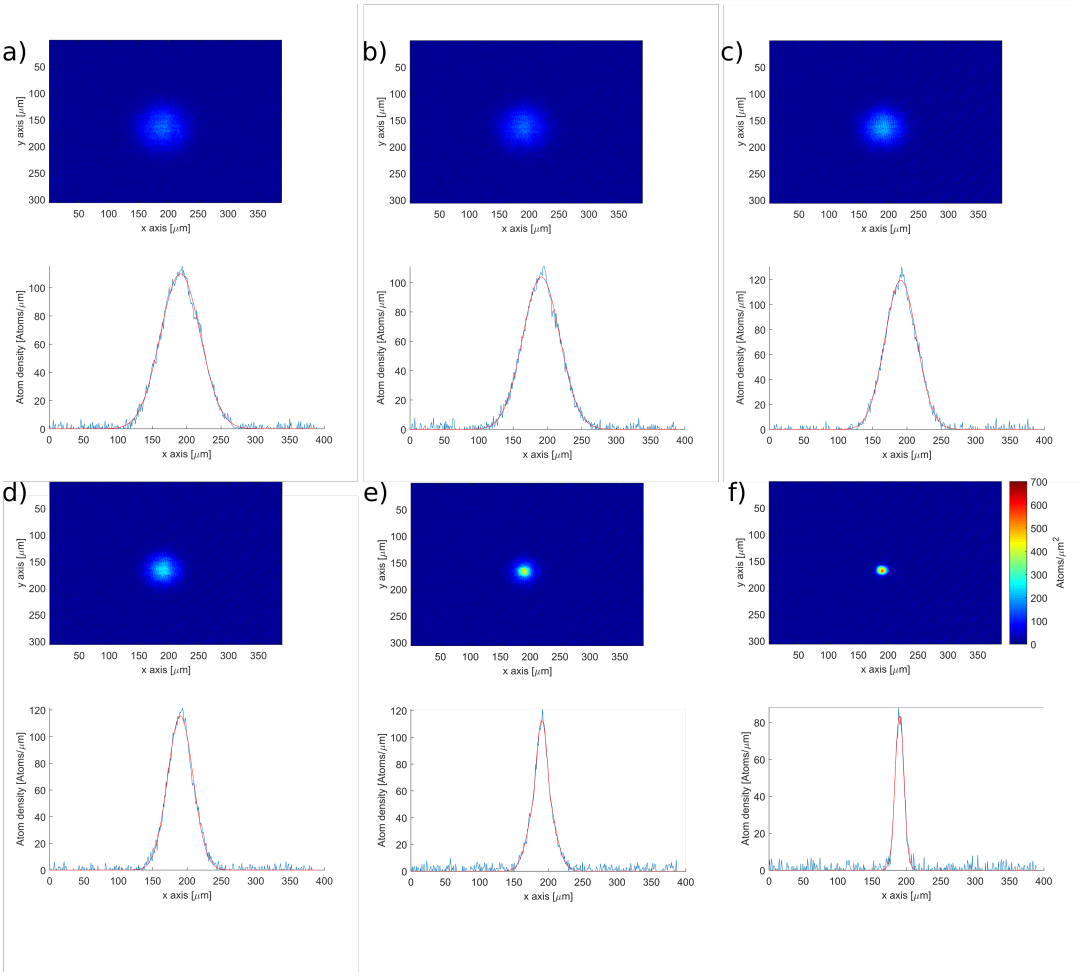

FIGURE 5.11: Atoms at different endpoints of the second phase of the main evaporation. a) corresponds to the endpoint of the first main phase. From a) to f) we decrease the power of the Transport trap from 4.1 W to 1.3 W in equal intervals. On e) there is a 50% of BEC condensation, while on f) we have above 90% condensed fraction.

5.2.2 Temperature of the thermal fraction

We cannot probe the temperature of the BEC directly but we can measure the temperature of the thermal fraction. We use a time-of-flight measurement of the evolution of the Gaussian profile of the thermal cloud (Section 4.1.2) for different time-of-flight durations.

After every phase of the evaporation, our atoms get colder. Before the evaporation process (Section 5.1.3), the atoms have a temperature of 35.2(1) µK (Figure 5.12) and after the pre-evaporation (Section 5.1.3), the temperature of the cloud drops to 19.5(5) µK (Figure 5.13). During the pre-evaporation phase we only ramp down the CODT lasers, keeping the Transport trap beam constant (Figure 5.5). Even though we still have not reached temperatures as low as after the grey molasses (3.3 µK, Section 4.4.3), the atoms are now colder than after the optical pumping with a PSD of 2.2×10^{-5}.

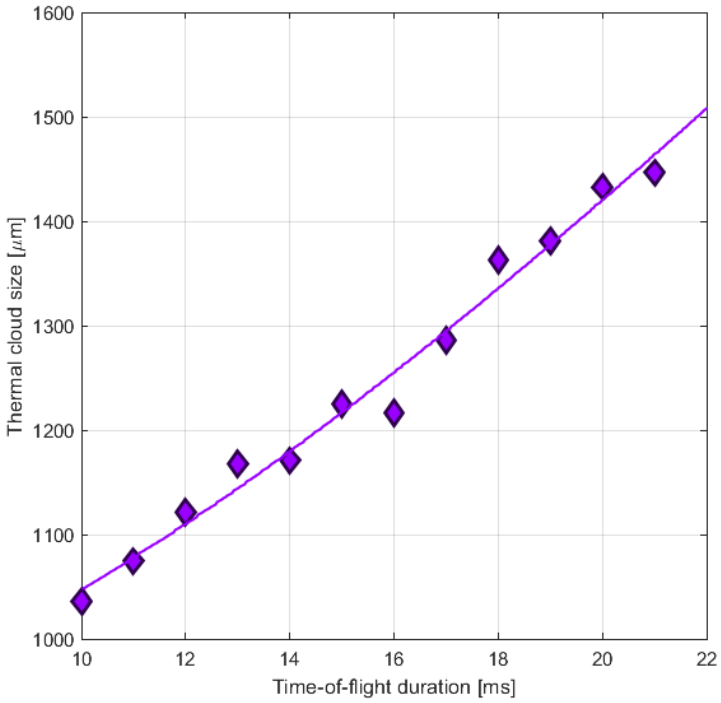

FIGURE 5.12: Temperature measurement before starting the evaporation, just after loading the atoms into the combination of the Transport trap and the crossed optical dipole trap (CODT). The temperature of the atoms is $T = 35.2(1)\mu K$ as per the fit obtained with Equations 4.9, 4.8.

After the pre-evaporation phase, the atoms are now cold enough so we can ramp down both CODT and Transport traps (Section 5.1.3). After the first main evaporation phase, the atoms are cooled to 4.71(5) µK (Figure 5.14). We are now approaching the temperatures obtained after grey molasses, but we have lost two orders of magnitude of atoms in the process (Table 5.1). Our PSD is 7.6×10^{-4}. It is possible that

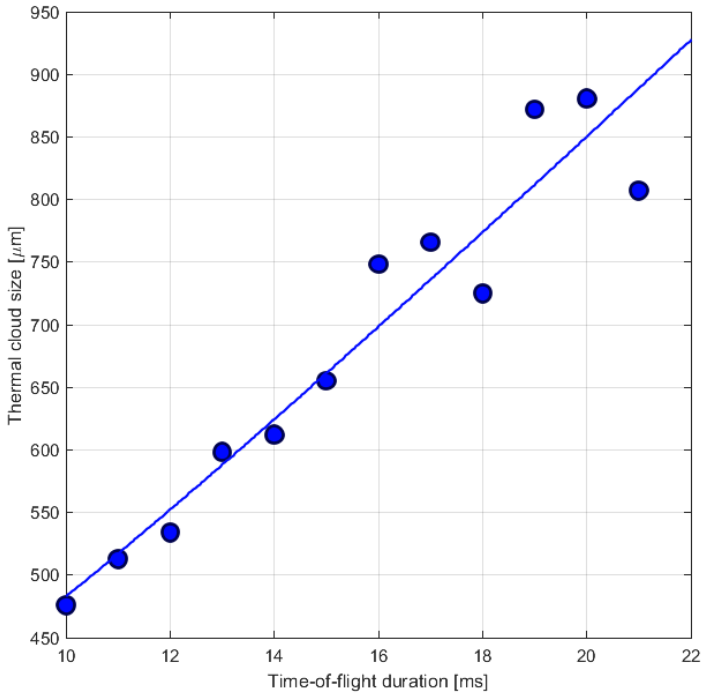

FIGURE 5.13: Temperature measurement after the initial evaporation. In this phase we keep the power of the Transport trap constant at 10 W and we lower the power of the CODT from 2×120 W to 2×60 W. The temperature of the atoms is $T = 19.5(5)\mu K$ as per the fit obtained with Equations 4.9, 4.8.

by adjusting some of the evaporation ramp parameters, such as the end points; duration or timescale, we could achieve lower temperatures or higher atom number in a more efficient way.

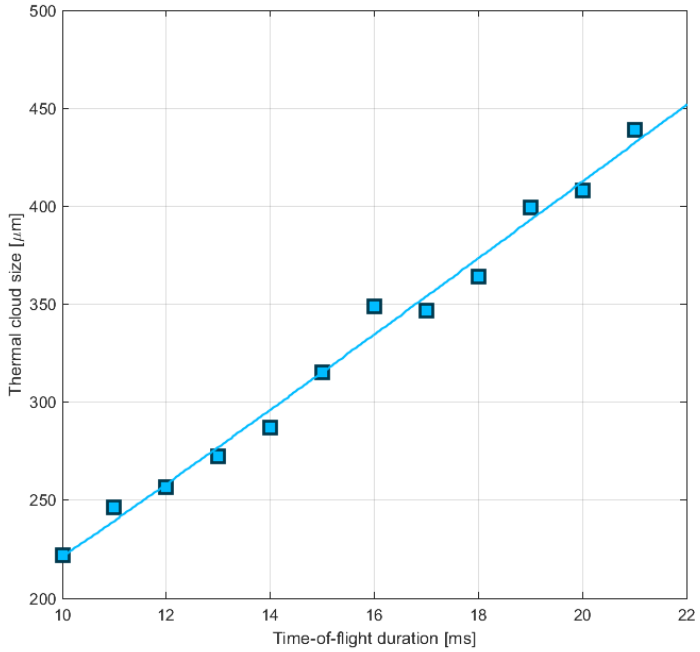

FIGURE 5.14: Temperature measurement after the first phase of the main evaporation. We lower the power of the Transport trap from 10 W to 4.1 W and we lower the power of the CODT from 2×60 W to 2×18.3 W. The temperature of the atoms is $T = 4.71(5)\mu K$ as per the fit obtained with Equations 4.9, 4.8.

In the final phase of the evaporation we bring back the focus of the Transport trap so it matches the focus of the CODT. This increases the density of our atoms, as they are confined in a tighter volume. Our CODT lasers are already at their minimum values, so we are only decreasing the depth of the Transport trap (Section 5.1.3). As our thermal fraction is on the level of the background noise, we cannot extract any information from it. Therefore, we calculate the temperature of the condensed fraction with Equation 2.24 and from it we obtain the PSD, collision rates and evaporation efficiencies at this stage. The temperature of the condensed fraction is 0.18 µK.

5.2.3 Phase-space density at several evaporation stages

Once we have measured the atom number (Section 5.2.1), temperature (Section 5.2.2) and trap frequencies (Section A.0.1) we can calculate the phase-space density (PSD, Section 2.3) of our atomic cloud by using Equation 2.14. By studing the PSD at different stages, we are able to know which stages can be improved and how, e.g. if we lose too many atoms from one stage to the next, with the temperature changing accordingly, we can either shorten the duration of the evaporation or evaporate to a different trap depth or both. The sequences that we use to create our BEC are a

proof of concept, and as such they can be optimised. By understanding Table 5.1 and Figure 5.15, we can improve the BEC creation process. In Figure 5.15 we plot the evolution of the PSD versus the atom number through the dfferent stages of a experimental run.

After the grey molasses stage, the PSD of the atoms is 1.9×10^{-2}. We calculate it from the following equation:

$$\text{PSD} = \left(\frac{n_{\text{MOT}}}{V_{\text{MOT}}}\right) \lambda_{dB}^3, \tag{5.1}$$

where n_{MOT} is the number of atoms after grey molasses, V_{MOT} is the in-situ volume of the MOT and λ_{dB} is the de Broglie wavelength. We measure the in situ trap volume by doing a temperature measurement and extrapolating to the minimum volume the cloud has for a given temperature and a time-of flight of 0 ms. The measured PSD is quite high for a molasses stage because we cool approximately 3×10^9 atoms to a temperature of 3.3 µK. The volume of the atomic cloud after grey molasses is much larger than the volume of the cross optical dipole trap and so when loading the atoms into the trap, the modes do not match and the atoms get heated. This is the reason behind the fact that, when loading into the CODT, we only retain a fraction of those atoms and they rethermalise to a tenth of the trap depth after 200 ms. The optical pumping (OP) heats them slightly and so the atoms end with a temperature close to 35 µK before the evaporation process. We could improve this situation simply by enlarging the beam waists of the CODT beams by a factor 2. Not only we will have a larger trap volume, being able to trap more atoms, but we will also have a shallower trap depth and the atoms will be heated less. All of these factors will result in a higher PSD than the current 4.61×10^{-4}. The high number of atoms in this stage and trap frequencies (Section A.0.1) result in a collision rate of 121 s^{-1} (Equation 2.15).

On the pre-evaporation stage, we lower only the power of the CODT and thus the trap frequencies drop (Section A.0.1). We lose an order of magnitude on the atom number and the atoms do not cool down enough so we can mantain or improve the PSD at this stage. The PSD changes from 4.61×10^{-4} to 2.22×10^{-5}, with a duration and timescale of 900 ms. The collision rates vary from 121 s^{-1} to 18 s^{-1}. Another way of studying why this stage needs to be optimised is from the perspective of the evaporation efficiency (Equation 2.18). The evaporation effciency at this stage is, $\gamma = -0.88$. A negative number implies that we lose more atoms than we improve the PSD. One way to improve this ramp would be to vary the duration and the matching timescale, choosing a shorter duration and keeping more atoms at a higher temperature. For that we would need to plot the atom number versus the ramp duration for the current evaporation endpoint of this ramp. In each of these datasets, the timescale and the duration of the evaporation should match, as the most efficient evaporation happens only when the timescale of the ramp matches the duration.

It is during the first main evaporation phase where we recover the PSD values

that we had before the pre-evaporation. The PSD at the end of the pre-evaporation is 2.22×10^{-5}, while at the end of the first main evaporation phase is 7.6×10^{-4}. Accordingly, the collision rates also improve from 18 s^{-1} to 36 s^{-1} and the evaporation efficiency is now 4.4. A factor that contributes to the improvements is the geometry of the trap during this stage. It is in this stage when the Transport trap is deep enough compared to the CODT so it actually acts as a Dimple trap. The Dimple configuration enhances the confinement along the Vertical and Dipole axes and thus, also the collision rates and the evaporation efficiency.

During the final stage of the evaporation we continue to improve the PSD greatly, bringing it up to 12.0. It is in this stage where we achieve condensation. The evaporation efficiency is now 5.25 and the collision rate is 811 s^{-1}. By moving the focus of the transport trap back to the overlap with the CODT we trap completely the atoms in the Dimple trap. While the evaporation efficiency is similar to the one achieved during the first main evaporation phase, the collision rate has improved by two orders of magnitude.

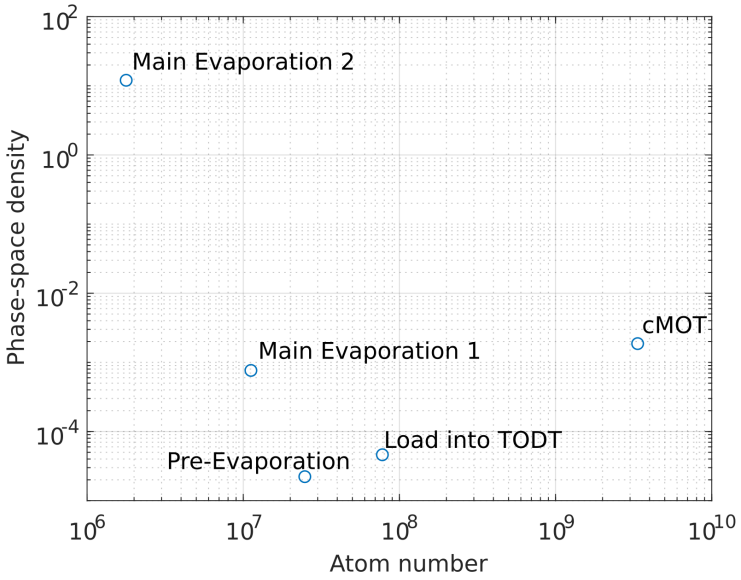

FIGURE 5.15: Evolution of the PSD and the atom number through the evaporation process.

5.3 Conclusions

In this chapter we have described the loading into the dipole traps, the state preparation and the evaporation process that lead into the BEC creation. We load approximately 7×10^8 atoms and after 3.3 s of evaporation we achieve a Bose-Einstein condensate close to 2×10^6 atoms. In Figure 5.16 we illustrate the state-of-the-art in BEC creation. The data points represented by a "+" belong to groups that created their BECs in atom chips [74, 75, 76, 77, 78], the squares (□) to groups with all-optical BECs [79, 80, 81, 82], the diamond (◇) to a group that employed magnetic traps in order to achieve Bose-Einstein condensation [83] and the black star (⍟) to what is presented in this thesis. All the groups mentioned in this section employ ^{87}Rb except [77] (dual BEC with ^{87}Rb and ^{40}K), [80] (^{84}Sr) and [78] (^{174}Yt).

Our full experimental sequence takes 2750 ms until the absorption imaging process. That means that we are able to create an all-optical BEC in less than 3 s, and so we employ one of the shortest experimental sequences for BEC creation in the world [83, 81, 76, 75, 74, 82] (Section 5.3, Figure 5.16). It is critical to understand how the duration and timescales of the evaporation ramps affect the end results. We can achieve a better evaporation efficiency by choosing the duration of each of the evaporation ramps. Depending on the final trap depth and the PSD of the cloud, sometimes extending the duration of the evaporation ramp does not add any advantage as we might lose more atoms and do not achieve a lower temperature. It is better to proceed with the next evaporation stage with more atoms, as we can improve the evaporation efficiency by optimising evaporation parameters such as ramp duration and timescale, final and initial trap depths and displacement of the focus of the Transport trap.

Our experiment posseses the second highest atom number of the list, second only to the Mun group [83] (red diamond in Figure 5.16), as they have 2×10^7 atoms compared to our 1.78×10^6 atoms. Our cycle time is approximately six times faster as we designed our experiment for high repetition rates. Regarding the other all-optical BECs [79, 80, 81, 82] (red square, blue square, magenta square and green square in Figure 5.16, respectively), our experiment is the one with the highest atom number in the BEC, 1.8×10^6 atoms compared to the 1.2×10^6 atoms of the Kinoshita group [82] (green square). Our experimental cycle time is shorter than the Kinoshita group, as it is only 4.3 s while their sequence is 5.8 s long. Regarding the remainder of the all-optical groups, our all-optical BEC posseses a higher atom number and our sequence is faster than the one produced by Aspect [81] (magenta square), as the atom number is 1.5×10^5 and the sequence lasts 7 s. The BECs from Weiss' group [79] (red square) and Grimm's group [80] (blue square) have 3.5×10^5 and 1.15×10^5 atoms and their cycle times are 3.3 s and 2 s long, respectively.

In conclusion, with our current experimental setup we are able to produce by

employing our Λ-enhanced grey molasses (Section 4.4) and our dimple trap configuration (Section 5.1) the largest all-optical BEC in the world in a shorter total repetition rate that the second largest one.

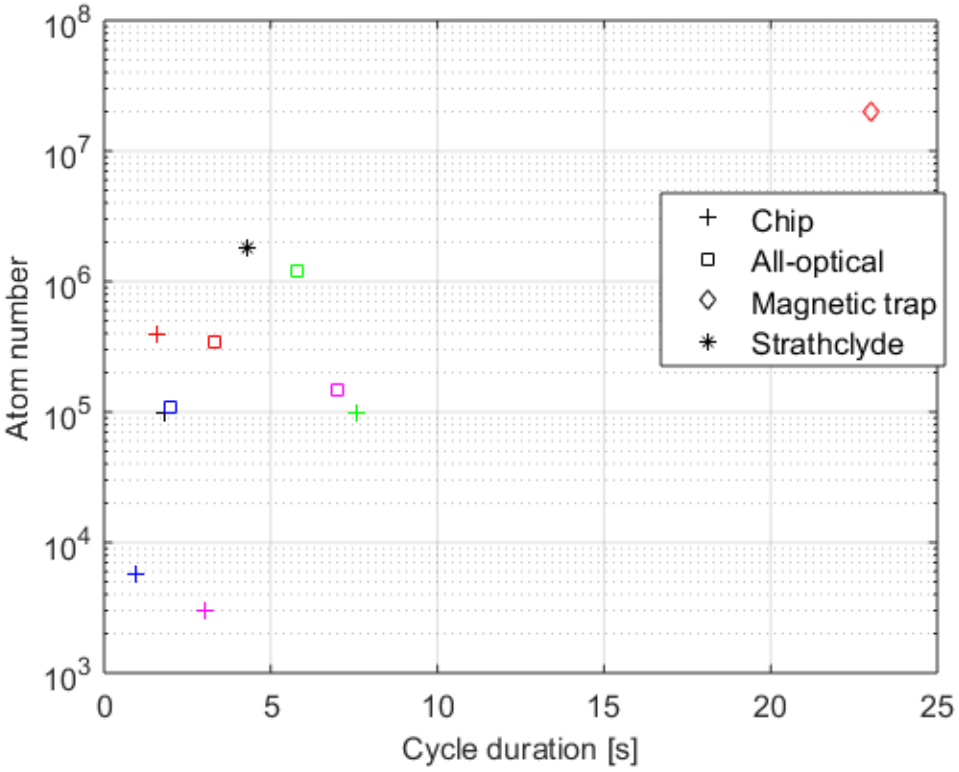

FIGURE 5.16: Comparison of atom number and cycle time between different BECs. Atom numbers and sequence durations taken from: experiments with atom chip traps + [74], + [75], + [76], + + [78], experiments with all optical traps □ [79], □ [80], □ [81], □ [82], magnetic trap ◇ [83].

Chapter 6

Future goals and conclusions

6.1 Conclusions

Along the course of this PhD, we have set up the foundations of the two-species bosonic quantum gas microscope from scratch. My main contributions, as reflected in Chapter 3, are the design, set up and characterisation of the laser systems employed in the experiment. We demonstrated that we can trap and cool a cloud of atoms of approximately 3×10^9 atoms to temperatures close to 40 µK after our compressed magneto-optical trap. In the grey molasses cooling stage the atoms are further cooled down to temperatures of the order of 4 µK, an order of magnitude less (Section 4.5). The phase-space density of the atomic cloud after grey molasses is 1.9×10^{-2} (Section 5.2.3).

We are able to load close to 7×10^8 atoms (Section 5.1.1) in the combination of crossed optical dipole trap (CODT) plus Transport trap.

After the evaporation process (Section 5.1.3), we achieve a Bose-Einstein condensate of approximately 1.8×10^6 atoms (Section 5.2.1), at a temperature of 180 nK (Section 5.2.2) and a phase-space density of 12.0 (Section 5.2.3). To our knowledge, this is the largest all-optical Bose-Einstein condensate and our cycle time is one second shorter than what has been reported by other groups (Section 5.3, Figure 5.16).

We believe that further improvements can be made by fine tuning our evaporation sequence, increasing the beam waist of the crossed optical dipole trap by a factor 2 and by optimising the relative positions of the magneto-optical cloud and a larger crossed optical dipole trap.

6.2 Towards a two-species quantum gas microscope

The setup described in this thesis will comprise the initial stages of a bosonic two-species quantum gas microscope. We have described the initial cooling and trapping of the atoms, as well as the theoretical background and experimental setup required to achieve Bose-Einstein condensation. The next steps will move the experiment towards a fully functional quantum gas microscope.

The next milestone will be the transport and imaging of cold ^{87}Rb atoms in the Science chamber. After that, we will set up the optical lattice system and create a

BEC in the Science chamber (Section 6.2.1). Setting up the microscope and imaging single atoms in an optical lattice will be next (Section 6.2.2). The final step will be setting up the cooling lasers for ^{85}Rb and creating a two-component Bose-Einstein condensate (Section 6.2.3). In this stage, control over the scattering length employing Feshbach resonances will be key to avoid heavy ^{85}Rb losses.

As shown in Section 5.1.3, we can create a BEC in 4.3 s. Considering that we can transport the atoms from the MOT chamber to the Science chamber (see Section 3.4.6 for a description of the displacement of the focus of the Transport beam) in approximately 1 s, we can be confident that our repetition rate will be in the order of 10 s.

Another characteristic feature of our experiment will be the possibility to explore different lattice geometries besides the square one, such as double-well potentials, triangular lattices, hexagonal lattices and kagome lattices. Initially we will be able to create a square lattice configuration, but later on by rearranging the optics on our lattice setups and adding an additional beam in the horizontal plane, we will be able to explore the additional, more exotic, configurations such as triangular lattices. With the aid of a spatial light modulator, lattice geometries like the hexagonal or kagomé lattices can be explored.

6.2.1 Bosons in an optical lattice

Before imaging with the microscope and adding the second species of rubidium, we need to be able to trap atoms in an optical lattice in the Science chamber. Instead of creating a BEC in the MOT chamber and transporting it, as we have shown in this thesis (Section 5), we will cool evaporately the atoms and then transport them to the Science chamber and evaporate them further there to create the BEC. Transporting a BEC over a distance of 25 cm is no trivial task and heavy losses are involved in it. We expect losses due to three-body recombinations and heating caused by motional excitations during the transport process. For a gas of thermal atoms, we have already done some preliminary tests consisting of the transport of a cloud of cold thermal atoms to and from the Science chamber and have observed a transfer efficiency above 99%. Once we are able to create a BEC in the Science chamber, we will set up the optical lattices, the microscope objective and move on to single atom imaging.

6.2.2 Single-species bosonic quantum gas microscope

Adding ^{85}Rb creates an additional degree of complexity in the experiment and will require some time to set up. This is why, for the initial tests of the microscope and single atom imaging, we will use only ^{87}Rb. Cold atoms in optical lattices are the perfect media to observe quantum phases such as the bosonic Mott insulator, and to measure their entropy and temperature [24]. Other interesting phenomena are dynamics of utra-cold atoms in optical lattices. We could study correlation spreading after quenching the lattice depth [84] now possible in two dimensions due to

the higher repetition rate; which will lead to better statistics, of out-of-equilibrium dynamics after a deterministic preparation of spin impurities [20], thermalisation of individual atoms in an optical lattice and the entanglement entropy [85].

We make use of a preparation technique for imaging single layers of atoms in an optical lattice, which is based on a clever use of magnetic gradients, Zeeman splitting and transfering the atoms to the other hyperfine state via microwave transition [86]. With the addition of a spatial light modulator, we will be able to address single atoms in the optical lattice. This will enable us to prepare the atoms in a number of configurations and to explore phenomena such as spin-flip perturbations in Mott insulators, i.e. changing the spin of a single atom in a Mott insulator and observe how the pertubation propagates through the system.

6.2.3 Two-species bosonic quantum gas microscope

One of the characteristics of ^{85}Rb is the existence of several Feshbach resonances [87], especially the one at a magnetic field value of 155 G. Feshbach resonances allow us to control the inter-species scattering lengths between atoms in specific magnetic states. The nature of the scattering lengths can be set so the resulting interactions are repulsive, attractive or non-interacting. If the scattering lengths result in an attractive interaction, the atoms might form metastable molecules. If the scattering length is repulsive, the atoms will collide with each other. In order to cool by forced evaporation a sample of both ^{85}Rb and ^{87}Rb atoms, the scattering length should be in the order of $100a_B$, where a_B is the Bohr radius, for an ideal evaporation.

We control the scattering lengths by employing a set of high current magnetic coils. ^{85}Rb is prone to heavy losses and heating unless the inter-species interaction strength is carefully optimised to avoid losses all along the experimental sequence [88]. We designed our experiment in such a way that the required control over the Feshbach resonances is possible in both chambers and during the transport of the atoms, with the aforementioned set of high-current magnetic coils.

Once we are able to observe atoms in an optical lattice, we will complete the ^{85}Rb laser setup and will optimise the laser cooling for ^{85}Rb. We will use the existent optical fibres for ^{87}Rb and we will overlap the ^{85}Rb beams with the ^{87}Rb beams before coupling the latter into the optical fibres. Our first milestone will be to create a Bose-Einstein condensate of ^{87}Rb and ^{85}Rb simultaneously. Our group will employ sympathetic cooling to cool down ^{85}Rb with the existing ^{87}Rb system. After creating the BECs we want to be able to image each of the rubidium species separately. With our two-species quantum gas microscope we will be able to probe systems modeled by the two-component Bose-Hubbard model [89]. A possible future direction before moving on to the quench dynamics in 1D and 2D with tuneable interactions and correlation spreading and effective spin-models with tuneable interactions in 1D and 2D is the observation of a bi-atomic Mott insulator phase with a single atom resolution.

In Chapter 1 we have introduced the Bose-Hubbard model for bosons in periodic potentials (Equation 1.2) and we have explained some of the different phenomena that we can describe with it and what can we explore with the single species bosonic quantum gas microscope (Section 6.2.2). By adding a second species to the optical lattice, we can study the two-component Bose-Hubbard model [89]:

$$\begin{aligned} H = &- \sum_{\langle i,j \rangle} t_a (a_i^\dagger a_j + \text{h.c.}) - \sum_{\langle i,j \rangle} t_b (b_i^\dagger b_j + \text{h.c.}) + U \sum_i (n_{ai} - \frac{1}{2})(n_{bi} - \frac{1}{2}) \\ &+ \frac{1}{2} \sum_{i,\alpha=a,b} V_\alpha n_{\alpha i}(n_{\alpha i} - 1) - \sum_{i,\alpha} \mu_\alpha n_{\alpha i}, \end{aligned} \tag{6.1}$$

where t_a, t_b are the tunneling rates for species a and b, $a^\dagger, b^\dagger$ and a, b are their creation and annihilation operators, U is the inter-species interaction strength, controlled by the Feshbach resonance, $n_{\alpha i}$ is the number of atoms of species a or b localised in lattice site i, V_α is the intra-species potential and μ_α the chemical potential. $\langle i, j \rangle$ denote nearest neighbour lattice sites. The occupation of the atoms in the lattice sites maps to spin Hamiltonian models. By controlling the intra-species interaction caused by the Feshbach resonance, we will be able to explore two-dimensional systems only 4 atoms in width. These systems will present some degree of frustration and structures like ladders or checkerboards [90]. Once we modify the lattice optics for triangular lattices, and thus also being capable of hexagonal or kagomé lattices, our group will be able to simulate frustrated systems. These are systems where the atoms are organised in such a geometry that once two spins are defined, the third one cannot be opposite to both at the same time and thus is in a superposition of the two states. The aforementioned superposition leads to a precession of the spin and this phenomenon opens the door to study novel dynamics.

Appendix A

Trap frequency measurements during evaporation

A.0.1 Trap frequencies and trap volumes of the dipole trap

To calculate the phase-space density (PSD) of the cloud at every phase of the evaporation, we need to measure the frequencies of the trap. If the atoms are cold enough, they will be resting at the bottom of the trap and, to a first approximation, the potential will be a harmonic one. By making the atoms slosh along the bottom of the trap and by measuring the breathing of the cloud we can understand how the volume and the frequecies of the trap behave for different stages of the evaporation.

We use a small cloud of atoms, as we obtain a better signal to noise ratio with it. For sloshing, it is easier to measure a movement on the order of 100 µm if the size of the cloud is of that magnitude or smaller. A similar reasoning can be applied to the breathing measurements.

We make the atoms slosh, and breathe, by suddenly changing the intensity of one of the beams that form the optical dipole trap. We have found that we can control to a high degree of precision the intensity of our beams in 1 ms. During 1 ms we increase and then we bring the intensity back to the previous value and keep the atoms trapped for a variable amount of time. By releasing the atoms from the trap at different time intervals, we are able to plot the different positions of the centre of the cloud as a function. This results in a damped sine plot, not dissimilar to having a bit of water in a bowl and gently shaking it, so the blob of water sloshes about until it stops. The frequency of the damped sine is the frequency of the trap. While the cloud sloshes, it also breathes, i.e. expands and contracts in a periodic manner. The breathing frequency is double the trap frequency and can be obtained by measuring the cloud size for several sloshing durations and fitting a damped sine to the results. Depending on how easy it was for us to measure position or cloud size for each evaporation stage we have measured either the sloshing or the breathing frequency (Figures A.1, A.2, A.3, A.4).

When loading the atoms in the combination of crossed optical dipole trap (CODT) and transport trap, we displace the focus of the dipole trap 6 mm away. That enables us to create a shallower trap with a larger trap volume. Observing the values of the frequencies in Table 5.1, we observe that the containment along the

Transport axis is tighter, with a frequency of 85 Hz. On the Dipole and Vertical axes, the frequencies are 52 Hz for both of them (Figure A.1). In this initial phase, the transport trap does not provide a dimple trap configuration, as the powers of the CODT beams are too high (120 W per beam, Figure 5.5).

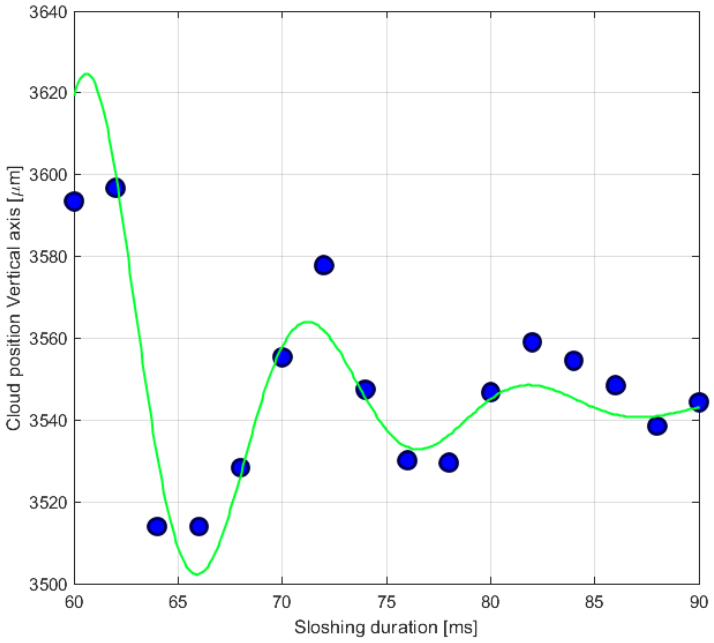

FIGURE A.1: Trap frequency measurement before the evaporation process along the Vertical axis. The measured trap frequency is $\nu_{\text{trap}} = 85(1)$ Hz. The CODT are at 2×120 W and the Transport beam at 10 W.

For the pre-evaporation phase, we only lower the power of the CODT beams, to 60 W each. As a result, the trap frequency on the Transport axis is 52 Hz (Figure A.2), while in the Dipole and Vertical axes it is 34 Hz. The combined trap is still mainly the CODT, with only a small contribution of the Transport trap (Figure 5.5).

During the first main evaporation phase, we lower both the CODT beams and the transport one. The CODT beams are lowered to their minimum output of 36.6 W, while the transport trap is lowered to 4.3 W. It is in this phase where we observe a reversal of the trap frequency values, with the Transport axis trap frequency being 28 Hz (Figure A.3) and the Vertical and Dipole 48 Hz. This means that the CODT powers are low enough so the transport trap acts as a dimple trap, as we can see in Figure 5.5. For the final stage of the evaporation we lower the transport trap value to 1.3 W and overlap the focus of the transport trap with the CODT (Figure 5.5). In this fashion we reduce the volume of the trap, increasing greatly the trap frequencies on all the axes. On the Transport axis, we have a trap frequency of 30 Hz (Figure A.4), while on the Dipole and Vertical axes we have trap frequencies of 107 Hz. The increased trap frequencies result on a higher collision rate and evaporation efficiency (Table 5.1, see Section 5.2.3 for a more detailed explanation on those topics).

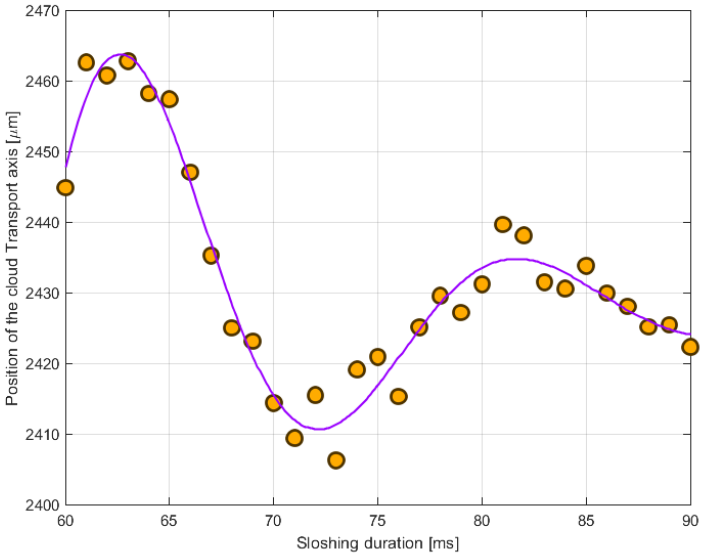

FIGURE A.2: Sloshing frequency measurement after the pre-evaporation phase along the Transport axis. The measured trap frequency is $\nu_{\text{trap}} = 52(1)$ Hz. The CODT are at 2×60 W and the Transport beam at 10 W.

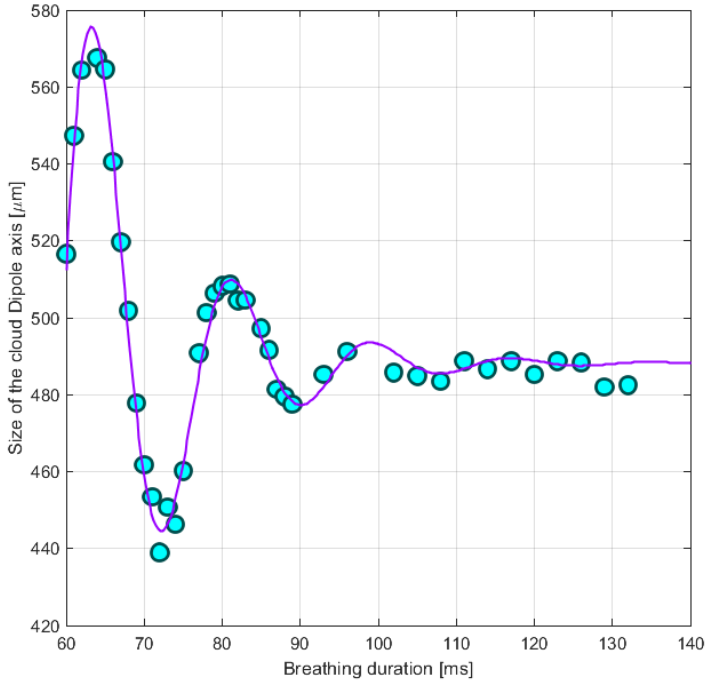

FIGURE A.3: Breathing frequency measurement after the first main evaporation phase along the Transport axis. The breathing frequency is twice the trap frequency, and has a value of $\nu_{\text{breathing}} = 55.9(5)$ Hz. The trap frequency is $\nu_{\text{breathing}}/2 = \nu_{\text{trap}} = 28(1)$ Hz. The CODT are at 2×18.3 W and the Transport beam at 4.3 W

.

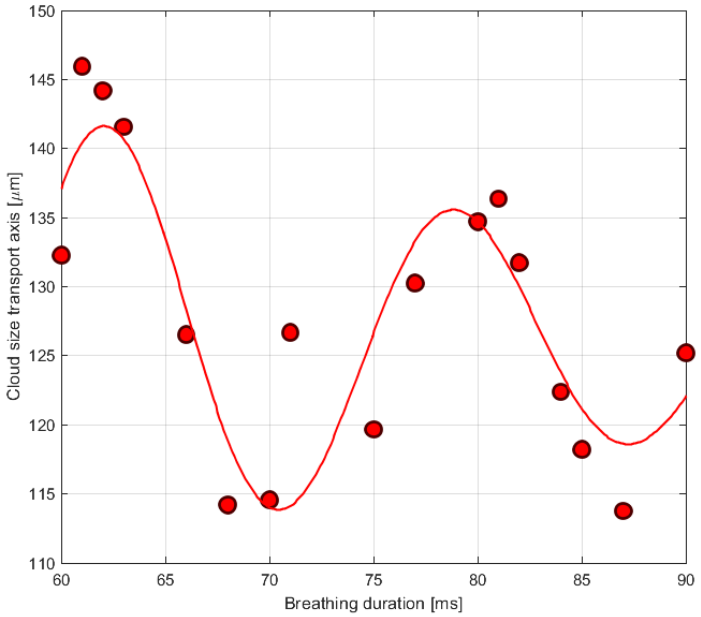

FIGURE A.4: Breathing frequency measurement after the end of the evaporation along the Transport axis. The breathing frequency has a value of $\nu_{\text{breathing}} = 59(1)$ Hz. The trap frequency is $\nu_{\text{breathing}}/2 = \nu_{\text{trap}} = 30(1)$ Hz. The CODT are at 2×18.3 W and the Transport beam at 1.3 W.

Bibliography

[1] A. G. Van Melsen. *From atomos to atom: The history of the concept atom*. Courier Corporation, 2004.

[2] H. E. Le Grand. "Galileo's Matter Theory". In: *New Perspectives on Galileo*. 1978, pp. 197–208.

[3] J. Dalton. *A new system of chemical philosophy*. Vol. 1. Cambridge University Press, 2010.

[4] J. J. Thomson. "Cathode rays". In: *The London, Edinburgh, and Dublin Philosophical Magazine and Journal of Science* 44 (1897), pp. 293–316.

[5] H. Geiger. "The scattering of α-particles by matter". In: *Proceedings of the Royal Society of London. Series A, Containing Papers of a Mathematical and Physical Character* 83 (1910), pp. 492–504.

[6] M. Planck. "On the law of distribution of energy in the normal spectrum". In: *Annalen der Physik* 4 (1901), p. 1.

[7] T. W. Hänsch and A. L. Schawlow. "Cooling of gases by laser radiation". In: *Optics Communications* 13 (1975), pp. 68–69.

[8] D. J. Wineland, R. E. Drullinger, and F. L. Walls. "Radiation-pressure cooling of bound resonant absorbers". In: *Physical Review Letters* 40 (1978), p. 1639.

[9] S. Chu, L. Hollberg, J. E. Bjorkholm, A. Cable, and A. Ashkin. "Three-dimensional viscous confinement and cooling of atoms by resonance radiation pressure". In: *Physical Review Letters* 55 (1985), p. 48.

[10] J. Dalibard and C. Cohen-Tannoudji. "Laser cooling below the Doppler limit by polarization gradients: simple theoretical models". In: *J. Opt. Soc. Am. B, JOSAB* 6 (1, 1989), pp. 2023–2045.

[11] A. Aspect, E. Arimondo, R. Kaiser, N. Vansteenkiste, and C. Cohen-Tannoudji. "Laser cooling below the one-photon recoil energy by velocity-selective coherent population trapping: theoretical analysis". In: *JOSA B* 6 (1989), pp. 2112–2124.

[12] G. D. Bruce, E. Haller, B. Peaudecerf, D. A. Cotta, M. Andia, S. Wu, M. Y. H. Johnson, B. W. Lovett, and S. Kuhr. "Sub-Doppler laser cooling of ^{40}K with Raman gray molasses on the D_2 line". In: *J. Phys. B: At. Mol. Opt. Phys.* 50 (2017), p. 095002.

[13] S. Rosi, A. Burchianti, S. Conclave, D. S. Naik, G. Roati, C. Fort, and F. Minardi. "Λ-enhanced grey molasses on the D_2 transition of Rubidium-87 atoms". In: *Sci Rep* 8 (2018), pp. 1–9.

[14] E. L. Raab, M. Prentiss, A. Cable, S. Chu, and D. E. Pritchard. "Trapping of Neutral Sodium Atoms with Radiation Pressure". In: *Phys. Rev. Lett.* 59 (1987), pp. 2631–2634.

[15] S. Chu, J. Bjorkholm, A. Ashkin, and A. Cable. "Experimental observation of optically trapped atoms". In: *Physical Review Letters* 57 (1986), p. 314.

[16] N. Masuhara, J. M. Doyle, J. C. Sandberg, D. Kleppner, T. J. Greytak, H. F. Hess, and G. P. Kochanski. "Evaporative cooling of spin-polarized atomic hydrogen". In: *Physical Review Letters* 61 (1988), p. 935.

[17] M. H. Anderson, J. R. Ensher, M. R. Matthews, C. E. Wieman, and E. A. Cornell. "Observation of Bose-Einstein condensation in a dilute atomic vapor". In: *Science* 269 (1995), pp. 198–201.

[18] W. Ketterle and N. J. van Druten. "Bose-Einstein condensation of a finite number of particles trapped in one or three dimensions". In: *Physical Review A* 54 (1996).

[19] M. Greiner, O. Mandel, T. Esslinger, T. W. Hänsch, and I. Bloch. "Quantum phase transition from a superfluid to a Mott insulator in a gas of ultracold atoms". In: *Nature* 415 (2002), p. 39.

[20] T. Fukuhara, A. Kantian, M. Endres, M. Cheneau, P. Schauß, S. Hild, D. Bellem, U. Schollwöck, T. Giamarchi, C. Gross, et al. "Quantum dynamics of a mobile spin impurity". In: *Nature Physics* 9 (2013), p. 235.

[21] D. M. Eigler and E. K. Schweizer. "Positioning single atoms with a scanning tunnelling microscope". In: *Nature* 344 (1990), pp. 524–526.

[22] R. Hooke. *Micrographia (1665)*. Vol. 20. AppLife, 2014.

[23] W. S. Bakr, J. I. Gillen, A. Peng, S. Fölling, and M. Greiner. "A quantum gas microscope for detecting single atoms in a Hubbard-regime optical lattice". In: *Nature* 462 (2009), p. 74.

[24] J. F. Sherson, C. Weitenberg, M. Endres, M. Cheneau, I. Bloch, and S. Kuhr. "Single-atom-resolved fluorescence imaging of an atomic Mott insulator". In: *Nature* 467 (2010), p. 68.

[25] C. Weitenberg, M. Endres, J. F. Sherson, M. Cheneau, P. Schauß, T. Fukuhara, I. Bloch, and S. Kuhr. "Single-spin addressing in an atomic Mott insulator". In: *Nature* 471 (2011), p. 319.

[26] P. Zupancic, P. M. Preiss, R. Ma, A. Lukin, M. E. Tai, M. Rispoli, R. Islam, and M. Greiner. "Ultra-precise holographic beam shaping for microscopic quantum control". In: *Optics Express* 24 (2016), pp. 13881–13893.

[27] L. D'Alessio, Y. Kafri, A. Polkovnikov, and M. Rigol. "From quantum chaos and eigenstate thermalization to statistical mechanics and thermodynamics". In: *Advances in Physics* 65 (2016), pp. 239–362.

[28] P. M. Preiss, R. Ma, M. E. Tai, A. Lukin, M. Rispoli, P. Zupancic, Y. Lahini, R. Islam, and M. Greiner. "Strongly correlated quantum walks in optical lattices". In: *Science* 347 (2015), pp. 1229–1233.

[29] D. Podolsky, A. Auerbach, and D. P. Arovas. "Visibility of the amplitude (Higgs) mode in condensed matter". In: *Physical Review B* 84 (2011), p. 174522.

[30] L. Pollet and N. Prokof'ev. "Higgs mode in a two-dimensional superfluid". In: *Physical Review Letters* 109 (2012), p. 010401.

[31] D. Podolsky and S. Sachdev. "Spectral functions of the Higgs mode near two-dimensional quantum critical points". In: *Physical Review B* 86 (2012), p. 054508.

[32] M. Endres, T. Fukuhara, D. Pekker, M. Cheneau, P. Schauβ, C. Gross, E. Demler, S. Kuhr, and I. Bloch. "The 'Higgs' amplitude mode at the two-dimensional superfluid/Mott insulator transition". In: *Nature* 487 (2012), p. 454.

[33] J. Struck, C. Ölschläger, R. Le Targat, P. Soltan-Panahi, A. Eckardt, M. Lewenstein, P. Windpassinger, and K. Sengstock. "Quantum simulation of frustrated classical magnetism in triangular optical lattices". In: *Science* 333 (2011), pp. 996–999.

[34] J. Struck, M. Weinberg, C. Ölschläger, P. Windpassinger, J. Simonet, K. Sengstock, R. Höppner, P. Hauke, A. Eckardt, M. Lewenstein, et al. "Engineering Ising-XY spin-models in a triangular lattice using tunable artificial gauge fields". In: *Nature Physics* 9 (2013), p. 738.

[35] T. Fukuhara, S. Hild, J. Zeiher, P. Schauß, I. Bloch, M. Endres, and C. Gross. "Spatially resolved detection of a spin-entanglement wave in a Bose-Hubbard chain". In: *Physical Review Letters* 115 (2015), p. 035302.

[36] T. Fukuhara, P. Schauß, M. Endres, S. Hild, M. Cheneau, I. Bloch, and C. Gross. "Microscopic observation of magnon bound states and their dynamics". In: *Nature* 502 (2013), p. 76.

[37] W. S. Bakr, A. Peng, M. E. Tai, R. Ma, J. Simon, J. I. Gillen, S. Foelling, L. Pollet, and M. Greiner. "Probing the superfluid–to–Mott insulator transition at the single-atom level". In: *Science* 329 (2010), pp. 547–550.

[38] A. Omran, M. Boll, T. A. Hilker, K. Kleinlein, G. Salomon, I. Bloch, and C. Gross. "Microscopic observation of Pauli blocking in degenerate fermionic lattice gases". In: *Physical Review Letters* 115 (2015), p. 263001.

[39] M. F. Parsons, F. Huber, A. Mazurenko, C. S. Chiu, W. Setiawan, K. Wooley-Brown, S. Blatt, and M. Greiner. "Site-resolved imaging of fermionic Li 6 in an optical lattice". In: *Physical Review Letters* 114 (2015), p. 213002.

[40] L. W. Cheuk, M. A. Nichols, M. Okan, T. Gersdorf, V. V. Ramasesh, W. S. Bakr, T. Lompe, and M. W. Zwierlein. "Quantum-gas microscope for fermionic atoms". In: *Physical Review Letters* 114 (2015), p. 193001.

[41] G. J. Edge, R. Anderson, D. Jervis, D. C. McKay, R. Day, S. Trotzky, and J. H. Thywissen. "Imaging and addressing of individual fermionic atoms in an optical lattice". In: *Physical Review A* 92 (2015), p. 063406.

[42] E. Haller, J. Hudson, A. Kelly, D. A. Cotta, B. Peaudecerf, G. D. Bruce, and S. Kuhr. "Single-atom imaging of fermions in a quantum-gas microscope". In: *Nature Physics* 11 (2015), pp. 738–742.

[43] C. J. Foot. *Atomic Physics*. Oxford University Press, 2014.

[44] D. Steck. *Rb 87 D Line Data*. Oregon Center for Optics and Department of Physics, University of Oregon. 2015.

[45] R. Grimm, M. Weidemüller, and Y. B. Ovchinnikov. "Optical dipole traps for neutral atoms". In: *Advances in Atomic, Molecular, and Optical Physics*. Vol. 42. 2000, pp. 95–170.

[46] C. J. Pethick and H. Smith. *Bose–Einstein condensation in dilute gases*. Cambridge University Press, 2008.

[47] W. Ketterle, D. S. Durfee, and D. M. Stamper-Kurn. "Making, probing and understanding Bose-Einstein condensates". In: *arXiv:cond-mat/9904034* (1999).

[48] G.-B. Liao, K.-S. Wu, C.-Y. Shih, Y.-H. Cheng, L.-A. Sun, Y.-J. Lin, and M.-S. Chang. "Optimization of a crossed optical dipole trap for loading and confining laser-cooled atoms". In: *J. Opt. Soc. Am. B* 34 (2017), pp. 869–876.

[49] J. Dalibard. "Collisional dynamics of ultra-cold atomic gases". In: *Proceedings of the International School of Physics-Enrico Fermi*. Vol. 321. 1999, p. 14.

[50] S. N. Bose. "Plancks Gesetz und Lichtquantenhypothese". In: *Zeitschrift für Physik* 26 (1924), pp. 178–181.

[51] A. Einstein. "Quantum theory of the monatomic ideal gas". In: *Sitzungsberichte der Preussischen Akademie der Wissenschaften, Physikalisch-mathematische Klasse* 22 (1924), pp. 261–267.

[52] A. Einstein. "Quantum theory of the monatomic ideal gas". In: *Sitzungsberichte der Preussischen Akademie der Wissenschaften, Physikalisch-mathematische Klasse* 1 (1925), p. 3.

[53] F. Dalfovo, S. Giorgini, L. P. Pitaevskii, and S. Stringari. "Theory of Bose-Einstein condensation in trapped gases". In: *Reviews of Modern Physics* 71 (1999), p. 463.

[54] O. Penrose and L. Onsager. "Bose-Einstein condensation and liquid helium". In: *Physical Review* 104 (1956), p. 576.

[55] Craig David Colquhoun. "A New Apparatus for Experiments with Caesium Bose-Einstein Condensates". PhD thesis. University of Strathclyde, 2019.

[56] D. J. Griffiths. *Introduction to Electrodynamics*. Prentice Hall, 1999.

[57] *Cateye External Cavity Diose Laser, Model CEL002*. Revision 1.02. Moglabs. 2014.

[58] C. J. Hawthorn, K. P. Weber, and R. E. Scholten. "Littrow configuration tunable external cavity diode laser with fixed direction output beam". In: *Review of Scientific Instruments* 72 (2001), pp. 4477–4479.

[59] G. S. Giri. *Laser Spectroscopy of Rubidium, English Version Manual For F. Praktikum*. Fakultät IV - Physik, Universität Siegen. 2016.

[60] C. P. Pearman, C. S. Adams, S. G. Cox, P. F. Griffin, D. A. Smith, and I. G. Hughes. "Polarisation spectroscopy of a closed atomic transition: applications to laser frequency locking". In: *J. Phys. B: At. Mol. Opt. Phys.* 35 (2002), pp. 5141–5151.

[61] T. Pyragius. "Developing and building an absorption imaging system for Ultracold Atoms". PhD thesis. 2012.

[62] F. Lord Rayleigh. "Investigations in Optics, with Special Reference to the Spectroscope". In: *Philosphical magazine* 5 (1879).

[63] M. Greiner. "Ultracold quantum gases in three-dimensional optical lattice potentials". PhD thesis. Ludwig-Maximilians-Universität München, 2003.

[64] T. M. Brzozowski, M. Maczynska, M. Zawada, J. Zachorowski, and W. Gawlik. "Time-of-flight measurement of the temperature of cold atoms for short trap-probe beam distances". In: *Journal of Optics B: Quantum and Semiclassical Optics* 4 (1, 2002), pp. 62–66.

[65] Andrea Di Carli. "A tunable quantum gas for matter-wave interferometry and soliton experiments". PhD thesis. University of Strathclyde, 2019.

[66] J.-Q. Huang, X.-S. Yan, C.-F. Wu, J.-W. Zhang, and L.-J. Wang. "Intense source of cold cesium atoms based on a two-dimensional magneto-optical trap with independent axial cooling and pushing". In: *Chinese Physics B* 25 (2016), p. 063701.

[67] W. Petrich, M. H. Anderson, J. R. Ensher, and E. A. Cornell. "Behavior of atoms in a compressed magneto-optical trap". In: *J. Opt. Soc. Am. B* 11 (1994), pp. 1332–1335.

[68] P. Zeeman. "The Effect of Magnetisation on the Nature of Light Emitted by a Substance". In: *Nature* 55 (1897).

[69] S. Reynaud, M. Himbert, J. Dalibard, J. Dupont-Roc, and C. Cohen-Tannoudji. "Compensation of Doppler broadening by light shifts in two photon absorption". In: *Optics Communications* 42 (1982), p. 6.

[70] U. Fano. "Effects of Configuration Interaction on Intensities and Phase Shifts". In: *Physical Review* 124 (1961), pp. 1866–1878.

[71] I. F. Bloch. "Atomlaser und Phasenkohärenz atomarer Bose-Einstein-Kondensate". PhD thesis. Ludwig-Maximilians-Universität München, 2000.

[72] M. Garwood and L. DelaBarre. "The return of the frequency sweep: designing adiabatic pulses for contemporary NMR". In: *Journal of magnetic resonance* 153 (2001), pp. 155–177.

[73] A. J. Leggett. "Bose-Einstein condensation in the alkali gases: Some fundamental concepts". In: *Reviews of Modern Physics* 73 (2001), p. 307.

[74] D. M. Farkas, E. A. Salim, and J. Ramirez-Serrano. "Production of Rubidium Bose-Einstein Condensates at a 1 Hz Rate". In: *arXiv:1403.4641 [cond-mat, physics:physics]* (2014).

[75] J. Rudolph, W. Herr, C. Grzeschik, T. Sternke, A. Grote, M. Popp, D. Becker, H. Müntinga, H. Ahlers, A. Peters, et al. "A high-flux BEC source for mobile atom interferometers". In: *New Journal of Physics* 17 (2015), p. 065001.

[76] M. Horikoshi and K. Nakagawa. "Atom chip based fast production of Bose-Einstein condensate". In: *Appl. Phys. B* 82 (2006), pp. 363–366.

[77] M. H. T. Extavour, L. J. LeBlanc, T. Schumm, B. Cieslak, S. Myrskog, A. Stummer, S. Aubin, and J. H. Thywissen. "Dual-Species Quantum Degeneracy of 40K and 87Rb on an Atom Chip". In: *AIP Conference Proceedings* 869 (2006), pp. 241–249.

[78] R. Roy, A. Green, R. Bowler, and S. Gupta. "Rapid Cooling to Quantum Degeneracy in Dynamically Shaped Atom Traps". In: *Phys. Rev. A* 93 (2016), p. 043403.

[79] T. Kinoshita, T. Wenger, and D. S. Weiss. "All-optical Bose-Einstein condensation using a compressible crossed dipole trap". In: *Physical Review A* 71 (2005), p. 011602.

[80] S. Stellmer, B. Pasquiou, R. Grimm, and F. Schreck. "Laser cooling to quantum degeneracy". In: *Phys. Rev. Lett.* 110 (2013), p. 263003.

[81] J.-F. Clément, J.-P. Brantut, M. R. D. S. Vincent, R. A. Nyman, A. Aspect, T. Bourdel, and P. Bouyer. "All-optical runaway evaporation to Bose-Einstein condensation". In: *Phys. Rev. A* 79 (2009), p. 061406.

[82] K. Yamashita, K. Hanasaki, A. Ando, M. Takahama, and T. Kinoshita. "All-optical production of a large Bose-Einstein condensate in a double compressible crossed dipole trap". In: *Physical Review A* 95 (2017), p. 013609.

[83] J. Noh, S. J. Park, C. Y. Park, W.-K. Lee, D.-H. Yu, and J. Mun. "High-performance experimental apparatus for large atom number 87Rb Bose-Einstein condensates". In: *Journal of the Korean Physical Society* 61 (2012), pp. 1021–1027.

[84] M. Cheneau, P. Barmettler, D. Poletti, M. Endres, P. Schauß, T. Fukuhara, C. Gross, I. Bloch, C. Kollath, and S. Kuhr. "Light-cone-like spreading of correlations in a quantum many-body system". In: *Nature* 481 (2012), p. 484.

[85] A. M. Kaufman, M. E. Tai, A. Lukin, M. Rispoli, R. Schittko, P. M. Preiss, and M. Greiner. "Quantum thermalization through entanglement in an isolated many-body system". In: *Science* 353 (2016), pp. 794–800.

[86] B. M. Peaudecerf, M. Andia, M. Brown, E. Haller, and S. Kuhr. "Microwave preparation of two-dimensional fermionic spin mixtures". In: *New Journal of Physics* (2019), p. 013020.

[87] C. L. Blackley, C. R. Le Sueur, J. M. Hutson, D. J. McCarron, M. P. Köppinger, H.-W. Cho, D. L. Jenkin, and S. L. Cornish. "Feshbach resonances in ultracold 85 Rb". In: *Physical Review A* 87 (2013), p. 033611.

[88] C. Kuhn, G. McDonald, K. Hardman, S. Bennetts, P. Everitt, P. Altin, J. Debs, J. Close, and N. Robins. "A Bose-condensed, simultaneous dual-species Mach–Zehnder atom interferometer". In: *New Journal of Physics* 16 (2014), p. 073035.

[89] E. Altman, W. Hofstetter, E. Demler, and M. D. Lukin. "Phase diagram of two-component bosons on an optical lattice". In: *New Journal of Physics* 5 (2003), p. 113.

[90] M. Lewenstein, A. Sanpera, and V. Ahufinger. *Ultracold Atoms in Optical Lattices: Simulating quantum many-body systems*. Oxford University Press, 2012.